

**SOME THEORETICAL AND EXPERIMENTAL STUDIES
OF
CAVITATION NOISE**

Thesis by
Sanjay Kumar
Division of Engineering and Applied Science

In Partial Fulfillment
of the Requirements for the Degree of
Doctor of Philosophy

California Institute of Technology
Pasadena, California 91125
1992
(Submitted August 2, 1991)

ACKNOWLEDGEMENTS

I wish to express my deep gratitude to my advisor, Professor Christopher Brennen. His personal and professional guidance, patience and a very caring human touch have been invaluable during my stay at Caltech and have made completion of this work possible. I am also grateful to Professor Allan Acosta for very helpful advice and insights I could not have done without. I am thankful to Professor Rolf Sabersky and Professor James Knowles for their inspiration and excellent classes.

I used experimental equipment prepared by Dr. Steven Ceccio for the experimental part of this investigation. I thank Steve for the facilities and advice which made speedy completion of the experimental part of this thesis possible. Marty Gould rendered exceptional help in repairing the water tunnel windows at short notices. I thank Marty for his help and Cecilia Lin for preparation of the figures. I would also like to thank Jackie Beard and Dana Young for their support and help. I thank Joe Fontana and Rich Eastvedt of W.M. Keck Laboratory of Hydraulics and Water Resources for their help during the experiments.

I thank my colleagues Anthony Wexler, Douglas Hart, Yan Kuhn de Chizelle, Adiel Guinzberg, Talal Balaa and Abhijit Bhattacharyya for their invaluable friendship and help.

Funding for this work was provided by the Office of Naval Research under contract number N 000167 - 85 - K - 0165 and grant number N 00014 - 91 - J - 1295. This support is gratefully acknowledged. I would also like to thank the California Institute of Technology for the C.L. Powell Fellowship and teaching assistantship which facilitated my stay.

I thank my wife, Sangita, for her invaluable patience and support. I dedicate this thesis to my parents, Shri Pawan Shrivastava and Shrimati Usha Shrivastava whose vision and sacrifices have been invaluable in my life.

ABSTRACT

This work investigates two aspects of cavitation noise. The first part models some nonlinear interactive effects in bubbly mixtures generated in cavitating flows, and the second part focuses on an acoustical study of the collapse process of a single bubble in travelling bubble cavitation.

The nonlinear interactive effects in a bubbly cloud have been studied by investigating the frequency response of a bubble layer bounded by a wall oscillating normal to itself. First, a Fourier analysis of the Rayleigh–Plesset equation is used to obtain an approximate solution for the nonlinear response of a single bubble in an infinite fluid. This is used in an approximate solution of the oscillating wall problem for bubble layers of finite and infinite thickness in which all the bubbles have the same equilibrium size and a semi-infinite layer containing bubbles with a distribution of size. Particular attention is paid to the generation of harmonics that is due to nonlinear effects.

The finite thickness of the layer results in characteristic natural frequencies of the bubble mixture, all of which are less than bubble natural frequency. These characteristic natural frequencies are functions of the void fraction and the ratio of layer thickness to the bubble radius. In general, the lowest characteristic natural frequency is found to dominate the response. The amplitude of the response increases as the excitation frequency, ω_f , is reduced from ω_b to around $0.5\omega_b$ and decreases with further decrease in excitation frequency. The characteristic frequencies disappear in the limit of a semi-infinite layer. The bubble size oscillation in a semi-infinite layer is maximum at the excitation frequency of ω_b . The pressure oscillation is minimum at the excitation frequency of ω_b with equally significant first and second harmonic components.

For *sub-resonant* and *trans-resonant* excitation ($\omega_f < \omega_b$), the response consists of standing wave patterns with an amplitude that decays slowly with

distance from the oscillating wall. This decay is different from that found in spherical bubble clouds (d'Agostino and Brennen 1988a) because of the geometric effects of propagating disturbance. However, for *super-resonant* excitation the amplitude of oscillation rapidly decays with distance from the source of excitation.

A phenomenon termed *harmonic cascading* is seen to take place when the bubble layer consists of bubbles with a distribution of bubble sizes. In this phenomenon a large response is observed at twice the excitation frequency when the layer contains bubbles with a natural frequency equal to twice the excitation frequency. The effect is manifest as an increase in the ratio of the second harmonic to the first harmonic as the number of bubbles with small radii gets larger relative to the number of bubbles with large radii. Also, a similar change in the bubble size distribution, while holding the equilibrium void fraction constant, results in a weaker response. This reduction in amplitude of pressure oscillation may be due to the increased number of bubbles. Larger void fraction and smaller amplitudes of wall oscillation are observed to produce a weaker response. Reduced effects of viscosity and surface tension that are due to changes in ambient conditions result in a larger response.

In the second part the collapse processes of single bubbles in the travelling bubble cavitation around two axisymmetric headforms have been studied acoustically to understand the collapse process of a cavitation bubble and to characterize the sound emission in travelling bubble cavitation. The bubbles were observed to collapse and then sometimes to rebound and collapse again, resulting in one or two pulses in the acoustic signal from a cavitation event. It was observed that each of the pulses could contain more than one peak. This phenomenon is called *multipeaking* and is clearly distinct from rebounding. The occurrence of rebounding and multipeaking and their effects on some characteristic measures of the acoustic signal such as power spectra are examined in this chapter. Two particular headforms (I.T.T.C. headform and Schiebe headform) with distinct flow characteristics

were investigated.

Both rebounding and multipeaking increased with reduction in cavitation number in case of the I.T.T.C. headform. However, multipeaking decreased and rebounding increased with the reduction in cavitation number for the Schiebe headform. Smaller flow velocity, smaller cavitation number and multipeaking delay the rebound. The peak amplitude of the sound emitted from the first collapse was seen to be twice as large as the peak amplitude of sound from the second collapse suggesting a repeatable process of bubble fission during the collapse process. The multipeaking and rebounding increased the characteristic measures of the acoustic signal. These characteristic measures have larger magnitudes for smaller flow velocity. Also, the values of these characteristics are larger for the I.T.T.C. headform than for the Schiebe headform.

Theoretical calculations based on the Rayleigh–Plesset equation were seen to predict correctly the order of magnitude for most of these characteristic measures. However, the distribution of spectral energy is not properly predicted by the model based on the Rayleigh–Plesset equation; bubble fission during the collapse is thought to account for this discrepancy. Reduction in the cavitation number and multipeaking are observed to decrease the fraction of spectral energy contained in the high frequency range (30 *kHz*–80*kHz*).

TABLE OF CONTENTS

Title Page	i
Acknowledgements	ii
Abstract	iii
Table of Contents	vi
Nomenclature	viii
List of Figures	xi
List of Tables	xxi
1. Introduction	1
2. Nonlinear Effects in Bubble Clouds	4
2.1. Introduction	4
2.2. Some Typical Applications and Values	7
2.3. Nonlinear Solution for a Single Bubble	8
2.4. A Semi-infinite Bubble Layer	13
2.5. A Bubble Layer of Finite Thickness	21
2.6. A Semi-infinite Layer with Bubble Size Distribution	29
2.7. Summary	37
2.8. Limitations	39
2.9. Practical Applications	40
3. An Acoustical Study of Travelling Bubble Cavitation	80
3.1. Introduction	80
3.2. Experimental Details	82
3.3. Experimental Results	85
3.3.1. Occurrence of Multipeaking and Rebounding	85
3.3.2. Some Characteristic Measures of the Acoustic Signal	88
3.3.3. Comparison Between Experimental Results and Theoretical Calculations	91
3.3.4. Power Spectra Measurement	94
3.4. Summary	98

4. Conclusions	136
References	141

NOMENCLATURE

A_i	power spectral density at a frequency indicated by i
d	time interval between maximum peak of the main pulse and maximum peak of the rebound pulse (see Fig. 3.4)
d^*	nondimensional time interval between maximum peak of the main pulse and maximum peak of the rebound pulse (see Fig. 3.4)
i	imaginary number
I^*	nondimensional acoustic impulse, $4\pi I_m / \rho U R_h$
I_m	acoustic impulse (see Fig. 3.4)
I_s	a measure of strength of the pulse
k	polytropic constant for gas expansion and contraction
j, m, n	integer indices
l	thickness of the bubble layer
l_r	reference length scale
N	number of data points in an acoustic record
p	pressure in liquid flow field
P	peak amplitude of an acoustic pulse (see Fig. 3.4)
P_{go}	pressure of permanent gas in the bubble at undisturbed condition
P_n	complex amplitude of pressure oscillation at frequency $n\delta$
P_o	reference pressure in the liquid
P_s	total spectral power
P_s^*	a quantity proportional to total spectral power, $P_s N / R'$
P_v	vapor pressure inside the bubble
P_∞	pressure at infinity
r	ratio of maximum amplitude of the main pulse to maximum amplitude of the rebound pulse
R	radius of the bubble
R'	sampling rate used for data collection [MHz]
R_h	radius of the headform

R_m	radius of the smallest bubbles in the layer
R_M	radius of the largest bubbles in the layer
R_o	radius of the bubble in reference condition
R_n	complex amplitude of radius oscillation at frequency $n\delta$
S	surface tension of the liquid
t	time
t_1	time of beginning of an acoustic pulse (see Fig. 3.4)
t_2	time of end of an acoustic pulse (see Fig. 3.4)
T	Lagrangian time
u	velocity in the liquid flow field
U	flow velocity
x	Eulerian space coordinate normal to the wall
X	Lagrangian space coordinate normal to the wall
X_n	complex amplitude of fluid displacement oscillation at frequency $n\delta$
α	volume fraction of bubbly mixture
α_i	fractional power spectral density
α_o	volume fraction of bubbly mixture at undisturbed reference condition
δ	increment in the frequency
ϵ	normalized standard error in power spectral density
γ	ratio of specific heats
ν	kinematic viscosity
ω_b	natural frequency of the bubble (in radians/sec)
ω_f	forcing frequency for pressure or wall oscillation (in radians/sec)
ω_r	reference frequency (in radians/sec)
η	number of data sets used to calculate average power spectral density
$\eta(R_o)$	bubble number density per unit liquid volume

$\eta^*(R_o)$	bubble number density per unit total volume
η'	number of bubbles per unit liquid volume
\Re	real part of complex quantity
ρ	density of the liquid
ρ_v	density of the vapor in the bubble
σ	cavitation number
τ	volume of the bubble
τ_n	complex amplitude of the bubble volume oscillation at frequency $n\delta$
τ_o	volume of the bubble at undisturbed condition
τ_s	peak separation (see Fig. 3.4)
τ_w	duration of an acoustic pulse (see Fig. 3.4)
τ_w^*	nondimensional pulse width, $\tau_w U / R_h$

LIST OF FIGURES

Figure 2.1: Radius $R(\tau)/R_o$ is plotted against the nondimensional time, $\tau = \omega_b t$ for a single bubble. The parameters : $P_n/\omega_b^2 R_o^2 = 0.04$, $\omega_b/\omega_p = 3.0$ and $\nu/\omega_b R_o^2$ and $S/\rho\omega_b^2 R_o^3$ are for the water tunnel conditions. (—) is the numerical solution and (- - -) is the approximate analytical solution

Figure 2.2: Radius $R(\tau)/R_o$ is plotted against the nondimensional time, $\tau = \omega_b t$ for a single bubble. The parameters : $P_n/\omega_b^2 R_o^2 = 0.08$, $\omega_b/\omega_p = 3.0$ and $\nu/\omega_b R_o^2$ and $S/\rho\omega_b^2 R_o^3$ are for the water tunnel conditions. (—) is the numerical solution and (- - -) is the approximate analytical solution

Figure 2.3: Comparison of the spectra of $[1 - R(\tau)/R_o]$ obtained for a single bubble from numerical integration of the Rayleigh–Plesset equation (—) and the present approximate (- - -) analysis. The parameters : $P_n/\omega_b^2 R_o^2 = 0.08$, $\omega_b/\omega_p = 6.0$ and $\nu/\omega_b R_o^2$ and $S/\rho\omega_b^2 R_o^3$ are for the water tunnel conditions.

Figure 2.4: The frequency response of a single bubble; $|R_n|/R_o$ is plotted against the frequency ratio, $n\delta/\omega_b$, for the first five harmonics. The parameters: $P_n/\omega_b^2 R_o^2 = 0.02$ and $\nu/\omega_b R_o^2$ and $S/\rho\omega_b^2 R_o^3$ are for the water tunnel conditions.

Figure 2.5: Schematic of the Oscillating Wall Problem.

Figure 2.6: The frequency response of the bubbly cloud; $|R_n|/R_o(X=0)$ and $|P_n|/\omega_b^2 R_o^2(X=0)$ are plotted against the frequency ratio, $n\delta/\omega_b$, for the first five harmonics. The parameters: $X_n(0)/R_o = 0.03$, $\alpha_o = 0.02$ and $\nu/\omega_b R_o^2$ and $S/\rho\omega_b^2 R_o^3$ are for the water tunnel conditions.

Figure 2.7: The frequency response of the bubbly cloud; (a) $|R_n|/R_o$ and (b) $|P_n|/\omega_b^2 R_o^2$ for the fundamental harmonic are plotted against the frequency ratio, ω_x/ω_b , and the distance from the oscillating wall, X/R_o , to illustrate the decay away from the wall. The parameters: $X_n(0)/R_o = 0.03$, $\alpha_o = 0.02$ and $\nu/\omega_b R_o^2$ and $S/\rho\omega_b^2 R_o^3$ for the water tunnel conditions.

Figure 2.8: The frequency response of the bubbly cloud; (a) $|R_n|/R_o$ and (b) $|P_n|/\omega_b^2 R_o^2$ for the second harmonic are plotted against the frequency ratio, $2\omega_x/\omega_b$, and the distance from the oscillating wall, X/R_o , to illustrate the decay away from the wall. The parameters: $X_n(0)/R_o = 0.03$, $\alpha_o = 0.02$ and $\nu/\omega_b R_o^2$ and $S/\rho\omega_b^2 R_o^3$ are for the water tunnel conditions.

Figure 2.9: The effect of variation in $\nu/\omega_b R_o^2$ and $S/\rho\omega_b^2 R_o^3$ on the fundamental harmonic; $|R_n|/R_o(X = 0)$ and $|P_n|/\omega_b^2 R_o^2(X = 0)$ for the fundamental harmonic are plotted against the frequency ratio, ω_x/ω_b . The parameters: $X_n(0)/R_o = 0.03$, $\alpha_o = 0.02$ and $\nu/\omega_b R_o^2$ and $S/\rho\omega_b^2 R_o^3$ are for the water tunnel and the ocean conditions.

Figure 2.10: The effect of variation in $\nu/\omega_b R_o^2$ and $S/\rho\omega_b^2 R_o^3$ on the second harmonic; $|R_n|/R_o(X = 0)$ and $|P_n|/\omega_b^2 R_o^2(X = 0)$ for the second harmonic are plotted against the frequency ratio, $2\omega_x/\omega_b$. The parameters: $X_n(0)/R_o = 0.03$, $\alpha_o = 0.02$ and $\nu/\omega_b R_o^2$ and $S/\rho\omega_b^2 R_o^3$ are for the water tunnel and the ocean conditions.

Figure 2.11: The effect of change in the void fraction, α_o , on the fundamental harmonic; $|R_n|/R_o(X = 0)$ and $|P_n|/\omega_b^2 R_o^2(X = 0)$ for the fundamental harmonic are plotted against the frequency ratio, ω_x/ω_b . The parameters: $X_n(0)/R_o = 0.03$ and $\nu/\omega_b R_o^2$ and $S/\rho\omega_b^2 R_o^3$ are for the water tunnel conditions. Values of the void fraction, α_o , of 0.005, 0.020 and 0.100 are used.

Figure 2.12: The effect of change in the void fraction, α_o , on the second harmonic; $|R_n|/R_o(X = 0)$ and $|P_n|/\omega_b^2 R_o^2(X = 0)$ for the second harmonic are plotted against the frequency ratio, $2\omega_x/\omega_b$. The parameters: $X_n(0)/R_o = 0.03$ and $\nu/\omega_b R_o^2$ and $S/\rho\omega_b^2 R_o^3$ are for the water tunnel conditions. Values of the void fraction, α_o , of 0.005, 0.020 and 0.100 are used.

Figure 2.13: The effect of change in the amplitude of wall oscillation, $X_n(0)/R_o$, on the fundamental harmonic; $|R_n|/R_o(X = 0)$ and $|P_n|/\omega_b^2 R_o^2(X = 0)$ for the

fundamental harmonic are plotted against the frequency ratio, ω_x/ω_b . The parameters: $\alpha_o = 0.02$ and $\nu/\omega_b R_o^2$ and $S/\rho\omega_b^2 R_o^3$ are for the water tunnel conditions. $X_n(0)/R_o$ values of 0.01, 0.03 and 0.06 are used.

Figure 2.14: The effect of change in the amplitude of wall oscillation, $X_n(0)/R_o$, on the second harmonic; $|R_n|/R_o(X = 0)$ and $|P_n|/\omega_b^2 R_o^2(X = 0)$ for the second harmonic are plotted against the frequency ratio, $2\omega_x/\omega_b$. The parameters: $\alpha_o = 0.02$ and $\nu/\omega_b R_o^2$ and $S/\rho\omega_b^2 R_o^3$ are for the water tunnel conditions. $X_n(0)/R_o$ values of 0.01, 0.03 and 0.06 are used.

Figure 2.15: Schematic of the Oscillating Wall Problem With a Layer of Finite Thickness.

Figure 2.16: The frequency response of a bubbly layer of finite thickness; $|R_n|/R_o(X = 0)$ and $|P_n|/\omega_b^2 R_o^2(X = 0)$ are plotted against the frequency ratio, $n\delta/\omega_b$, for the first two harmonics. The parameters: $X_n(0)/R_o = 0.02$, $\alpha_o = 0.02$, $l/R_o = 20$ and $\nu/\omega_b R_o^2$ and $S/\rho\omega_b^2 R_o^3$ are for the water tunnel conditions.

Figure 2.17: The frequency response of a bubbly layer of finite thickness; (a) $|R_n|/R_o$ and (b) $|P_n|/\omega_b^2 R_o^2$ for the fundamental harmonic are plotted against the frequency ratio, ω_x/ω_b , and the distance from the oscillating wall, X/l , for the first harmonic. The parameters: $X_n(0)/R_o = 0.02$, $\alpha_o = 0.02$, $l/R_o = 20$ and $\nu/\omega_b R_o^2$ and $S/\rho\omega_b^2 R_o^3$ are for the water tunnel conditions.

Figure 2.18: The frequency response of a bubbly layer of finite thickness; (a) $|R_n|/R_o$ and (b) $|P_n|/\omega_b^2 R_o^2$ for the second harmonic are plotted against the frequency ratio, $2\omega_x/\omega_b$, and the distance from the oscillating wall, X/l , for the second harmonic. The parameters: $X_n(0)/R_o = 0.02$, $\alpha_o = 0.02$, $l/R_o = 20$ and $\nu/\omega_b R_o^2$ and $S/\rho\omega_b^2 R_o^3$ are for the water tunnel conditions.

Figure 2.19: The effect of variation in $\nu/\omega_b R_o^2$ and $S/\rho\omega_b^2 R_o^3$ on the fundamental harmonic; $|R_n|/R_o(X = 0)$ and $|P_n|/\omega_b^2 R_o^2(X = 0)$ for the fundamental harmonic are plotted against the frequency ratio, ω_x/ω_b . The parameters:

$X_n(0)/R_o = 0.005$, $\alpha_o = 0.02$, $l/R_o = 20$ and $\nu/\omega_b R_o^2$ and $S/\rho\omega_b^2 R_o^3$ are for the water tunnel and the ocean conditions.

Figure 2.20: The effect of variation in $\nu/\omega_b R_o^2$ and $S/\rho\omega_b^2 R_o^3$ on the second harmonic; $|R_n|/R_o(X = 0)$ and $|P_n|/\omega_b^2 R_o^2(X = 0)$ for the second harmonic are plotted against the frequency ratio, $2\omega_x/\omega_b$. The parameters: $X_n(0)/R_o = 0.005$, $\alpha_o = 0.02$, $l/R_o = 20$ and $\nu/\omega_b R_o^2$ and $S/\rho\omega_b^2 R_o^3$ are for the water tunnel and the ocean conditions.

Figure 2.21: The effect of change in the thickness of the bubble layer, l/R_o , on the fundamental harmonic; $|R_n|/R_o(X = 0)$ and $|P_n|/\omega_b^2 R_o^2(X = 0)$ for the fundamental harmonic are plotted against the frequency ratio, ω_x/ω_b . The parameters: $X_n(0)/R_o = 0.02$, $\alpha_o = 0.02$ and $\nu/\omega_b R_o^2$ and $S/\rho\omega_b^2 R_o^3$ are for the water tunnel conditions. Values of the thickness of the bubble layer, l/R_o , of 10, 20 and 50 are used.

Figure 2.22: The effect of change in thickness of the bubble layer, l/R_o , on the second harmonic; $|R_n|/R_o(X = 0)$ and $|P_n|/\omega_b^2 R_o^2(X = 0)$ for the second harmonic are plotted against the frequency ratio, $2\omega_x/\omega_b$. The parameters: $X_n(0)/R_o = 0.02$, $\alpha_o = 0.02$ and $\nu/\omega_b R_o^2$ and $S/\rho\omega_b^2 R_o^3$ are for the water tunnel conditions. Values of the thickness of the bubble layer, l/R_o , of 10, 20 and 50 are used.

Figure 2.23: The effect of change in the void fraction, α_o , on the fundamental harmonic; $|R_n|/R_o(X = 0)$ and $|P_n|/\omega_b^2 R_o^2(X = 0)$ for the fundamental harmonic are plotted against the frequency ratio, ω_x/ω_b . The parameters: $X_n(0)/R_o = 0.02$, $l/R_o = 20$ and $\nu/\omega_b R_o^2$ and $S/\rho\omega_b^2 R_o^3$ are for the water tunnel conditions. Values of the void fraction, α_o , of 0.005, 0.020 and 0.100 are used.

Figure 2.24: The effect of change in the void fraction, α_o , on the second harmonic; $|R_n|/R_o(X = 0)$ and $|P_n|/\omega_b^2 R_o^2(X = 0)$ for the second harmonic are plotted against the frequency ratio, $2\omega_x/\omega_b$. The parameters: $X_n(0)/R_o = 0.02$, $l/R_o = 20$ and $\nu/\omega_b R_o^2$ and $S/\rho\omega_b^2 R_o^3$ are for the water tunnel conditions. Values of

the void fraction, α_o , of 0.005, 0.020 and 0.100 are used.

Figure 2.25: The effect of change in the amplitude of wall oscillation, $X_n(0)/R_o$, on the fundamental harmonic; $|R_n|/R_o(X = 0)$ and $|P_n|/\omega_b^2 R_o^2(X = 0)$ for the fundamental harmonic are plotted against the frequency ratio, ω_x/ω_b . The parameters: $\alpha_o = 0.02$, $l/R_o = 20$ and $\nu/\omega_b R_o^2$ and $S/\rho\omega_b^2 R_o^3$ are for the water tunnel conditions. Values of the amplitude of wall oscillation, $X_n(0)/R_o$, of 0.005, 0.010 and 0.020 are used.

Figure 2.26: The effect of change in the amplitude of wall oscillation, $X_n(0)/R_o$, on the second harmonic; $|R_n|/R_o(X = 0)$ and $|P_n|/\omega_b^2 R_o^2(X = 0)$ for the second harmonic are plotted against the frequency ratio, $2\omega_x/\omega_b$. The parameters: $\alpha_o = 0.02$, $l/R_o = 20$ and $\nu/\omega_b R_o^2$ and $S/\rho\omega_b^2 R_o^3$ are for the water tunnel conditions. Values of the amplitude of wall oscillation, $X_n(0)/R_o$, of 0.005, 0.010 and 0.020 are used.

Figure 2.27: The frequency response of a bubbly layer with a given size distribution of bubbles; $|P_n|/\omega_r^2 l_r^2(X = 0)$ is plotted against the frequency ratio, $n\delta/\omega_r$, for the first two harmonics and the linear solution for (a) $m = 2$, (b) $m = 3$ and (c) $m = 4$. The parameters: $X_n(0)/l_r = 0.0002$, $\alpha_o = 0.05$ and the ambient conditions are for the water tunnel.

Figure 2.28: The frequency response of a bubbly layer with a given size distribution of bubbles; $|P_n|/\omega_r^2 l_r^2$ for the (a) first and (b) second harmonic is plotted against the distance from the wall, X/l_r , and the frequency ratio, (a) ω_x/ω_r and (b) $2\omega_x/\omega_r$, respectively. The parameters: $X_n(0)/l_r = 0.0002$, $\alpha_o = 0.05$, $m = 3$ and the ambient conditions are for the water tunnel.

Figure 2.29: The effect of variation in the bubble size density distribution slope, m , on the (a) first and (b) second harmonic; $|P_n|/\omega_r^2 l_r^2(X = 0)$ is plotted against the frequency ratio, (a) ω_x/ω_r and (b) $2\omega_x/\omega_r$, respectively. The parameters: $X_n(0)/l_r = 0.0002$, $\alpha_o = 0.05$ and the ambient conditions are for the water tunnel.

Figure 2.30: The effect of variation in ambient conditions on the fundamental harmonic; $|P_n|/\omega_r^2 l_r^2 (X=0)$ for the fundamental harmonic is plotted against the frequency ratio, ω_x/ω_r , for (a) $m=2$, (b) $m=3$ and (c) $m=4$. The parameters: $X_n(0)/l_r=0.0002$, $\alpha_o=0.05$ and the ambient conditions are for the water tunnel and the ocean.

Figure 2.31: The effect of variation in ambient conditions on the second harmonic; $|P_n|/\omega_r^2 l_r^2 (X=0)$ for the second harmonic is plotted against the frequency ratio, $2\omega_x/\omega_r$, for (a) $m=2$, (b) $m=3$ and (c) $m=4$. The parameters: $X_n(0)/l_r=0.0002$, $\alpha_o=0.05$ and the ambient conditions are for the water tunnel and the ocean.

Figure 2.32: The effect of changes in void fraction, α_o , on the fundamental harmonic; $|P_n|/\omega_r^2 l_r^2 (X=0)$ for the fundamental harmonic is plotted against the frequency ratio, ω_x/ω_r , for (a) $m=2$, (b) $m=3$ and (c) $m=4$. The parameters: $X_n(0)/l_r=0.0002$ and the ambient conditions are for the water tunnel. Values of the void fraction, α_o , of 0.01, 0.05 and 0.10 are used.

Figure 2.33: The effect of changes in void fraction, α_o , on the second harmonic; $|P_n|/\omega_r^2 l_r^2 (X=0)$ for the second harmonic is plotted against the frequency ratio, $2\omega_x/\omega_r$, for (a) $m=2$, (b) $m=3$ and (c) $m=4$. The parameters: $X_n(0)/l_r=0.0002$ and the ambient conditions are for the water tunnel. Values of the void fraction, α_o , of 0.01, 0.05 and 0.10 are used.

Figure 2.34: The effect of changes in the amplitude of wall oscillation, $X_n(0)/l_r$, on the fundamental harmonic; $|P_n|/\omega_r^2 l_r^2 (X=0)$ for the fundamental harmonic is plotted against the frequency ratio, ω_x/ω_r , for (a) $m=2$, (b) $m=3$ and (c) $m=4$. The parameters: $X_n(0)/l_r=0.0002$ and the ambient conditions are for the water tunnel. Values of the amplitude of wall oscillation, $X_n(0)/l_r$, of 0.00008, 0.0002 and 0.0005 are used.

Figure 2.35: The effect of changes in amplitude of wall oscillation, $X_n(0)/l_r$,

on the second harmonic; $|P_n|/\omega_r^2 l_r^2 (X=0)$ for the second harmonic is plotted against the frequency ratio, $2\omega_x/\omega_r$, for (a) $m=2$, (b) $m=3$ and (c) $m=4$. The parameters: $X_n(0)/l_r=0.0002$ and the ambient conditions are for the water tunnel. Values of the amplitude of wall oscillation, $X_n(0)/l_r$, of 0.00008, 0.0002 and 0.0005 are used.

Figure 2.36: The power spectra of noise that is due to cavitation produced by rotating rods in the Thames river (from Mellen (1954)). The peaks at 1.25, 2.5 and 5 *kHz* (marked respectively as (1), (2) and (3)) may be due to *harmonic cascading*.

Figure 2.37: The spectra of noise that is due to cavitation on the suction side of a propeller blade (from Blake (1986)). The peaks at 8.5, 17 and 34 *kHz* (marked respectively as (1), (2) and (3)) may be due to *harmonic cascading*.

Figure 3.1: Schematics illustrating (a) instrumentation of the headform and (b) Low Turbulence Water Tunnel.

Figure 3.2: Pressure distributions on the (a) I.T.T.C. and (b) Schiebe headforms.

Figure 3.3: A typical amplified and filtered signal for a single cavitation event illustrating multiple peaks and a rebound. Inset shows the complete acoustic trace.

Figure 3.4: Sketch of a typical acoustic trace with the definitions of some measured quantities.

Figure 3.5: Probabilities of different types of cavitation events on the (a) I.T.T.C. headform and (b) Schiebe headform indicating the occurrence of multiple peaks or a rebound. R and NR respectively denote events with and without rebound. The number alongside indicates the number of peaks in the main pulse.

Figure 3.6: Probabilities of different number of peaks in the rebound pulse for cavitation events on the (a) I.T.T.C. headform and (b) Schiebe headform. The legend indicates number of peaks in the rebound pulse.

Figure 3.7: Probabilities of different types of cavitation events with rebound for

the (a) I.T.T.C. headform and (b) Schiebe headform. A two-letter symbol is used to classify the event with the first letter indicating the number of peaks in the main pulse and the second letter, the number of peaks in the rebound pulse; s indicates single peak and m indicates more than one peak.

Figure 3.8: A typical photograph from Ceccio and Brennen (1991) illustrating the bubble breaking up into two or more pieces during the collapse.

Figure 3.9: Ratio of the peak pressure amplitude of the main pulse to peak pressure amplitude of the rebound pulse, r , as a function of the cavitation number. The legend indicates the headform, the type of event and the flow velocity.

Figure 3.10: Variation of the time between the main pulse and the rebound pulse as a function of the cavitation number. The legend indicates the headform, the type of event and the flow velocity.

Figure 3.11: The figure illustrates the dependence of the acoustic impulse, I_m , on the type of event for the I.T.T.C. headform. The flow velocity is 8 m/sec.

Figure 3.12: The peak separation, τ_s , as a function of the flow velocity for each headform. The legend indicates the type of headform and the flow velocity.

Figure 3.13: The figure illustrates the dependence of I_s on the flow velocity for sp -type event on the I.T.T.C. headform.

Figure 3.14: The figure illustrates the dependence of the acoustic impulse, I_m , on the flow velocity for mp -type events on the Schiebe headform.

Figure 3.15: The figure illustrates the variation of the acoustic impulse, I_m , with the type of headform for sp -type of events. The flow velocity is 8 m/sec.

Figure 3.16: Experimentally obtained values of the nondimensional pulse width, τ_w^* , plotted against the nondimensional impulse, I^* , and compared with the values from the numerical integration of the Rayleigh–Plesset equation. The data for the I.T.T.C. headform and different cavitation numbers. The flow velocity is 8 m/sec.

Figure 3.17: Experimentally obtained values of the nondimensional time between the main pulse and the rebound pulse, d^* , plotted against the nondimensional impulse, I^* , and compared with the values from the numerical integration of the Rayleigh–Plesset equation. The data for the I.T.T.C. headform and different cavitation numbers. The flow velocity is 8 m/sec .

Figure 3.18: Experimentally obtained values of the nondimensional time between the main pulse and the rebound pulse, d^* , plotted against the nondimensional impulse, I^* . The data for the I.T.T.C. headform, different flow velocities and cavitation number of 0.50.

Figure 3.19: Experimentally obtained values of the nondimensional pulse width, τ_w^* , plotted against the nondimensional impulse, I^* . The data for the I.T.T.C. headform, different flow velocities and cavitation number of 0.45.

Figure 3.20: The total spectral power, P_s , plotted against the cavitation number for different types of events and the flow velocities. Data for the I.T.T.C. headform.

Figure 3.21: The total spectral power, P_s , plotted against the cavitation number for different types of events and the flow velocities. Data for the Schiebe headform.

Figure 3.22: Typical nondimensional power spectral density obtained from the experimental data for the Schiebe headform at $\sigma = 0.45$ and flow velocity of 9 m/sec . The superimposed spectrum is from the numerical calculations using the Rayleigh–Plesset equation for a 100 μm nucleus at the water tunnel conditions.

Figure 3.23: Effect of reduction in the cavitation number on the nondimensional power spectral density. Experimental data for sp -type events on the I.T.T.C. headform and flow velocity of 8 m/sec .

Figure 3.24: Effect of reduction in the cavitation number on the nondimensional power spectral density. Experimental data for mp -type events on the Schiebe headform and flow velocity of 8 m/sec .

Figure 3.25: Effect of multipeaking on the nondimensional power spectral density. Experimental data for the Schiebe headform at $\sigma = 0.50$ and flow velocity of 8 *m/sec*.

Figure 3.26: Effect of flow velocity on the nondimensional power spectral density. Experimental data for *mp*-type events on the I.T.T.C. headform at $\sigma = 0.45$.

Figure 3.27: Effect of flow velocity on the nondimensional power spectral density. Experimental data for *mp*-type events on the Schiebe headform at $\sigma = 0.55$.

Figure 3.28: Comparison of the nondimensional power spectral density for the I.T.T.C. and the Schiebe headforms. Experimental data for *mp*-type events, flow velocity of 8 *m/sec* and cavitation number of 0.55.

Figure 3.29: Comparison of the nondimensional power spectral density for the I.T.T.C. and the Schiebe headforms. Experimental data for *sp*-type events, flow velocity of 8 *m/sec* and cavitation number of 0.45.

Figure 3.30: Comparison of the nondimensional power spectral density for the I.T.T.C. and the Schiebe headforms. Experimental data for *mp*-type events, flow velocity of 9 *m/sec* and cavitation number of 0.55.

LIST OF TABLES

Table 2.1: Fluid and Bubble Parameters for the Examples Presented

Table 3.1: Percentage Errors in Power Spectral Density

Table 3.2: Changes in the Nondimensional Power Spectral Density – Cavitation Number Reduction.

Table 3.3: Changes in the Nondimensional Power Spectral Density – Effect of Multipeaking

Table 3.4: Changes in the Nondimensional Power Spectral Density – Effect of Flow Velocity

Table 3.5: Changes in the Nondimensional Power Spectral Density – Difference Between Two Headforms

Chapter 1

INTRODUCTION

A free stream nucleus grows into a large cavity when it migrates into low pressure regions in a flow and stays there long enough to permit nonlinear growth. This cavity collapses violently upon migration into flow regions with larger pressure resulting in sound emission and damage to the solid surfaces nearby. This phenomenon is termed bubble cavitation and is a major source of noise and damage in ship propellers, hydrofoils and turbomachines and affects their performance by altering the flow. The bubble cavitation is also important in design and operation of sonars, cavitation detecting devices and in acoustic techniques of flow measurement.

Much of the theoretical studies of bubble cavitation are based on Plesset's modification (Plesset (1949)) of the Rayleigh equation for a collapsing cavity (Rayleigh (1917)). Since then, the theory has been modified to include factors such as compressibility effects (Gilmore (1952)) and presence of a solid wall (Plesset and Chapman(1971)). Fitzpatrick and Strasberg (1956) proposed using the Rayleigh-Plesset equation along with the pressure history in the flow to calculate spectra of the emitted noise. Mellen (1954) reported presence of f^{-2} dependence in high frequency spectrum of the cavitation noise, and Brooke Benjamin (1958) related it to the presence of shock waves caused by liquid compressibility during the collapse process.

Knapp and Hollander (1948) laid out much of the experimental foundation for study of the bubble cavitation. Since then, hydrodynamically produced bubble cavitation has been studied by many researchers including Parkin (1952), Blake *et al.* (1977) and Hamilton (1981). The collapse of spark and laser produced cavities has also been acoustically and photographically studied to understand the physical mechanisms in the collapse of cavities next to a solid wall (Lauterborn and Bolle (1975), Kimoto (1987) and Vogel *et al.* (1989)). van der Meulen and

van Renesse (1989) studied the collapse of laser generated cavities in flows near hemispherical headforms. These studies have reported the generation of a jet and a counter jet during the collapse of a bubble and have increased our understanding of the bubble collapse process. Blake *et al.* (1986) have theoretically modeled the collapse of these cavities.

Much of the theoretical investigation does not take into account the effect of various fluid dynamical factors such as vortices, flow separation and turbulence. Baiter (1986) has suggested a model that includes real flow effects for noise emission from the single bubble collapse by way of experimental measurement, for characterizing the process of bubble cavitation and associated noise emission. Experimental measurements by Ceccio and Brennen (1991) suggest some measurements towards characterization of the bubble cavitation noise.

For flows with large concentration of bubbles, the experimental results of Arakeri and Shanmuganathan (1985) and Marboe *et al.* (1986) suggest that the cavitation noise cannot be explained on the basis of single bubble theories alone. Probably the interactive effects among bubbles influence the global patterns in the flow. Tangren, Dodge and Seifert (1949) and van Wijngaarden made first attempts to model these interactions in bubbly mixtures. This effort has been carried out in two different ways. van Wijngaarden(1964), Morch (1982), d'Agostino *et al.* (1988a and 1988b) have modeled the bubbly mixtures as continuum, and Chahine(1982) has modeled the bubbly mixtures by summing up the effects of individual bubbles in presence of other bubbles. Recently, d'Agostino and Brennen (1988a) and Omta (1987) have reported linearized dynamics of spherical bubble clouds. Most of these efforts are based on linearized continuum equations along with the linearized Rayleigh–Plesset equation to include the bubble dynamics. These models are also restricted to bubbly mixtures of single size bubbles.

The present work investigates two different problems in cavitation noise. The theoretical part of this investigation is aimed at modeling nonlinear effects in

bubbly clouds and physical features such as the finite dimension of the cloud and the bubble size distribution in the cloud have been included. The experimental component of the investigation involves an acoustical study of bubble collapse process by characterizing main features of the acoustic signal generated by a collapsing bubble and relating these features and the flow variables to other measures of the acoustic signal such as spectra and peak amplitudes. It is hoped that such an investigation suggests some ways of characterizing the single bubble sound emission through experimental measurement.

The results from single bubble measurements may be combined with interactive effects in bubbly mixtures to enable a qualitative understanding of sound emission in bubble clouds.

Chapter 2

NONLINEAR EFFECTS IN BUBBLE CLOUDS

2.1 Introduction

The purpose of this research is to gain some understanding of the global effects of bubble dynamics in the fluid mechanics of bubbly flows. At the most basic level, this interaction occurs because the pressure changes generate rapid volume changes which cause accelerating velocity fields that affect the pressure distribution in the flow.

Traditionally, such flows have been studied using the single bubble dynamics and assuming no interaction among the bubbles in the flow field. Such an approach ignores interactive effects that the bubble dynamics has on the global pressure distribution in the flow field and is accurate only in case of extremely dilute bubble concentrations. Experimental results of Arakeri and Shanmuganathan (1985) have indicated that experimental measurements of cavitation noise cannot be the result of many single bubble signals. Marboe *et al.* (1986) have measured noise spectrum at lower frequencies in travelling bubble cavitation than can be explained on the basis of single bubble theories. Both papers indicate interactive effects for bubble flows with a large concentration of bubbles. Later researchers have used continuum mechanics models with bubble dynamics models to analyze global interactive effects. Indeed, d'Agostino and Brennen (1988a) and Omta (1987) found that the characteristic natural frequencies of a spherical cloud of bubbles can be much lower than the natural frequency of a single bubble. However, these recent analyses use linearized models of the bubble dynamics and the flow. It is well known that the dynamics of a bubble can be quite nonlinear (Prosperetti (1974)), which in combination with nonlinear convective effects may produce significant nonlinear effects in bubbly flows. The objective of the present research is to understand these nonlinear effects by studying some analytically amenable model problems.

The nonlinear dynamics in the growth and collapse of a single bubble has been studied for a long time (e.g., Plesset and Prosperetti (1977)). Early studies of bubbly flows, based on using space averaged equations, did not include bubble dynamic effects. These treated the bubbly mixture as an equivalent, compressible, homogeneous medium (Tangren, Dodge and Seifert (1949)). Among the first to focus on the dynamics of bubble clusters was van Wijngaarden (1964), who analyzed the collapse of a large number of bubbles next to a flat wall and found considerable increase in the pressure at the wall as a result of the interactive effects. Biesheuvel and van Wijngaarden (1984) have developed more general, equivalent flow models of dispersed two phase mixtures, including the phenomena of bubble dynamics, relative motion and liquid compressibility, by ensemble and volume averaging of conservation equations for each separate phase. Most of the later research efforts are based on these equations.

Morch (1980 and 1982) considered the collapse of a spherical bubble cloud characterized by a cloud radius and uniform volume fraction. He assumed that the pressure increase would lead to shock formation at the cloud boundary and that the shock would propagate inward and completely annihilate bubbles in its path. This model did not include individual bubble dynamics and predicted infinite pressure and infinite collapse velocities as the radius approached zero. In a subsequent paper Hansson *et al.* (1982) constructed a model using a continuum mechanics approach and used the Rayleigh–Plesset equation to model the bubble dynamics. In particular, the response of a bubble cloud to a vibrating horn and the cavitating flow in an accelerating water column were considered. Chahine (1982) developed a method using matched asymptotic expansions. This model assumes instantaneous transmission of ambient conditions to the bubbles and thus neglects the compressibility of the bubble cloud. This is a major weakness in the model because compressibility of the cloud will not be negligible for moderate to large void fractions. It was found that because of interactive effects in the cloud,

the larger the number of bubbles in the cloud, the more delayed and violent is the implosion and thus larger are the pressures generated. This method is also limited to low void fraction flows and to a small number of bubbles in a specified configuration. Chahine(1983) also developed a model using a continuum mechanics approach and first order gradient theory.

Omta (1987) has carried out analytical solutions for small amplitude oscillations and numerical solutions for large amplitudes. Omta linearized the Biesheuvel–van Wijngaarden equations for homogeneous flows (Biesheuvel and van Wijngaarden (1984)) and obtained the solution under a number of simplifying assumptions. Frequency spectra for the bubble cloud were obtained. The bubble cloud was found to possess characteristic natural frequencies with the lowest one dominating the cloud behavior. The natural frequencies of the cloud were found to depend upon void fraction and not upon the bubble size, a feature that seems particularly true at the lowest cloud natural frequency. d’Agostino and Brennen (1988a) also solved for the linearized dynamics of spherical bubble clouds using a continuum mechanics model with bubble dynamics under more general conditions. This model includes various dissipative mechanisms including the relative motion between phases. The main conclusions from this analysis were found to be virtually the same as as the ones obtained by Omta (1987). d’Agostino *et al.* (1988b) also solved for the linearized dynamics of the flow of bubbly mixture over slender surfaces. Recently Birnir and Smereka (1990) have carried out numerical solutions for bubble clouds and investigated the solutions using techniques used to study the dynamical systems. They found that the bubble radius, flow velocity and pressure were bounded and the cloud was seen to possess natural frequencies. Periodic solution was seen to be stable for weak excitation. Other than these very little has been done on the nonlinear solutions of the dynamics of bubble clouds. The objective of the present work is to develop a methodology for handling nonlinear terms and to obtain nonlinear solutions by studying the dynamics of a bubbly

liquid next to a flat wall that oscillates normal to its own plane. The cases of a layer of identical bubbles of finite and infinite thickness have been examined. Also, a semi-infinite layer with a given bubble size distribution has been examined and reveals an entirely new phenomenon of *harmonic cascading* in such clouds. The purpose is to obtain a qualitative understanding of the various mechanisms of frequency dispersion in the bubbly two-phase mixtures associated with cavitation.

2.2 Some Typical Applications and Values

Bubbly mixtures occur in a variety of industrial applications. Cavitation clouds generated by cavitation on propellers are an important source of noise and damage to the propellers. Single bubbles in the travelling bubble cavitation have been observed to break up into many smaller bubbles (Blake *et al.* (1977) and Ceccio and Brennen (1991)); and the sound generated during the collapse process may be described by the theory for bubble clouds. The typical values for evaluating the results of the present analysis have been selected with these physical situations in mind.

A number of researchers have measured the size of free stream nuclei (Gates and Acosta (1978) and O'Hern *et al.*(1987)) and cavitation bubbles (Maeda *et al.* (1991)). The bubbles have been found to vary in size between 10 μm and 150 μm . The bubble size distribution is described by

$$\eta(R_o) = \frac{N^*}{R_o^m} \quad (1)$$

where $\eta(R_o) dR_o$ is the number of bubbles per unit liquid volume with equilibrium radii between R_o and $R_o + dR_o$. The distribution of the form given by Equation (1) has been used to describe the size distribution of free stream nuclei in sea water and various water tunnel facilities with $N \approx 0.00001$ and $m \approx 3 \rightarrow 4$ (Brennen and Ceccio(1989)). The bubble size distribution in cavitation clouds (Maeda *et al.* (1991)) can also be adequately described by Equation (1) with suitable values of

N^* and m . The void fraction values due to free stream nuclei are extremely small. Though the void fraction for a cavitation cloud is larger than the one that is due to free stream nuclei, it is still small at approximately 0.03% (Maeda *et al.* (1991)). No measurement of the void fraction of the cloud resulting from the breakup of a collapsing bubble is known. The void fraction values used for evaluating the nonlinear effects have been chosen according to experimental results of Arakeri and Shanmuganathan (1985) for weak interaction effects in the bubbly mixtures.

Table 2.1 lists the values used. The fluid has been chosen to be water at room temperature (20 ° C). A bubble subject to periodic excitation oscillates with the value of the polytropic constant, k , between 1 and γ (Plesset and Hsieh (1960)). For illustrative purposes the value of the polytropic constant, k , has been chosen to be 1. The bubble radius has been selected to be a typical size for nuclei and cavitation bubbles. For evaluating the nonlinear interactive effects in clouds with a size distribution of bubbles, the bubble size distribution is assumed to be given by Equation (1) with bubble radii between 10 μm and 100 μm . The values in the data set I are typical of the conditions in a water tunnel where the static pressure has been lowered to induce cavitation. Similarly, the values in the data set II represent conditions in cavitating flows near the ocean surface at atmospheric conditions. Henceforth the values in data set I will be referred to as *Water Tunnel* values and the values in data set II will be referred to as *Ocean* values.

2.3 Nonlinear Solution for a Single Bubble

There exists a substantial body of literature on the nonlinear dynamics of a single bubble in an infinite fluid; this has been reviewed by Plesset and Prosperetti (1977). In the present context it is appropriate to note that Eller and Flynn (1969) solved the problem of subharmonics of order one-half, using a perturbation procedure and that Prosperetti (1974) generated nonlinear analytical solutions for subharmonics and harmonics of various orders, using a perturbation method.

In the present work it is necessary to construct the very simplest nonlinear

solution of the Rayleigh–Plesset equation for a single bubble. Later this will be used as a building block for the problem of many bubbles interacting in a flow. The bubble is assumed to be spherical and to contain water vapor and residual permanent gas. The bubble interior is assumed to be uniform with constant vapor pressure, P_v . The permanent gas in the bubble is assumed to behave polytropically with an index, k , between 1 and γ (Plesset and Hsieh (1960)). The liquid compressibility is included only in the radiation damping, and this is done by including it in the effective viscosity used for the bubble dynamics (Devin (1959) and Prosperetti (1977)). The bubble growth that is due to rectified diffusion has been ignored since that takes place at a much slower time scale than the natural cycle of the bubble (Hsieh and Plesset (1961)). With these assumptions the Rayleigh–Plesset equation describing the bubble dynamics becomes

$$R \frac{D^2 R}{Dt^2} + \frac{3}{2} \left(\frac{DR}{Dt} \right)^2 + \frac{4\nu}{R} \frac{DR}{Dt} + \frac{2S}{\rho R} = \frac{P_v - P_\infty(t)}{\rho} + \frac{P_{go}}{\rho} \left(\frac{R_o}{R} \right)^{3k} \quad (2)$$

In the present solution a Fourier series expansion is used and terms up to second order are retained in order to examine these corrections to the linear solution. The bubble radius $R(t)$ and the pressure at infinity $P_\infty(t)$ are expanded in the form

$$R = R_o + \sum_{n=1}^N \Re(R_n e^{in\delta t}) \quad (3)$$

and

$$\frac{P_\infty(t)}{\rho} = P_o + \sum_{n=1}^N \Re(P_n e^{in\delta t}) \quad (4)$$

where P_n and R_n are complex quantities and the frequencies $n\delta$, $n = 1, N$ represent a discretization of the frequency domain. These expansions are substituted into Equation (2), and all terms of third or higher order in R_n/R_o are neglected in order to extract the simplest nonlinear effects. Finally, coefficients of $e^{in\delta t}$ on both sides of the simplified equation are equated to yield the following relation for P_n and R_n :

$$\frac{P_n}{\omega_b^2 R_o^2} = \Lambda(n) \frac{R_n}{R_o} + \sum_{j=1}^{n-1} \beta_1(n, j) \frac{R_j}{R_o} \frac{R_{n-j}}{R_o} + \sum_{j=1}^{N-n} \beta_2(n, j) \frac{\bar{R}_j}{R_o} \frac{R_{n+j}}{R_o} \quad (5)$$

where the overbar denotes a complex conjugate, and the bubble natural frequency,

ω_b is given by

$$\omega_b = \left(\frac{3kP_{go}}{\rho R_o^2} - \frac{2S}{\rho R_o^3} \right)^{\frac{1}{2}} \quad (6)$$

and $\Lambda(n)$, $\beta_1(n, j)$ and $\beta_2(n, j)$ are defined as

$$\Lambda(n) = \left[\frac{n^2 \delta^2}{\omega_b^2} - 1 - i \frac{n\delta}{\omega_b} \frac{4\nu}{\omega_b R_o^2} \right] \quad (7)$$

$$\beta_1(n, j) = \frac{3k+1}{4} + \frac{3k-1}{2} \frac{S}{\rho \omega_b^2 R_o^3} + \frac{1}{2} \frac{\delta^2}{\omega_b^2} (n-j) \left(n + \frac{j}{2} \right) + i \frac{2\nu}{\omega_b R_o^2} \frac{\delta}{\omega_b} (n-j) \quad (8)$$

and

$$\beta_2(n, j) = \frac{3k+1}{2} + (3k-1) \frac{S}{\rho \omega_b^2 R_o^3} + \frac{1}{2} \frac{\delta^2}{\omega_b^2} (n^2 - nj - j^2) + i \frac{2\nu}{\omega_b R_o^2} \frac{n\delta}{\omega_b} \quad (9)$$

Using a Newton–Raphson Scheme, Equation (5) is solved iteratively for R_n/R_o , given P_n , the fluid properties and individual bubble characteristics. It was seen numerically that if there is a single excitation frequency, ω_f , then the only nonzero components of the bubble oscillation, R_n , will occur at the harmonics of excitation frequency. It is also seen that the response R_n/R_o decays with increase in the order of the harmonic and is negligible (amplitude $\ll 10^{-20}$) at harmonics of order higher than 50. Thus calculating the response up to 50 harmonics was considered sufficient. It is also clear from Equations (8) and (9) that $\beta_1(n, j)$ and $\beta_2(n, j)$ are functions of $n\delta/\omega_b$ and j/n . Furthermore, note from Equation (5) that for a single excitation frequency, the only coefficients $\beta_1(n, j)$ and $\beta_2(n, j)$ that enter the calculations are those for which j and n take values corresponding to harmonics of the excitation frequency. Consequently the only values of $n\delta/\omega_b$ and j/n that enter the calculations are those that are ratios between an excitation frequency harmonic and the natural frequency of the bubble or two excitation frequency harmonics. Hence, despite the explicit appearance of δ , the results of the calculation are independent of this parameter used in discretizing the frequency domain. Finally, note also that the pressure perturbations, P_n , occur in (5) only in linear form and thus can be large without introducing error into the solution. However, the analysis is valid only for $|R_n/R_o| \ll 1$. This defines the extent of

the weak nonlinear effects that are examined here and indirectly, implies an upper limit on the magnitude of $P_n/\omega_b^2 R_o^2$.

For illustrative purposes, we select the values of the parameters $\nu/\omega_b R_o^2$ and $S/\rho\omega_b^2 R_o^3$ for the water tunnel conditions listed in Table 2.1. The bubble radius value is typical for cavitation bubbles. For illustrative purposes, the polytropic constant, k , has been chosen to be 1. We chose to consider a single bubble subjected to an oscillating pressure at infinity containing a single frequency, ω_f , with an amplitude $|P_n|/\omega_b^2 R_o^2$. First of all, results obtained from Equation (5) are compared to a numerical integration of the Rayleigh–Plesset equation, which uses a fourth order Runge–Kutta scheme. In Figs. 2.1 and 2.2 the radius–time behavior obtained from our analysis and the numerical integration of the Rayleigh–Plesset equation are compared. The ratio ω_b/ω_f is 3 and values of $P_n/\omega_b^2 R_o^2$ for Figs. 2.1 and 2.2 are 0.04 and 0.08, respectively. It can be seen that the present approximate analysis works very well for weak nonlinear effects or small values of $P_n/\omega_b^2 R_o^2$. The agreement between the numerical integration and the present approximate solution is less satisfactory for larger values of $P_n/\omega_b^2 R_o^2$, as shown in Fig. 2.2.

It was seen numerically that Equation (5) has a nontrivial solution only at the harmonics of excitation frequency. It can be seen that such a solution is one of the solutions of Equation (5). However, at present it is impossible to prove the uniqueness of the solution for nonlinear equations such as Equation (5). The comparison of the approximate solution to the numerical solution as done in Figs. 2.1 and 2.2 is one way to confirm the correctness of the present solution.

A comparison of the spectra of $[1 - R(t)/R_o]$ is made in Fig. 2.3 for the case in which the $P_n/\omega_b^2 R_o^2$ and ω_b/ω_f values are 0.08 and 6, respectively. It can be seen that the present approximate solution agrees well with the numerical integration for frequencies at which the magnitude is significant. Note that the radius oscillations occur at harmonics of the frequency of the pressure oscillation, ω_f . The excitation frequency, ω_f , is varied from $\omega_b/100$ to $2\omega_b$ for the purpose

of calculating the frequency response of the layer. Fig. 2.4 shows the frequency response of a single bubble subjected to a pressure oscillation with a $P_n/\omega_b^2 R_o^2$ value of 0.02. The lines labelled [1] are the magnitudes of the response at the fundamental excitation frequency, ω_f so that in this case, the abscissa represents ω_f/ω_b . The lines labelled [2] represent the magnitudes of the response at twice the excitation frequency, and in this case the abscissa represents $2\omega_f/\omega_b$. A general line labelled [m] represents the magnitude of the response at m times the excitation frequency, and in this case the abscissa represents the frequency, $m\omega_f/\omega_b$. Thus, all the harmonics are plotted against the actual reduced frequency, ω/ω_b , at which they occur and in this figure we have presented the results for harmonics up to fifth order. In viewing these results it should be recognised that those harmonics with magnitudes below a certain level are of dubious significance since higher order nonlinearities could markedly alter those results. It can be seen that ω_b is the dominant frequency in the radius oscillation as would be expected from the linear analysis.

Eller and Flynn (1969) observed that for pressure oscillations with an amplitude larger than a threshold value, the bubble radius oscillation will contain a subharmonic of order one half. This can also be seen in Lauterborn's numerical calculation of the frequency response of a single bubble (Lauterborn (1976)) and in the third order perturbation solution of Prosperetti(1974). The threshold value of pressure oscillation needed to generate subharmonics in the response is a minimum for the excitation frequency of $2\omega_b$ (Eller and Flynn(1969)). The presence of a subharmonic component also marks the beginning of large amplitude radius oscillations. The presence of subharmonics in the response has been used as the beginning of sound emission in cavitation by Vaughan(1968) and Neppiras(1968). On the other hand, the present solution does not give rise to subharmonics in the domain of its validity; i.e., $R_n/R_o \ll 1$. The present model addresses the steady state frequency response of bubbly flows in weakly nonlinear situations, and the

numerical solution of the Rayleigh–Plesset equation (Equation (2)) for weakly nonlinear situations does not yield subharmonic components in the response. This is because the subharmonics are generated by nonlinearities at an order higher than quadratic. Also, the absence of subharmonics from our approximate solution does not imply limitation of the validity of the present solution for weakly nonlinear situations defined by $R_n/R_o \ll 1$.

More accurate nonlinear solutions than the one described above (for example Prosperetti (1974)) exist and have been reported in the literature. The value of the present solution lies in its simplicity and the feasibility of incorporating it in an analysis of the collective response of a cloud of bubbles.

2.4. A Semi-infinite Bubble Layer

The specific problem addressed in this paper is shown schematically in Fig. 2.5. Liquid containing bubbles is bounded by a flat wall that oscillates in a direction normal to itself at a given frequency, ω_f . The resulting flow is assumed to be a function of x and t only. The continuum mechanics equations are used with a number of simplifying assumptions in order to obtain a soluble set of equations. The volume of liquid involved in condensation and evaporation during bubble oscillation has been ignored. This is a reasonable assumption in view of the large difference of densities between the liquid and the vapor phases. The liquid has been assumed to be incompressible, and the relative motion between the phases has been ignored. The compressibility of the liquid and the relative motion provide for the energy dissipation in the flow. These were found by d’Agostino and Brennen (1988a) to have very little effect on important features such as the natural frequencies of the flow. The most important contribution of these damping mechanisms is in making the response nonsingular at resonant frequencies. This can be incorporated in the present solution by taking an appropriate value of effective viscosity in place of the liquid viscosity used in the Rayleigh–Plesset equation. Hence, neglecting the medium compressibility and the relative motion are reasonable assumptions. The breakup and coalescence of bubbles are assumed not to occur for flows under weakly nonlinear excitation. The number of bubbles per unit liquid volume, η' , will remain constant under these assumptions, and η' is

also assumed to be uniform. Under these simplifying assumptions, the continuity and the momentum equations can be written in the form:

$$\frac{\partial u}{\partial x} = \frac{\eta'}{(1 + \eta'\tau)} \frac{D\tau}{Dt} \quad (10)$$

$$\rho \frac{Du}{Dt} = -(1 + \eta'\tau) \frac{\partial p}{\partial x} \quad (11)$$

The solution to the problem represented by Equations (10), (11) and (2) is obtained in Lagrangian coordinates, X and T for which the above equations become

$$(1 + \eta'\tau) \frac{\partial u}{\partial X} = \eta' \frac{\partial \tau}{\partial T} \frac{\partial x}{\partial X} \quad (12)$$

and

$$\frac{\partial u}{\partial T} \frac{\partial x}{\partial X} = -(1 + \eta'\tau) \frac{1}{\rho} \frac{\partial p}{\partial X} \quad (13)$$

Consistent with the structure of the solution sought, the relationship between the Lagrangian and the Eulerian coordinates, X and x , is written in the form

$$x = X + \sum_{n=1}^N \Re (X_n(X) e^{in\delta T}) \quad (14)$$

and the bubble volume, τ , and pressure, P , are expressed by the expansions

$$\tau = \tau_o + \sum_{n=1}^N \Re (\tau_n(X) e^{in\delta T}) \quad (15)$$

and

$$\frac{P}{\rho} = P_o + \sum_{n=1}^N \Re (P_n(X) e^{in\delta T}) \quad (16)$$

The expansions (14), (15) and (16) are substituted into Equation (12) and coefficients of $e^{in\delta T}$ are equated to obtain

$$\begin{aligned} \frac{dX_n}{dX} = & \alpha_o \frac{\tau_n}{\tau_o} + \alpha_o \sum_{j=1}^{n-1} \frac{(2j-n) \tau_j}{2n} \frac{dX_{n-j}}{\tau_o} \frac{dX}{dX} \\ & + \alpha_o \sum_{j=1}^{N-n} \frac{(n+2j)}{2n} \left[\frac{\tau_{n+j}}{\tau_o} \frac{d\overline{X}_j}{dX} - \frac{\overline{\tau}_j}{\tau_o} \frac{dX_{n+j}}{dX} \right] \end{aligned} \quad (17)$$

Similar substitution into the momentum equation (Equation (13)) leads to

$$\begin{aligned}
\frac{dP_n}{dX} &= (1 - \alpha_o) n^2 \delta^2 X_n \\
&+ \frac{1}{2} \sum_{j=1}^{n-1} \left[(1 - \alpha_o) (n - j)^2 \delta^2 X_{n-j} \frac{dX_j}{dX} - \alpha_o \frac{\tau_j}{\tau_o} \frac{dP_{n-j}}{dX} \right] \\
&+ \frac{1}{2} \sum_{j=1}^{N-n} \left[\begin{aligned} &(n + j)^2 \delta^2 (1 - \alpha_o) X_{j+n} \frac{d\bar{X}_j}{dX} \\ &+ j^2 \delta^2 (1 - \alpha_o) \bar{X}_j \frac{dX_{j+n}}{dX} \\ &- \alpha_o \frac{\bar{\tau}_j}{\tau_o} \frac{dP_{n+j}}{dX} - \alpha_o \frac{\tau_{j+n}}{\tau_o} \frac{d\bar{P}_j}{dX} \end{aligned} \right] \tag{18}
\end{aligned}$$

Note that in the linear approximation Equations (17) and (18) become

$$\frac{dX_n}{dX} = \alpha_o \frac{\tau_n}{\tau_o} \tag{19}$$

and

$$\frac{dP_n}{dX} = (1 - \alpha_o) n^2 \delta^2 X_n \tag{20}$$

It is consistent with the level of approximation to substitute these first order expressions into the quadratic terms in Equations (17) and (18), which then become

$$\frac{dX_n}{dX} = \alpha_o \frac{\tau_n}{\tau_o} + \alpha_o^2 \sum_{j=1}^{n-1} \frac{(2j - n) \tau_j}{2n} \frac{\tau_{n-j}}{\tau_o} + O(\alpha_o^3) \tag{21}$$

and

$$\frac{dP_n}{dX} = (1 - \alpha_o) n^2 \delta^2 X_n + O(\alpha_o^3) \tag{22}$$

The simple algebraic relation between the bubble radius, R , and the bubble volume, τ , namely, $\tau = 4\pi R^3/3$, leads to

$$\frac{\tau_n}{\tau_o} = 3 \frac{R_n}{R} + \frac{3}{2} \sum_{j=1}^{n-1} \frac{R_j}{R_o} \frac{R_{n-j}}{R_o} + 3 \sum_{j=1}^{N-n} \frac{\bar{R}_j}{R_o} \frac{R_{n+j}}{R_o} \tag{23}$$

and using this in (21) and (22), one obtains the following equation

$$\frac{d^2 (P_n / \omega_b^2 R_o^2)}{d(x/R_o)^2} = 3\alpha_o (1 - \alpha_o) \left(\frac{n\delta}{\omega_b} \right)^2 \frac{R_n}{R_o} + f_{n1}(X) \tag{24}$$

where $f_{n1}(X)$ is given by

$$f_{n1}(X) = 3\alpha_o(1 - \alpha_o) \left(\frac{n\delta}{\omega_b}\right)^2 \left[\sum_{j=1}^{n-1} \left(\frac{1}{2} + \frac{3\alpha_o(2j-n)}{2n}\right) \frac{R_j}{R_o} \frac{R_{n-j}}{R_o} + \sum_{j=1}^{N-n} \frac{\overline{R}_j}{R_o} \frac{R_{n+j}}{R_o} \right] \quad (25)$$

At this point in the solution we have obtained one relation, Equation (24), connecting the pressure coefficients, P_n to the radius coefficients, R_n . We now introduce the Rayleigh–Plesset equation, which will provide a second such relation. More specifically, we use Equation (5) which may be written as

$$\frac{P_n}{\omega_b^2 R_o^2} = \Lambda(n) \frac{R_n}{R_o} + f_{n2}(X) \quad (26)$$

where

$$f_{n2}(X) = \sum_{j=1}^{n-1} \beta_1(n, j) \frac{R_j}{R_o} \frac{R_{n-j}}{R_o} + \sum_{j=1}^{N-n} \beta_2(n, j) \frac{\overline{R}_j}{R_o} \frac{R_{n+j}}{R_o} \quad (27)$$

where $\beta_1(n, j)$ and $\beta_2(n, j)$ are given by Equations (8) and (9). For convenience we define λ_n such that

$$\lambda_n^2 = 3\alpha_o(1 - \alpha_o) \left(\frac{n\delta}{\omega_b}\right)^2 / \Lambda(n) \quad (28)$$

Now the linear terms involving the radius coefficients, R_n/R_o , can be eliminated from the simultaneous Equations (24) and (26) to yield the following differential equation for the pressure coefficients, P_n :

$$\frac{d^2 (P_n/\omega_b^2 R_o^2)}{d(X/R_o)^2} = \lambda_n^2 \left[\frac{P_n}{\omega_b^2 R_o^2} - f_{n2}(X) \right] + f_{n1}(X) \quad (29)$$

The solution of this equation has the form

$$\frac{P_n}{\omega_b^2 R_o^2} = \Lambda(n) a_n e^{-\lambda_n X/R_o} + f_{n3}(X) \quad (30)$$

where from Equations (26) and (30) we have

$$\frac{R_n}{R_o} = a_n e^{-\lambda_n X/R_o} + [f_{n3}(X) - f_{n2}(X)] / \Lambda(n) \quad (31)$$

and using Equations (29) and (30)

$$\frac{d^2 f_{n3}}{d(x/R_o)^2} = \lambda_n^2 [f_{n3}(X) - f_{n2}(X)] + f_{n1}(X) \quad (32)$$

Having obtained the form of solution (31) and noting that the linear component of this solution can be written as

$$\frac{R_n}{R_o} = a_n e^{-\lambda_n X/R_o} \quad (33)$$

we can proceed to evaluate $f_{n1}(X)$ and $f_{n2}(X)$ from Equations (25) and (27) by noting that it is consistent with the level of approximation to use the expression (33) in quadratic terms. Then Equation (32) can be solved exactly, the solution taking the form :

$$f_{n3}(X) = \left[\begin{array}{l} \sum_{j=1}^{n-1} \beta_3(n, j) a_j a_{n-j} e^{-(\lambda_j + \lambda_{n-j})X/R_o} \\ + \sum_{j=1}^{N-n} \beta_4(n, j) \bar{a}_j a_{n+j} e^{-(\bar{\lambda}_j + \lambda_{n+j})X/R_o} \end{array} \right] \quad (34)$$

where

$$\beta_3(n, j) = \frac{\lambda_n^2}{(\lambda_j + \lambda_{n-j})^2 - \lambda_n^2} \left[\Lambda(n) \left(\frac{1}{2} + 3\alpha_o \frac{(2j-n)}{2n} \right) - \beta_1(n, j) \right] \quad (35)$$

and

$$\beta_4(n, j) = \frac{\lambda_n^2}{(\bar{\lambda}_j + \lambda_{n+j})^2 - \lambda_n^2} [\Lambda(n) - \beta_2(n, j)] \quad (36)$$

Using Equations (20), (30) and (34) we get following equation

$$\begin{aligned} -\frac{\lambda_n}{3\alpha_o} \frac{X_n(0)}{R_o} &= a_n + \sum_{j=1}^{n-1} \beta_5(n, j) a_j a_{n-j} \\ &+ \sum_{j=1}^{N-n} \beta_6(n, j) \bar{a}_j a_{n+j} \end{aligned} \quad (37)$$

where

$$\beta_5(n, j) = \frac{\lambda_n (\lambda_j + \lambda_{n-j})}{(\lambda_j + \lambda_{n-j})^2 - \lambda_n^2} \left[\frac{1}{2} + 3\alpha_o \frac{(2j-n)}{2n} - \beta_1(n, j) / \Lambda(n) \right] \quad (38)$$

and

$$\beta_8(n, j) = \frac{\lambda_n (\bar{\lambda}_j + \lambda_{n+j})}{(\bar{\lambda}_j + \lambda_{n+j})^2 - \lambda_n^2} [1 - \beta_2(n, j)/\Lambda(n)] \quad (39)$$

This completes the solution because for given fluid and bubble properties, the values of λ_n are known through the definition (28). For a given nondimensional wall oscillation amplitude, $X_n(0)/R_o$ and given bubble properties Equation (37) can be solved for a_n using a Newton–Raphson scheme. Then $P_n/\omega_b^2 R_o^2$ at the wall can be calculated using Equations (30) and (34). Equations (33) and (27) are used to estimate $f_{n2}(X)$, which is then used with Equations (34) and (31) to calculate the radius response, R_n/R_o .

Equation (37) is similar in structure to Equation (5). Thus for wall motion at a single frequency, ω_f , the only nonzero response occurs at the harmonics of ω_f . For the same reasons as given earlier in the context of Equation (5), the solutions to the Equation (37) are independent of the interval of discretization, δ . Also, both $P_n/\omega_b^2 R_o^2$ and R_n/R_o appear only at harmonics of the frequency of the wall oscillation, ω_f . Thus the software may be written so as to evaluate only the response of nonzero amplitude, in other words at the harmonics of the excitation frequency. Calculation of the harmonics up to order 10 was found to be sufficient, harmonics of higher order being negligible. For the purpose of demonstrating the nonlinear effects, we chose to vary the wall oscillation frequency from $\omega_b/100$ to $2\omega_b$, and the resulting magnitudes of the harmonics $P_n/\omega_b^2 R_o^2$ and R_n/R_o at the wall are plotted as functions of the reduced frequency $n\delta/\omega_b$. Data for the two sets of values listed in Table 2.1 will be presented. A convenient reference case will consist of water tunnel conditions, listed in Table 2.1, plus a void fraction, α_o , of 0.02 and an amplitude of wall oscillation, $X_n(0)/R_o$, of 0.03. The ocean conditions listed in Table 2.1 will be used to examine the effect of varying the viscous and surface tension parameters. The effect on the results of varying α_o and $X_n(0)/R_o$ will also be examined.

Results for the reference case are presented in Fig. 2.6 in exactly the same

way as the earlier results were presented in Fig. 2.4. We reiterate that data below a certain magnitude will be substantially affected by higher order nonlinearities. The first point to note is that the response rapidly decays at higher harmonics. For the purpose of discussion of the results, a frequency at which the response is a maximum will be called an enhanced frequency and a frequency at which the response is a minimum will be called a suppressed frequency. From Fig. 2.6, it can be seen that the dominant enhanced frequency for the bubble radius oscillations is ω_b for harmonics of all orders. Also, the second harmonic has enhanced frequencies of ω_b and $2\omega_b$ where the response at $2\omega_b$ is significant. It can also be seen that the higher harmonics have other enhanced and suppressed frequencies.

In contrast to the radius oscillations, fundamental harmonic in pressure oscillation has a suppressed frequency close to ω_b . The pressure oscillation increases linearly with excitation frequency for excitation frequencies greater than ω_b . The linear increase in pressure for frequencies larger than ω_b indicates that the bubbles do not respond as quickly as the excitation requires and that the whole bubble mass moves as a homogeneous medium in response to the oscillating wall, with lesser influence of bubble oscillation for frequencies larger than ω_b . The suppression in the fundamental harmonic at ω_b is also predicted by the linear solution. It can be seen that the dominant second harmonic response occurs at $2\omega_b$ which is of a little larger amplitude than the response of the fundamental harmonic at ω_b . Furthermore, harmonics of all orders have a suppressed frequency of approximately $3\omega_b$, though the reasons for this are not clear. Significant amplitude of the second harmonic is one of the main results from the nonlinear analysis. Also, the minimum amplitude of pressure oscillation at ω_b probably indicates the effect of global motion in the flow.

Apart from considering the frequency response at the wall, it is also of interest to know its variation away from the wall. This is indicated in Figs. 2.7 and 2.8. The amplitude of the first harmonic is plotted as a surface, indicating

its variation as a function of the frequency ratio, ω/ω_b and the distance from the wall, X/R_o . The first harmonic of the pressure oscillation decays rapidly with distance from the wall for frequencies larger than ω_b . On the other hand, decay is less rapid for lower frequencies. The fundamental harmonic of radius oscillation decays rapidly till the distance of $2R_o$ from the wall for frequencies close to ω_b . The decay is less rapid farther away from the wall. The second harmonic of pressure and radius oscillation also decays rapidly up to a distance of $2R_o$ from the wall; the decay at larger distances is slower in comparison. The pressure oscillation at $2\omega_b$ decays completely about $20R_o$ away from the wall.

The effect of changing the viscous and the surface tension parameters while all other parameters remain unchanged is illustrated in Figs. 2.9 and 2.10 for the first and second harmonic, respectively. This contains a comparison between the results for the ocean conditions and the earlier results for the the water tunnel conditions. Larger viscous and surface tension parameters tend to inhibit bubble oscillations. Hence the response curves for the ocean conditions exhibit sharper peaks and troughs. Otherwise, the basic form of the response is very similar for the two sets of data. An additional feature of the results presented in Fig. 2.10 deserves special attention. First, note that the strong nonlinearity present at the enhanced frequency for ocean conditions has resulted in splitting into two adjacent, enhanced frequencies. This is exemplified in Fig. 2.10 by the response in the radius oscillations at $2\omega_b$.

Next, the effect of varying the void fraction is demonstrated in Figs. 2.11 and 2.12, where data for void fraction values of 0.005, 0.020 and 0.100 are compared. Note that the main features of the results, namely, the enhanced and suppressed frequencies, remain almost the same. However, the nonlinear response is enhanced as the void fraction is reduced. This dependence can be predicted from the linear solution in which both radius and pressure are given by terms multiplied by the factor $[(1 - \alpha_o)/3\alpha_o]^{1/2}$. For the small void fractions considered here,

the denominator dominates this factor and implies larger effects at smaller void fractions. This is observed at both the fundamental and second harmonics. Also, with the increased level of nonlinearity, stronger second harmonic response is seen at ω_b and approximately $0.6\omega_b$, which is absent at the larger void fractions.

Finally, the effect of changing the amplitude of the wall motion $X_n(0)/R_o$ while keeping void fraction constant at 0.02 is shown in Figs. 2.13 and 2.14. Values of 0.01, 0.03 and 0.06 for $X_n(0)/R_o$ are used. The nonlinear effects become stronger for larger values of $X_n(0)/R_o$. The effect is similar to the effects seen from decreasing void fraction.

2.5. A Bubble Layer of Finite Thickness

The geometry of the flow for which a solution was obtained in Section 2.4 was not typical of any real flow in the sense that it was not characterized by any typical dimension of the bubble cloud. It is known that the presence of such length scale as a finite thickness of the bubble layer results in characteristic natural frequencies of the bubble cloud (d'Agostino and Brennen (1988a) and Omta (1987)). The natural frequencies for undamped oscillation of a spherical bubble cloud were given by d'Agostino and Brennen (1988a) as

$$\frac{\omega_n}{\omega_b} = \left[1 + \frac{3\alpha_o(1-\alpha_o)}{(n-1/2)^2\pi^2} \left(\frac{A_o}{R_o} \right)^2 \right]^{-\frac{1}{2}} ; n = 1, 2, \dots \quad (40)$$

where A_o is the equilibrium radius of the cloud. It can be easily seen that all the natural frequencies given by the Equation (40) are less than ω_b and are packed progressively closer to ω_b . It is also known that the lowest characteristic natural frequency of the cloud dominates the frequency response. These were some of the most interesting results of the linearized analysis by d'Agostino and Brennen (1988a). We shall explore the influence of weak nonlinear effects on these phenomena.

A layer bounded by the oscillating wall on the interior and by incompressible liquid on the exterior is considered here (Fig. 2.15). Since the incompressible liquid

on the outer side is infinite in extent, it must always be at rest. It can be easily verified that the natural frequencies of such a bubble layer are given, in case of undamped bubble dynamics, by

$$\frac{\omega_n}{\omega_b} = \left[1 + \frac{3\alpha_o(1-\alpha_o)}{n^2\pi^2} \left(\frac{l}{R_o} \right)^2 \right]^{-\frac{1}{2}} ; n = 1, 2, \dots \quad (41)$$

With damping, the natural frequencies of the cloud differ from the above values by only a small amount. If the bubble layer has a finite thickness, l , the solution to Equation (29) has the following form

$$\frac{P_n}{\omega_b^2 R_o^2} = \Lambda(n) \left[a_n e^{-\lambda_n X/R_o} + b_n e^{\lambda_n(X-l)/R_o} \right] + f_{n3}(X) \quad (42)$$

where $f_{n3}(X)$ satisfies Equation (32). From Equation (26) and (42) we have

$$\frac{R_n}{R_o} = a_n e^{-\lambda_n X/R_o} + b_n e^{\lambda_n(X-l)/R_o} + [f_{n3}(X) - f_{n2}(X)]/\Lambda(n) \quad (43)$$

Using the first two terms of above equation to evaluate $f_{n1}(X)$ (Equation (25)) and $f_{n2}(X)$ ((27)) in Equation (32), $f_{n3}(X)$ can be solved exactly, the solution taking the form

$$f_{n3}(X) = \sum_{j=1}^{n-1} \left[\begin{aligned} & \zeta_1(n, j) a_j a_{n-j} e^{-(\lambda_j + \lambda_{n-j})X/R_o} \\ & + \zeta_2(n, j) a_j b_{n-j} e^{-\lambda_j X/R_o + \lambda_{n-j}(X-l)/R_o} \\ & + \zeta_2(n, j) b_j a_{n-j} e^{\lambda_j(X-l)/R_o - \lambda_{n-j}X/R_o} \\ & + \zeta_1(n, j) b_j b_{n-j} e^{(\lambda_j + \lambda_{n-j})(X-l)/R_o} \end{aligned} \right] \\ + \sum_{j=1}^{N-n} \left[\begin{aligned} & \zeta_3(n, j) \bar{a}_j a_{n+j} e^{-(\bar{\lambda}_j + \lambda_{n+j})X/R_o} \\ & + \zeta_4(n, j) \bar{a}_j b_{n+j} e^{-\bar{\lambda}_j X/R_o + \lambda_{n+j}(X-l)/R_o} \\ & + \zeta_4(n, j) \bar{b}_j a_{n+j} e^{\bar{\lambda}_j(X-l)/R_o - \lambda_{n+j}X/R_o} \\ & + \zeta_3(n, j) \bar{b}_j b_{n+j} e^{(\bar{\lambda}_j + \lambda_{n+j})(X-l)/R_o} \end{aligned} \right] \quad (44)$$

where

$$\zeta_1(n, j) = \frac{\lambda_n^2 \Theta(n, j)}{(\lambda_j + \lambda_{n-j})^2 - \lambda_n^2} \quad (45)$$

$$\zeta_2(n, j) = \frac{\lambda_n^2 \Theta(n, j)}{(\lambda_j - \lambda_{n-j})^2 - \lambda_n^2} \quad (46)$$

$$\zeta_3(n, j) = \frac{\lambda_n^2 \Gamma(n, j)}{(\lambda_j + \lambda_{n+j})^2 - \lambda_n^2} \quad (47)$$

$$\zeta_4(n, j) = \frac{\lambda_n^2 \Gamma(n, j)}{(\lambda_j - \lambda_{n+j})^2 - \lambda_n^2} \quad (48)$$

$$\Theta(n, j) = \Lambda(n) \left(\frac{1}{2} + 3\alpha_o \frac{2j-n}{2n} \right) - \beta_1(n, j) \quad (49)$$

$$\Gamma(n, j) = \Lambda(n) - \beta_2(n, j) \quad (50)$$

In linear analysis, Equation (43) may be written as

$$\frac{R_n}{R_o} = a_n e^{-\lambda_n X/R_o} + b_n e^{\lambda_n(X-l)/R_o} \quad (51)$$

This can be used in evaluating $f_{n2}(X)$, defined in Equation (27), and R_n/R_o can then be calculated using Equation (43). Using Equations (20), (42) and (44)

we get the following equation

$$\frac{\lambda_n}{3\alpha_o} \frac{X_n}{R_o} = -a_n e^{-\lambda_n X/R_o} + b_n e^{\lambda_n X/R_o}$$

$$+ \sum_{j=1}^{n-1} \begin{bmatrix} -\kappa_1(n, j) a_j a_{n-j} e^{-(\lambda_j + \lambda_{n-j})X/R_o} \\ -\kappa_2(n, j) a_j b_{n-j} e^{-\lambda_j X/R_o + \lambda_{n-j}(X-l)/R_o} \\ +\kappa_2(n, j) b_j a_{n-j} e^{\lambda_j(X-l)/R_o - \lambda_{n-j}X/R_o} \\ +\kappa_1(n, j) b_j b_{n-j} e^{(\lambda_j + \lambda_{n-j})(X-l)/R_o} \end{bmatrix} \quad (52)$$

$$+ \sum_{j=1}^{N-n} \begin{bmatrix} -\kappa_3(n, j) \bar{a}_j a_{n+j} e^{-(\bar{\lambda}_j + \lambda_{n+j})X/R_o} \\ -\kappa_4(n, j) \bar{a}_j b_{n+j} e^{-\bar{\lambda}_j X/R_o + \lambda_{n+j}(X-l)/R_o} \\ +\kappa_4(n, j) \bar{b}_j a_{n+j} e^{\bar{\lambda}_j(X-l)/R_o - \lambda_{n+j}X/R_o} \\ +\kappa_3(n, j) \bar{b}_j b_{n+j} e^{(\bar{\lambda}_j + \lambda_{n+j})(X-l)/R_o} \end{bmatrix}$$

where

$$\kappa_1 = \frac{\lambda_n (\lambda_j + \lambda_{n-j}) \Theta(n, j)}{\Lambda(n) \left((\lambda_j + \lambda_{n-j})^2 - \lambda_n^2 \right)} \quad (53)$$

$$\kappa_2 = \frac{\lambda_n (\lambda_j - \lambda_{n-j}) \Theta(n, j)}{\Lambda(n) \left((\lambda_j - \lambda_{n-j})^2 - \lambda_n^2 \right)} \quad (54)$$

$$\kappa_3 = \frac{\lambda_n (\bar{\lambda}_j + \lambda_{n+j}) \Gamma(n, j)}{\Lambda(n) \left((\bar{\lambda}_j + \lambda_{n+j})^2 - \lambda_n^2 \right)} \quad (55)$$

$$\kappa_4 = \frac{\lambda_n (\bar{\lambda}_j - \lambda_{n+j}) \Gamma(n, j)}{\Lambda(n) \left((\bar{\lambda}_j - \lambda_{n+j})^2 - \lambda_n^2 \right)} \quad (56)$$

The boundary conditions for solving Equation (52) are (i) the given wall oscillation amplitude at $x = 0$, and (ii) the oscillation of the fluid at the exterior of the layer as zero. The constants $\zeta_1 - \zeta_4$ and $\kappa_1 - \kappa_4$ can be evaluated using their definitions for given fluid and bubble properties. Thus, applying the boundary conditions, a set of nonlinear algebraic equations is obtained for a_n and b_n . These are solved

using a Newton–Raphson scheme. Since Equation (52) is similar to Equation (37), it can be seen that the solution is independent of the way in which the frequency domain is discretized. As before, the solution consists of nonzero amplitudes only at the harmonics of the excitation frequency.

Having calculated a_n and b_n , $P_n/\omega_b^2 R_o^2$ can be calculated using Equation (42) and R_n/R_o obtained using Equation (43). The frequency response of the bubbly layer was calculated by varying the wall oscillation frequency from $\omega_b/100$ to $2\omega_b$. Calculation up to 20 harmonics was found to be sufficient, harmonics of higher order being negligible.

A typical frequency response of the bubble cloud of finite thickness is shown in Fig. 2.16. The values for the water tunnel conditions given in Table 2.1 have been used. The frequency response is shown in the same manner as earlier in Figs. 2.4 and 2.6. The first and second harmonics are marked as [1] and [2]. The amplitudes of higher order harmonics are negligible in comparison. The first harmonic is similar to that predicted by the linear solution. For both the pressure and the radius response, significant amplitudes of oscillation can be observed at the characteristic natural frequencies of the cloud with the response at the lowest natural frequency being dominant. It is also observed that the response at the characteristic natural frequencies close to ω_b are overwhelmed by the response modification that is due to proximity of ω_b , making it impossible to distinguish the peaks at characteristic natural frequencies close to ω_b . Also, the response at the second harmonic of the lowest characteristic natural frequency (at $2\omega_1$) is greater than the response at other natural frequencies of the bubble cloud. The response for excitation frequencies close to and greater than ω_b is similar to that for the bubble layer of infinite thickness discussed in Section 2.4.

In other words, the most significant frequency is the lowest natural frequency of the cloud and even weak nonlinear effects cause the harmonics of this frequency to dominate the other natural cloud frequencies. Since, the second harmonic re-

sponse at $2\omega_1$ is not highly damped, there remain some important high frequencies such as $2\omega_1$. This is the main addition to the results of the linearized analysis of d'Agostino and Brennen (1988a).

Following d'Agostino and Brennen (1988a), the flow solution is divided into 3 different regimes, namely: *sub-resonant* ($0 < \omega_f < \omega_1$), *trans-resonant* ($\omega_1 < \omega_f < \omega_b$) and *super-resonant* ($\omega_f > \omega_b$). The first and second harmonics of the radius oscillation and the pressure oscillation are shown as surface plots in Figs. 2.17 and 2.18, respectively. The amplitude of a harmonic is plotted as function of the frequency ratio, ω/ω_b and the distance from the wall, X/l in these figures to understand the frequency response of the cloud away from the oscillating wall. In cases of the *sub-resonant* and *trans-resonant* excitation, the amplitudes of oscillation form standing wave patterns, whose amplitude decays slowly with distance from the wall. In case of *super-resonant* excitation, the response is seen to decay rapidly with distance from the wall.

The response to *sub-resonant* and *trans-resonant* excitation for spherical bubble clouds was seen to decay rapidly with distance from the center of the cloud (d'Agostino and Brennen (1988a)). Comparing the response of a spherical cloud and the present flat layer, it appears that the strong decay at a distance from the bubble center in the case of a spherical cloud is caused by attenuation that is due to spherical divergence. In other words, the response at the center of the spherical cloud is much stronger than the response at the boundary of the cloud because of the focussing of the spherically symmetric disturbance. Thus, for *sub-resonant* and *trans-resonant* excitations the magnitude of the response is determined by the geometry of the bubble cloud and the excitation. The bubbles have ample time to react to the excitation, and the bubble dynamics significantly influences the response throughout the layer. In the case of *super-resonant* excitation, the response is seen to decay rapidly with the distance from the oscillating wall in the same way as it decayed rapidly with the distance from the boundary of a spherical

cloud (d'Agostino and Brennen (1988a)). Thus, in the case of *super-resonant* excitation, the response gets weaker with increasing distance from the source of excitation. In this case, the excitation is too fast for bubbles to follow and the bubbles act *stiff*. Thus, the bubble dynamics does not play any significant role except in dissipation of the input energy.

The effects of variation in the viscous parameter $\nu/\omega_b R_o^2$ and the surface tension parameter $S/\rho\omega_b^2 R_o^3$ are indicated in Figs. 2.19 and 2.20. The two sets of data used for comparison are the same as given in Table 2.1 for the earlier case of bubble layer of infinite thickness, namely, the water tunnel conditions and the ocean conditions. Again, higher values of viscous and surface tension parameters are seen to inhibit pressure and bubble radius oscillations at the characteristic natural frequencies of the bubble cloud. It is also important to note that the effect of change in viscous and surface tension parameters are significant only near the characteristic natural frequencies of the cloud.

As can be seen from Equation (41), the spread of the natural frequencies of the cloud is determined by the value of the parameter $3\alpha_o(1 - \alpha_o)(l/R_o)^2$; a similar behavior was observed for the spherical bubble clouds (d'Agostino and Brennen (1988a)). For a given value of the void fraction and the bubble radius, the layer with the larger thickness has smaller characteristic natural frequencies. The effect of variation in the thickness of the bubble layer, l/R_o , for a given value of the void fraction will be examined next, followed by observations on the effect of the void fraction, α_o , for a given value of the thickness to bubble radius ratio, l/R_o .

Figs. 2.21 and 2.22 show the changes in frequency response of the layer because of the increase in its thickness. The increase in the thickness results in lower natural frequencies of the cloud, as can be expected from Equation (41). It is clear from the Figs. 2.21 and 2.22 that the change in the thickness of the layer does not influence the frequency response for *super-resonant* excitation and

for excitation frequencies close to ω_b . In order to investigate this, consider the response of the fundamental harmonic shown in Fig. 2.21. The amplitude of oscillation is a maximum at the lowest cloud natural frequency, ω_1 , in cases for which ω_1 is greater than $0.5\omega_b$. However, the amplitude of oscillation at ω_2 is greater than at ω_1 in the case for which ω_1 is about $0.25\omega_b$. It appears that the amplitude of oscillation at a cloud natural frequency increases as that cloud natural frequency gets closer to about $0.5\omega_b$. The response at the second harmonic shown in Fig. 2.22 also appears to follow the same pattern. This explains the change of this solution for a layer of finite thickness to the solution for an infinitely thick layer. The cloud natural frequencies move to values much less than $0.5\omega_b$ with increase in the thickness of the layer, and the amplitude of oscillation at these cloud natural frequencies reduces to the same value as in the case of an infinitely thick layer.

Figs. 2.23 and 2.24 illustrate the effect of change in the void fraction on the frequency response of the layer. An increase in the value of void fraction reduces the characteristic natural frequencies, which is also obvious from Equation (41). The amplitude of oscillation is reduced by an increase in the void fraction for excitation frequencies close to and greater than ω_b . Also, two other features of Fig. 2.23 are noteworthy. First, the amplitude of pressure oscillation at ω_1 is larger for the void fraction of 0.020 than for the void fraction of 0.005. The possible reason for this is the proximity of ω_1 to $0.5\omega_b$ for the void fraction of 0.020. Second, the amplitude of oscillation at ω_1 is larger than at ω_2 for the void fraction of 0.1, which is contrary to the result for $\alpha_o = 0.02$ and $l/R_o = 50$ seen earlier in Fig. 2.21. Thus, it appears that both the proximity of the cloud natural frequencies to $0.5\omega_b$ and the void fraction influence the relative amplitudes of oscillation at ω_1 and ω_2 .

Lastly, the effect of the amplitude of wall oscillation $X_n(0)/R_o$ is shown in Figs. 2.25 and 2.26. Larger amplitudes increase the amplitude of pressure and radius oscillation at all frequencies just as expected. Some new enhanced

frequencies around $0.55\omega_b$ and $0.8\omega_b$ can be seen in Fig. 2.26 for the largest amplitude of wall oscillation.

Because of the limitations on the solution which restrict the validity to $|R_n/R_o| \ll 1$, further changes in the frequency response due to reduction in α_o or increase in $X_n(0)/R_o$, $\nu/\omega_b R_o^2$ and $S/\rho\omega_b^2 R_o^3$ could not be investigated.

2.6. A Semi-infinite Layer with Bubble Size Distribution

Most of the research efforts in modeling bubbly mixtures so far have assumed bubbly mixtures of identical bubbles. In most practical cases, uniformly sized bubbles are impossible to achieve. The free nuclei in water have a distribution of the bubble sizes (Gates and Acosta (1978)). Recently Maeda *et al.* (1991) have used holography to measure the distribution of bubble sizes in cavitation clouds. The bubble size distribution can be described by

$$\eta(R_o) = \frac{N^*}{R_o^m} \quad (57)$$

The distribution of the form given by Equation (57) has been used to describe the nuclei number distribution in sea water and different water tunnel facilities with $N \approx 0.00001$ and $m \approx 3 \rightarrow 4$ (Brennen and Ceccio (1989)). This section presents a weakly nonlinear model of flows of such bubbly mixtures. Since such flows have a number of length and time scales in terms of the bubble radii and their natural periods, we can expect different mechanisms linking the interaction between different time scales. Such an interaction leads to a new physical phenomenon termed *harmonic cascading*.

In this model we assume that the bubble number density distribution for equilibrium size per unit liquid volume, $\eta(R_o)$, is given. This quantity is assumed to be uniform and constant. The relative velocity between the phases and the compressibility of the medium have been neglected in order to keep the equations simple. These assumptions have been discussed in detail in Section 2.4. The number of bubbles per unit liquid volume with equilibrium size between R_o and $R_o + dR_o$ is given by $\eta(R_o) dR_o$. The volume of bubbles per unit liquid volume

can then be written as

$$\frac{\alpha}{1-\alpha} = \int_{R_m}^{R_M} \eta(R_o) \tau dR_o \quad (58)$$

where the volume of the bubble, τ , is given by Equation (15) and R_m and R_M are the minimum and the maximum value for the radius of the bubbles present in the layer. Thus, the number of bubbles per unit total volume with equilibrium radius between R_o and $R_o + dR_o$, $\eta^*(R_o) dR_o$, can be written as

$$\eta^*(R_o) dR_o = \eta(R_o) (1-\alpha) dR_o = \frac{\eta(R_o) dR_o}{1 + \int_{R_m}^{R_M} \eta(R_o) \tau dR_o} \quad (59)$$

We use a dispersed phase number continuity equation (DPNC) to model mass and number conservation. Assuming the liquid to be incompressible, the dispersed phase number continuity equation, which assumes that the bubbles are neither created nor destroyed is

$$\frac{D}{Dt} \int_{R_m}^{R_M} \eta^*(R_o) dR_o + \frac{\partial u}{\partial x} \int_{R_m}^{R_M} \eta^*(R_o) dR_o = 0 \quad (60)$$

Assuming that the number density per unit total volume is conserved, the above equation reduces to

$$\frac{D\eta^*(R_o)}{Dt} + \eta^*(R_o) \frac{\partial u}{\partial x} = 0 \quad (61)$$

The corresponding momentum equation is given by

$$\rho(1-\alpha) \frac{Du}{Dt} = -\frac{\partial p}{\partial x} \quad (62)$$

The solution to the problem represented by (2), (59) (61) and (62) is solved in Lagrangian coordinates, X and T , as described earlier in Section 2.4. The above equations become

$$\frac{\partial \eta^*(R_o)}{\partial T} \frac{\partial x}{\partial X} + \eta^*(R_o) \frac{\partial u}{\partial X} = 0 \quad (63)$$

and

$$\rho \frac{\partial u}{\partial T} \frac{\partial x}{\partial X} = -\frac{1}{1-\alpha} \frac{\partial P}{\partial X} \quad (64)$$

Also using Equation (15) we can write

$$\int_{R_m}^{R_M} \eta(R_o) \tau dR_o = \int_{R_m}^{R_M} \eta(R_o) \left[\tau_o + \sum_{n=1}^N \Re(\tau_n(X) e^{in\delta T}) \right] dR_o \quad (65)$$

Following Equation (58) this can be written as

$$\int_{R_m}^{R_M} \eta(R_o) \tau dR_o = \frac{\alpha_o}{1 - \alpha_o} + \sum_{n=1}^N \Re(A_n e^{in\delta T}) \quad (66)$$

where

$$A_n = \int_{R_m}^{R_M} \eta(R_o) \tau_n dR_o \quad (67)$$

Equations (14), (15), (16), (59) and (66) are substituted into the dispersed phase number continuity equation (Equation (63)), and coefficients of $e^{in\delta T}$ are equated to obtain

$$\begin{aligned} \frac{dX_n}{dX} = & (1 - \alpha_o) A_n + \frac{(1 - \alpha_o)}{2} \sum_{j=1}^{n-1} \frac{2j - n}{2n} A_j \frac{dX_{n-j}}{dX} \\ & + \frac{(1 - \alpha_o)}{2} \sum_{j=1}^{N-n} \frac{2j + n}{n} \left[A_{n+j} \frac{d\bar{X}_j}{dX} - \bar{A}_j \frac{dX_{n+j}}{dX} \right] \end{aligned} \quad (68)$$

Similar substitution into the momentum equation (Equation (64)) leads to

$$\begin{aligned} \frac{dP_n}{dX} = & (1 - \alpha_o) n^2 \delta^2 X_n \\ & + \frac{(1 - \alpha_o)}{2} \sum_{j=1}^{n-1} \left[j^2 \delta^2 X_j \frac{dX_{n-j}}{dX} - A_{n-j} \frac{dP_j}{dX} \right] \\ & + \frac{(1 - \alpha_o)}{2} \sum_{j=1}^{N-n} \left[\begin{aligned} & j^2 \delta^2 \bar{X}_j \frac{dX_{n+j}}{dX} \\ & + (n+j)^2 \delta^2 X_{n+j} \frac{d\bar{X}_j}{dX} \\ & - A_{n+j} \frac{d\bar{P}_j}{dX} - \bar{A}_j \frac{dP_{n+j}}{dX} \end{aligned} \right] \end{aligned} \quad (69)$$

Note that in the linear approximation, Equations (68) and (69) become

$$\frac{dX_n}{dX} = (1 - \alpha_o) A_n \quad (70)$$

$$\frac{dP_n}{dX} = (1 - \alpha_o) n^2 \delta^2 X_n \quad (71)$$

It is consistent with the level of approximation to substitute these first order expressions into quadratic terms in Equations (68) and (69), which can then be

written as

$$\frac{d(X_n/l_r)}{d(X/l_r)} = (1 - \alpha_o) A_n + \frac{(1 - \alpha_o)^2}{2} \sum_{j=1}^{n-1} \frac{2j - n}{n} A_j A_{n-j} + O(3) \quad (72)$$

and

$$\frac{d(P_n/\omega_r^2 l_r^2)}{d(X/l_r)} = (1 - \alpha_o) \left(\frac{n\delta}{\omega_r} \right)^2 \left(\frac{X_n}{l_r} \right) + O(3) \quad (73)$$

Here, ω_r and l_r are the reference frequency and length scales used for nondimensionalizing the results. Using Equations (23) and Equation (5) and the linear part of Equation (5) to approximate R_n/R_o , we arrive at

$$\begin{aligned} \frac{\tau_n}{\tau_o} = & 3 \frac{P_n}{\Lambda(n) \omega_b^2 R_o^2} + 3 \sum_{j=1}^{n-1} \left[\frac{1}{2} - \frac{\beta_1(n, j)}{\Lambda(n)} \right] \frac{P_j P_{n-j}}{\omega_b^4 R_o^4 \Lambda(j) \Lambda(n-j)} \\ & + 3 \sum_{j=1}^{N-n} \left[1 - \frac{\beta_2(n, j)}{\Lambda(n)} \right] \frac{\overline{P}_j P_{n+j}}{\omega_b^4 R_o^4 \overline{\Lambda}(j) \Lambda(n+j)} \end{aligned} \quad (74)$$

Using Equations (67) and (74), we arrive at the following:

$$A_n = \phi'(n) \frac{P_n}{\omega_r^2 l_r^2} + \sum_{j=1}^{n-1} \psi'(n, j) \frac{P_j}{\omega_r^2 l_r^2} \frac{P_{n-j}}{\omega_r^2 l_r^2} + \sum_{j=1}^{N-n} \theta'(n, j) \frac{\overline{P}_j}{\omega_r^2 l_r^2} \frac{P_{n+j}}{\omega_r^2 l_r^2} \quad (75)$$

where $\phi'(n)$, $\psi'(n, j)$ and $\theta'(n, j)$ are given by

$$\phi'(n) = \int_{R_m}^{R_M} \frac{3\eta(R_o) \tau_o \omega_r^2 l_r^2}{\Lambda(n) \omega_b^2 R_o^2} dR_o \quad (76)$$

$$\psi'(n, j) = \int_{R_m}^{R_M} \frac{3\eta(R_o) \tau_o \omega_r^4 l_r^4}{\Lambda(j) \Lambda(n-j) \omega_b^4 R_o^4} \left[\frac{1}{2} - \frac{\beta_1(n, j)}{\Lambda(n)} \right] dR_o \quad (77)$$

$$\theta'(n, j) = \int_{R_m}^{R_M} \frac{3\eta(R_o) \tau_o \omega_r^4 l_r^4}{\overline{\Lambda}(j) \Lambda(n+j) \omega_b^4 R_o^4} \left[1 - \frac{\beta_2(n, j)}{\Lambda(n)} \right] dR_o \quad (78)$$

Using Equations (72), (73) and (75) and the linear part of Equation (75) to evaluate A_n in quadratic terms, we have following equation,

$$\frac{d^2(P_n/\omega_r^2 l_r^2)}{d(X/l_r)^2} = \lambda_n^2 \frac{P_n}{\omega_r^2 l_r^2} + \sum_{j=1}^{n-1} \psi(n, j) \frac{P_j}{\omega_r^2 l_r^2} \frac{P_{n-j}}{\omega_r^2 l_r^2} + \sum_{j=1}^{N-n} \theta(n, j) \frac{\overline{P}_j}{\omega_r^2 l_r^2} \frac{P_{n+j}}{\omega_r^2 l_r^2} \quad (79)$$

where

$$\lambda_n^2 = (1 - \alpha_o)^2 \left(\frac{n\delta}{\omega_r} \right)^2 \phi'(n) \quad (80)$$

$$\psi(n, j) = (1 - \alpha_o)^2 \left(\frac{n\delta}{\omega_r} \right)^2 \left[\psi'(n, j) + (1 - \alpha_o) \frac{2j - n}{2n} \phi'(j) \phi'(n - j) \right] \quad (81)$$

$$\theta(n, j) = (1 - \alpha_o)^2 \left(\frac{n\delta}{\omega_r} \right)^2 \theta'(n, j) \quad (82)$$

Equation (79) has the following approximate solution (accurate to the second order and obtained in manner similar to the solution to Equation (24) given by Equation (30))

$$\begin{aligned} \frac{P_n}{\omega_r^2 l_r^2} = & c_n e^{-\lambda_n X/l_r} + \sum_{j=1}^{n-1} \frac{\psi(n, j) c_j c_{n-j}}{(\lambda_j + \lambda_{n-j})^2 - \lambda_n^2} e^{-(\lambda_j + \lambda_{n-j})X/l_r} \\ & + \sum_{j=1}^{N-n} \frac{\theta(n, j) \bar{c}_j c_{n+j}}{(\bar{\lambda}_j + \lambda_{n+j})^2 - \lambda_n^2} e^{-(\bar{\lambda}_j + \lambda_{n+j})X/l_r} \end{aligned} \quad (83)$$

Using the solution given by Equation (83) and relation (73), the following relation for the conditions at the wall may be obtained:

$$\begin{aligned} -(1 - \alpha_o) \left(\frac{n\delta}{\omega_r} \right)^2 \frac{X_n(0)}{l_r} = & \lambda_n c_n + \sum_{j=1}^{n-1} \frac{(\lambda_j + \lambda_{n-j}) \psi(n, j) c_j c_{n-j}}{(\lambda_j + \lambda_{n-j})^2 - \lambda_n^2} \\ & + \sum_{j=1}^{N-n} \frac{(\bar{\lambda}_j + \lambda_{n+j}) \theta(n, j) \bar{c}_j c_{n+j}}{(\bar{\lambda}_j + \lambda_{n+j})^2 - \lambda_n^2} \end{aligned} \quad (84)$$

In the case of identical bubbles, we have

$$\eta(R_o) = \eta' \delta (R_o - R'_o) \quad (85)$$

where η' is the total number of bubbles per unit liquid volume and R'_o is the radius of the bubbles. It can be seen that above result reduces to that for identical bubbles given in Section 2.4. Using Equation (85), Equations (83) and (84) can be respectively reduced to Equations (30) and (37).

For the purpose of evaluating typical results from this analysis, a bubble cloud is assumed to contain bubbles between radii 10.0 μm and 100.0 μm . The ambient conditions are the same as listed in Table 2.1 so far as ambient pressures

are concerned. Other values no longer apply. The largest natural frequency of the bubble and the largest bubble radius present in the cloud are chosen as a convenient reference frequency, ω_r and reference length scale, l_r respectively.

For a given bubble size distribution, ambient conditions and fluid properties, the coefficients, $\phi'(n)$, $\psi'(n, j)$ and $\theta'(n, j)$ are evaluated using Equations (76), (77) and (78) respectively. The integrals were evaluated numerically the using trapezoidal rule, and the Richardson extrapolation was used to estimate the value of the integral for zero step size. The parameters Λ_n , $\beta_1(n, j)$ and $\beta_2(n, j)$ have been defined earlier by Equations (7), (8) and (9), respectively. Now, λ_n , $\psi(n, j)$ and $\theta(n, j)$ can be calculated using Equations (80)–(82). Equation (84) is solved using the Newton–Raphson scheme to calculate the constants c_n for a given amplitude of wall oscillation, $X_n(0)/l_r$. Knowing c_n , the amplitude of pressure oscillation can be calculated from Equation (83). Using this solution, the values of R_n/R_o are calculated for different values of R_o , using Equation (31). The amplitude of R_n/R_o is checked to be less than 1 to insure validity of the solution. Equation (84) is similar in structure to Equations (5) and (37), and the solution is nonzero only at the harmonics of the excitation frequency. Once again, calculations of up to 20 harmonics were found to be sufficient, harmonics of higher order being negligible. The check on $|R_n/R_o|$ is performed only for the those bubbles for which the frequencies present (excitation frequency and its harmonics) are natural frequencies.

Numerical results were computed for a number of typical cases. For each case the results were obtained for the size distribution density slope, $m = 2, 3, 4$ and the value of N^* was adjusted to give the void fraction for the case. The results for six different cases were calculated in order to investigate the effect of changes in void fraction, ambient conditions and amplitude of wall oscillation. The excitation frequency is varied between $\omega_r/100$ and $1.25\omega_r$ in order to calculate the frequency response.

A typical frequency response of the cloud is shown in Fig. 2.27 for ambient conditions for a water tunnel given in Table 2.1. The main features of the frequency response are the same for both of the ambient conditions for the water tunnel and the ocean.

Fig. 2.27 shows the amplitude of pressure oscillation for the fundamental and the second harmonic, which are marked [1] and [2], respectively, as well as the solution obtained from the linearized analysis, which is marked [L]. The amplitudes of higher harmonics were found to be negligible. The frequency ratio is the ratio of the actual frequency at which the response occurs to the reference frequency, similar to Figs. 2.4 and 2.6. It is seen that the amplitude of the first harmonic pressure oscillation increases with increasing excitation frequency. The number of bubbles is larger for the smaller size for which the natural frequency of the bubble is larger. Thus, for a larger frequency ratio, or excitation frequency, a larger number of bubbles are excited at their natural frequency, thus leading to an increase in amplitude of the pressure oscillation. The *stiff* behavior of bubbles whose natural frequencies are less than the excitation frequency (seen in Section 2.4 as a response to the *super-resonant* excitation) also contributes to an increase in amplitude of the pressure oscillation.

When the wall is oscillated at a frequency, ω_f , the bubbles with their natural frequency equal to ω_f are excited with the largest amplitude. Because of the nonlinearity present in the system, the flow variables oscillate at the harmonics of the excitation frequency, ω_f . Thus, the pressure oscillation at $2\omega_f$ excites bubbles with their natural frequency equal to $2\omega_f$. Since the number of bubbles with the natural frequency, $2\omega_f$, is larger than the number of bubbles with the natural frequency, ω_f , the response resulting from the bubbles with a natural frequency of $2\omega_f$ may be significant and may be larger for larger values of m . In other words, the excitation may cascade its way to higher frequencies. This mechanism is termed as *harmonic cascading* for the rest of the discussion.

The amplitude of oscillation of the second harmonic is shown in Fig. 2.27. The ratio of amplitude of the second harmonic to the amplitude of the first harmonic increases for larger values of size density distribution slope, m . This may be expected from the mechanism of *harmonic cascading* described above. Also, the linear solution is larger than the first harmonic, and the difference between the linear solution and the first harmonic is larger for larger values of m . For excitation frequencies larger than the reference frequency, ω_r , the amplitude of the second harmonic is very small and the difference between the linear and nonlinear solutions is also very small. This may be expected since ω_r is the highest natural frequency present in the cloud, and the effect of *harmonic cascading* is expected to decrease for wall oscillation frequencies larger than $0.5\omega_r$. For excitation frequencies up to $0.5\omega_r$, *harmonic cascading* remains an important effect with the amplitude of the second harmonic becoming larger than the amplitude of the first harmonic for $m = 4$. For excitation frequencies larger than $0.5\omega_r$, the increase is due to the collective response of the bubbles to the excitation.

Fig. 2.28 presents the amplitude of pressure oscillation for the first and the second harmonic as a function of the frequency ratio, ω/ω_r and the distance from the wall, X/l_r . It is quite clear that the pressure oscillation decays rapidly away from the wall, decaying to very small values at the distance of $4l_r$ from the wall.

The frequency responses for different values of the size density distribution slope, m , are compared in the Fig. 2.29. The void fraction is the same for all cases. It appears that an increase in the value of m reduces the amplitude of the first harmonic. For a given value of the void fraction, the number of bubbles is larger for larger values of m , and reduction in the amplitude of the pressure oscillation may be caused by the increased number of bubbles since that increases damping in the system. The weaker response for increased void fraction seen earlier for a layer of identical bubbles may also be caused by an increase in the number of bubbles. Also, the amplitude of the second harmonic is not influenced strongly by

change in the value of m .

The effect of ambient conditions on the frequency response of the bubble layer is shown in Figs. 2.30 and 2.31. It is clear that the changes in ambient conditions do not strongly influence the frequency response of the layer. However, it does appear that ambient conditions at the ocean do promote a little stronger *harmonic cascading*. This may be explained as follows. The *super-resonant* excitation of bubbles that have a natural frequency less than the excitation frequency, contributes significantly to the amplitude of the fundamental harmonic and this is not strongly influenced by reduction in the viscous and surface tension parameters at ocean conditions. However, bubble dynamics plays a stronger role in generation of the second harmonic through *harmonic cascading*, and thus increase in the amplitude of the second harmonic with a reduced effect of viscosity and surface tension at ocean conditions may be expected. Hence, stronger *harmonic cascading* at the ocean conditions can be expected.

The effect of changes in the void fraction on the frequency response of the layer is shown in Figs. 2.32 and 2.33. A larger value of the void fraction produces a weaker response. The effect of change in the amplitude of the wall oscillation is shown in Figs. 2.34 and 2.35. Just as in the case of a layer with identical bubbles, larger wall oscillations produce stronger pressure oscillations.

2.7. Summary

In this work some of the nonlinear effects, which can occur when a plane wall bounding a bubbly liquid oscillates in a direction normal to itself, have been investigated. Specifically, these effects have been examined in terms of bubble radius and pressure oscillations. The principal results are summarized below.

The presence of a finite length scale such as the finite thickness of the bubble layer results in characteristic natural frequencies of the bubble layer (known as cloud natural frequencies) all of which are less than the bubble natural frequency,

ω_b . Natural frequencies are determined mainly by the void fraction and the ratio of thickness of the layer to the bubble radius. The dominant response occurs for excitation at the lowest cloud natural frequency. The response is dominated by the first and the second harmonic components. The amplitude of the response increases as the lowest natural frequency gets closer to about $0.5\omega_b$. The cloud natural frequencies are very small for large thickness to bubble radius ratio and the frequency response becomes the same as for an infinitely thick layer.

For excitation frequencies in the *sub-resonant* and *trans-resonant* regimes ($\omega < \omega_b$), the amplitude of oscillation forms standing wave patterns in the layer in which the amplitude slowly decays with distance from the oscillating wall. However, for *super-resonant* excitation the oscillation amplitude decays rapidly with distance from the source of excitation. This rapid decay is caused by the reduced effect of bubble dynamics in the *super-resonant* regime in which the bubbly layer behaves like a homogeneous compressible layer.

The phenomenon of *harmonic cascading* is seen to take place in a bubbly mixture containing bubbles of different sizes. *Harmonic cascading* occurs when a low frequency excitation applied to the layer at a frequency, ω_f , results in a large amplitude of oscillation at the frequency of $2\omega_f$ because of the presence of a large number of bubbles with a natural frequency of $2\omega_f$. The ratio of the amplitude of the second harmonic to the amplitude of the first harmonic defines the extent of *harmonic cascading*. This ratio increases with an increase in the number of bubbles with small radii relative to the number of bubbles with large radii. It is noteworthy that the phenomenon of *harmonic cascading* can be modelled only by a nonlinear model because the linearized models do not allow for frequency dispersion.

Larger values of the void fraction cause a reduction in the amplitude of pressure and radius oscillation in all cases. This may imply reduced acoustic noise in bubbly mixtures and damage potential in cavitating flows. The reduction

of acoustic noise at increased void fraction has been observed experimentally by Arakeri and Shanmuganathan (1985). A larger number of bubbles present at large void fraction may cause stronger dissipation and a reduced amplitude of oscillation.

2.8. Limitations

In this section we shall examine the various limitations of the present model. First, the present model is based on continuum mechanics. This requires that the bubble spacing be much smaller than the shortest characteristic length scale present in the flow. Hence, bubble spacing is required to be much less than the thickness of the bubble layer. The wavelength of disturbances is required to be much larger than the bubble size in order to insure a spherically symmetric disturbance for each bubble assumed in the present theory. This holds true for excitation frequencies far above the linear resonance frequency of the bubble, and so the condition is easily satisfied.

The local pressure disturbance resulting from volume oscillations of neighboring bubbles is assumed to be negligible as compared to the global pressure fluctuations. d'Agostino and Brennen (1988a) have given a condition for this assumption to be satisfied. This condition is generally satisfied in low void fraction flows for small amplitude oscillation (d'Agostino and Brennen (1988a)).

The amplitude of the radius oscillation is required to be small; in particular, $|R_n/R_o| < 1$ must be satisfied. This is also required to avoid the following instability in the bubble dynamics. For pressure oscillations exceeding a threshold value, bubbles larger than a critical size have been known to grow to a large size and then collapse violently (Flynn(1964), Eller and Flynn(1969) and Brennen and Ceccio (1989)). Such bubbles have been referred to as transient cavities in the literature. Bubble oscillation does not grow into collapse of a transient cavity if the ratio of the maximum size of the bubble to the equilibrium bubble radius does not exceed 2.0 (Flynn (1964)). The effect of damping is also reduced for large

bubbles. These place an upper limit on the excitation, which is smaller for large bubbles. In practice, $|R_n/R_o| < 1$ is expected to dictate the maximum applicable excitation for a given bubble size, for which the theory remains applicable.

The range of void fraction, for which the present theory may be applied, is also bounded by an upper and a lower limit. The lower limit of the void fraction is determined by the maximum bubble separation required under continuum assumption as well as the requirement of a maximum permissible amplitude of radius oscillation, $|R_n/R_o|$. The upper limit on void fraction is determined by the requirement of local pressure disturbance to be negligible in comparison to the global pressure oscillation (d'Agostino and Brennen (1988a)).

The phenomenon of rectified diffusion results in slow growth of the equilibrium size of a bubble (Hsieh and Plesset (1961)). Thus, the theory can be applied to the bubbly layers subject to steady state oscillation for long periods only if the equilibrium size, R_o is tracked and the values appropriate to a particular time are employed.

2.9 Practical Applications

The theory may also be applied in order to understand the behavior of the dense cavitation clouds shed in cavitating foils and the cloud formed by breakup of the collapsing bubble in the travelling bubble cavitation. Also, the bubbly mixtures are found in a number of industrial applications. Some ultrasonic devices used in sono-chemistry involve bubbly mixtures subject to periodic disturbances.

In cavitating flows, the typical value of void fraction is much less than 1% and the bubble sizes vary between $10 \mu m$ and $150 \mu m$. In view of the discussion given above (Section 2.8), the present theory is valid for small excitations. For example, the amplitude of wall oscillation was limited to less than a few percent of the equilibrium bubble radius in the present problems. The maximum allowed excitation, for the theory to remain applicable, is proportional to the void fraction

and inversely proportional to the bubble radius. The main results from the theory remain unaltered as long as $R_n/R_o < 1$ is satisfied.

In spite of being limited to small amplitude oscillations and thus to a small excitation, the results from the theory may be used to understand qualitatively the response of bubbly mixtures in practical situations. In particular, *harmonic cascading* should be present in many practical situations. Figs. 2.36 and 2.37 show two examples of spectra reported in the literature where *harmonic cascading* may be responsible for the features of the spectra. Fig. 2.36 shows the spectra of noise that is due to cavitation produced by a rotating rod in the Thames river (Mellen (1954)). It contains peaks at 1.25, 2.50 and 5.0 *kHz* (marked respectively as (1), (2) and (3)). The peaks at 1.25 and 2.5 *kHz* are of equal magnitude, and the peak at 2.5 *kHz* may have been caused by *harmonic cascading*, though Mellen has cited possibility of interference resulting from reflected waves as a reason. The second example (Fig. 2.37) has been taken from Blake (1986) and shows spectra of noise that is due to cavitation on the suction side of a propeller blade. The peaks at 8.5, 17 and 34 *kHz* (marked (1), (2), (3)) may be due to *harmonic cascading*. The results of Arakeri and Shanmuganathan (1985) do not exhibit *harmonic cascading*. However, that may be due to lack of variation in the size of bubbles generated by electrolysis. Most of the spectra measurement reported in the literature have been made using half-octave frequency resolution. Clearly, a finer spectra resolution in the spectra measurement is required in order to resolve *harmonic cascading* unambiguously.

The upper limit of the validity of the present theory also serves as the threshold above which catastrophic growth and collapse of cavitation bubbles may be seen in practical flow situations.

Table 2.1

Fluid and Bubble Parameters for the Examples Presented

These data are for water at 20° C.

Data Set	Application	R_o (μm)	P_o (Pa)	k	$\nu/\omega_b R_o^2$	$S/\rho\omega_b^2 R_o^3$
I	Water Tunnel	14	13146	1	0.01	0.10
II	Ocean	20	101325	1	0.0028	0.012

Other Data:

$$\nu = 0.000001 \text{ Kg}/(m.s)$$

$$S = 0.0734 \text{ N}/m$$

$$\rho = 1000.0 \text{ Kg}/(m^3)$$

$$P_v = 2339 \text{ Pa}$$

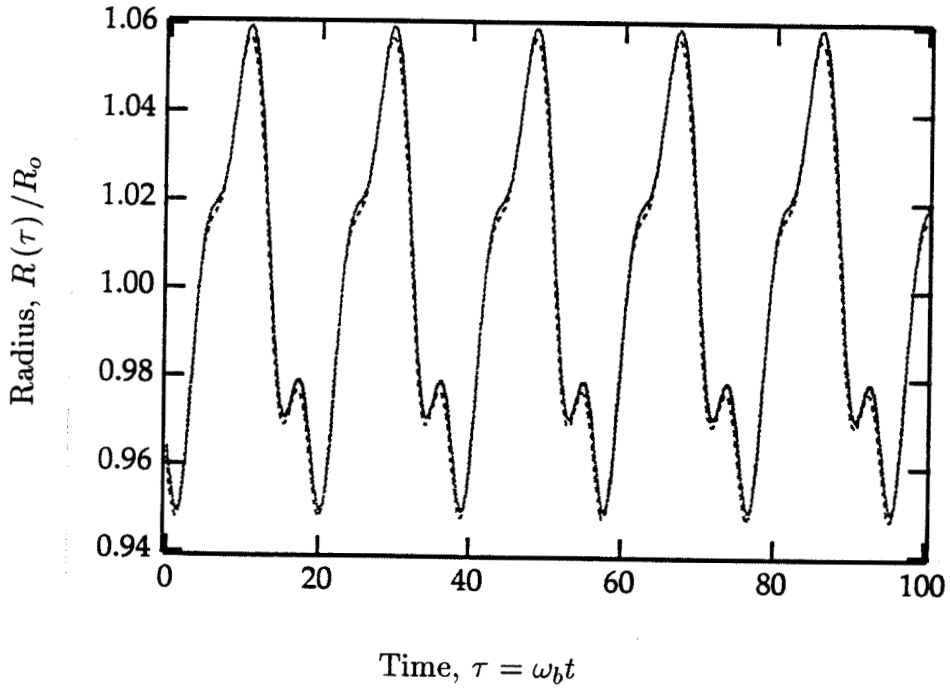


Figure 2.1: Radius $R(\tau)/R_o$ is plotted against the nondimensional time, $\tau = \omega_b t$ for a single bubble. The parameters : $P_n/\omega_b^2 R_o^2 = 0.04$, $\omega_b/\omega_p = 3.0$ and $\nu/\omega_b R_o^2$ and $S/\rho\omega_b^2 R_o^3$ are for the water tunnel conditions. (—) is the numerical solution and (- - -) is the approximate analytical solution

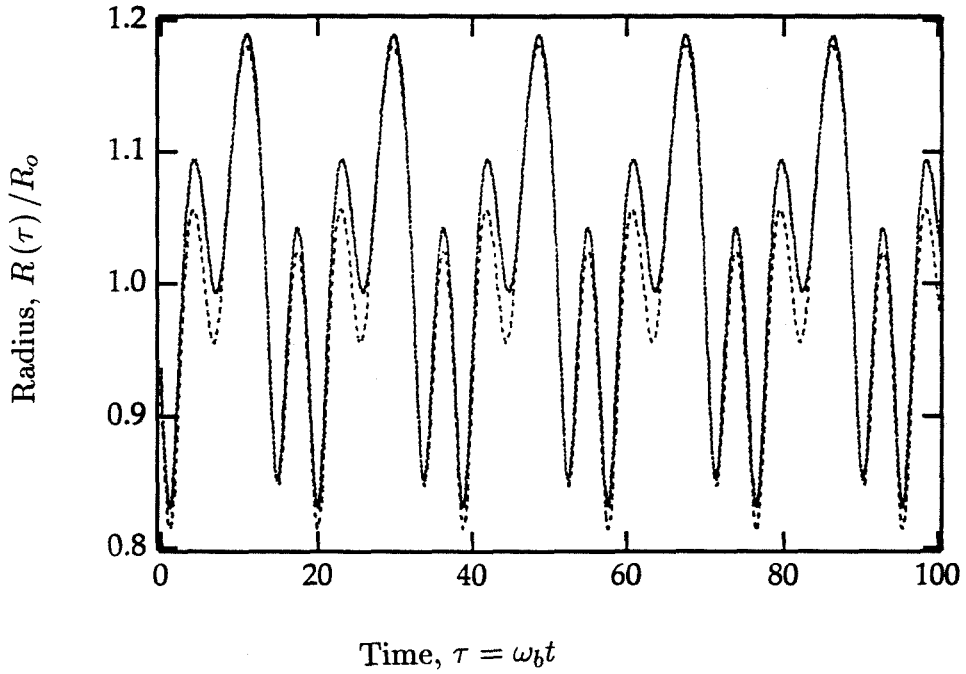


Figure 2.2: Radius $R(\tau)/R_o$ is plotted against the nondimensional time, $\tau = \omega_b t$ for a single bubble. The parameters : $P_n/\omega_b^2 R_o^2 = 0.08$, $\omega_b/\omega_p = 3.0$ and $\nu/\omega_b R_o^2$ and $S/\rho\omega_b^2 R_o^3$ are for the water tunnel conditions. (—) is the numerical solution and (- - -) is the approximate analytical solution

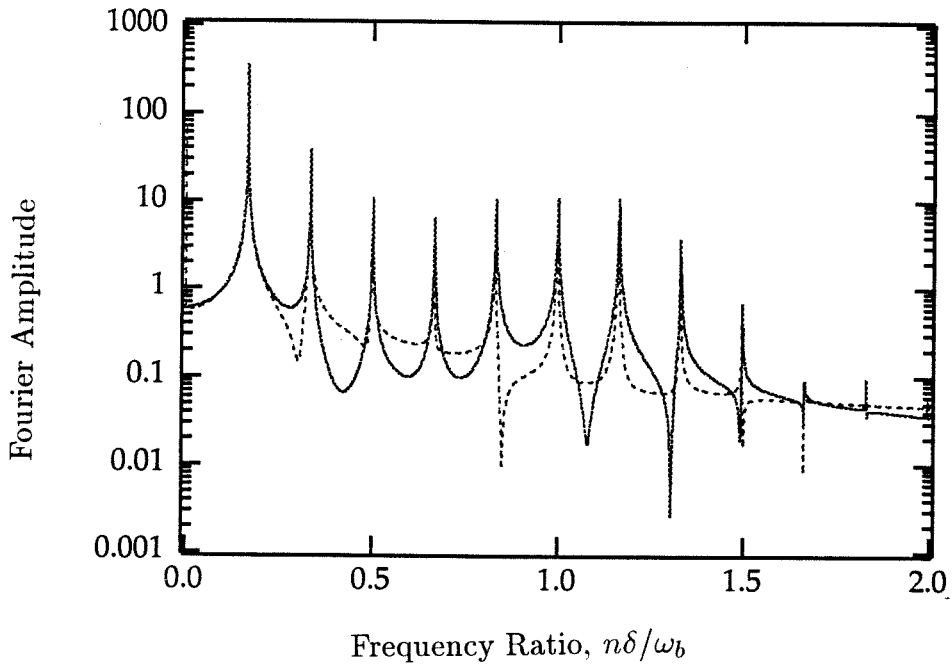


Figure 2.3: Comparison of the spectra of $[1 - R(\tau)/R_o]$ obtained for a single bubble from numerical integration of the Rayleigh-Plesset equation (—) and the present approximate (---) analysis. The parameters : $P_n/\omega_b^2 R_o^2 = 0.08$, $\omega_b/\omega_p = 6.0$ and $\nu/\omega_b R_o^2$ and $S/\rho\omega_b^2 R_o^3$ are for the water tunnel conditions.

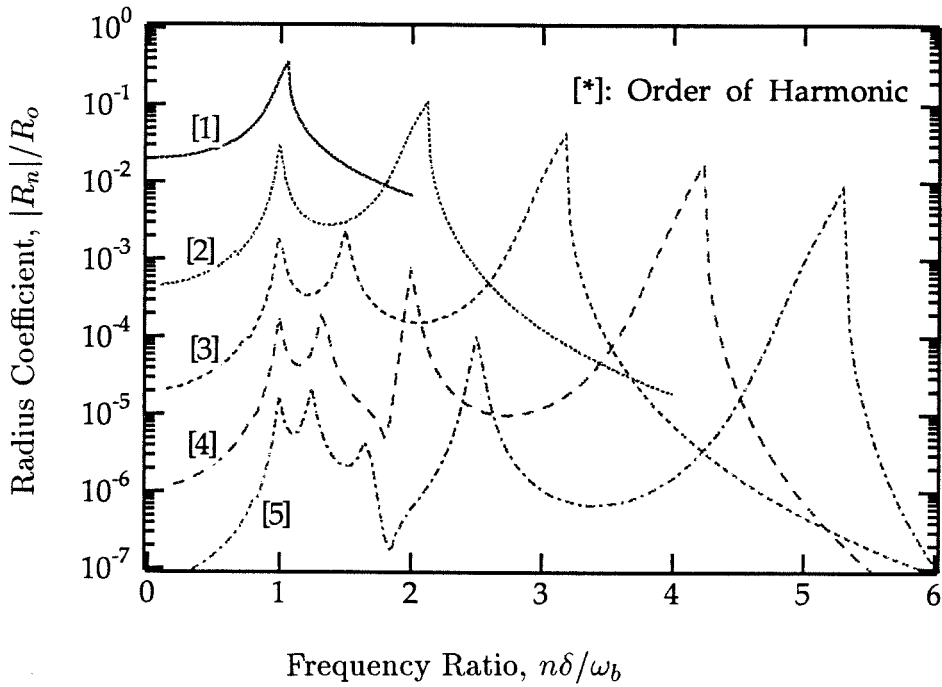


Figure 2.4: The frequency response of a single bubble; $|R_n|/R_o$ is plotted against the frequency ratio, $n\delta/\omega_b$, for the first five harmonics. The parameters: $P_n/\omega_b^2 R_o^2 = 0.02$ and $\nu/\omega_b R_o^2$ and $S/\rho\omega_b^2 R_o^3$ are for the water tunnel conditions.

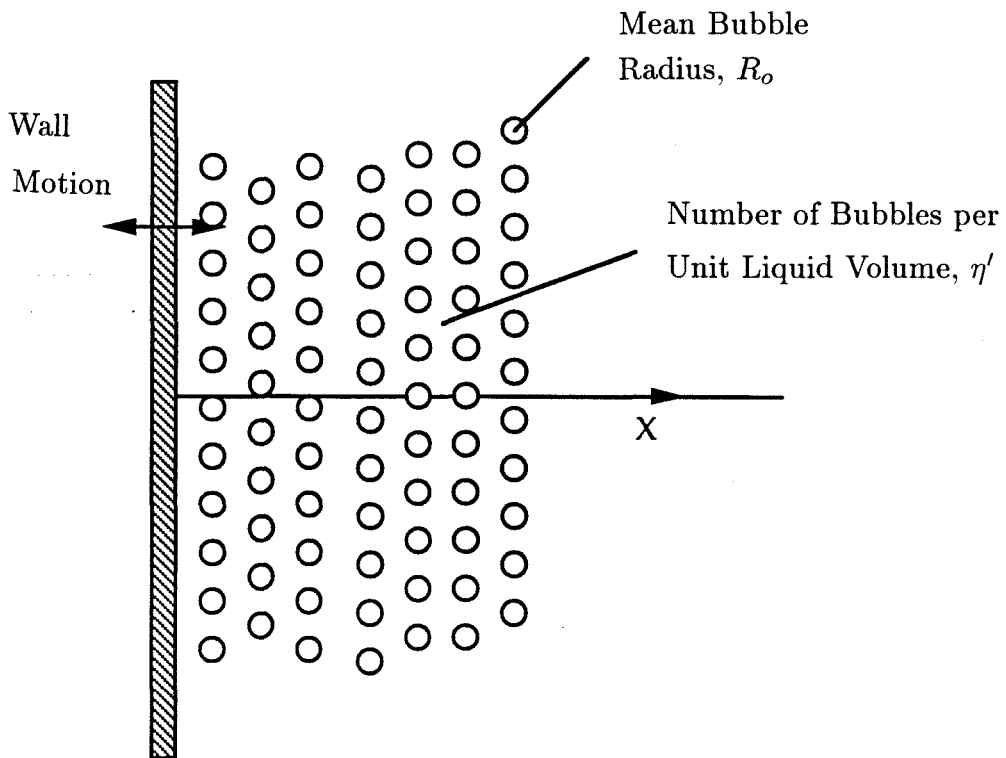


Figure 2.5: Schematic of the Oscillating Wall Problem.

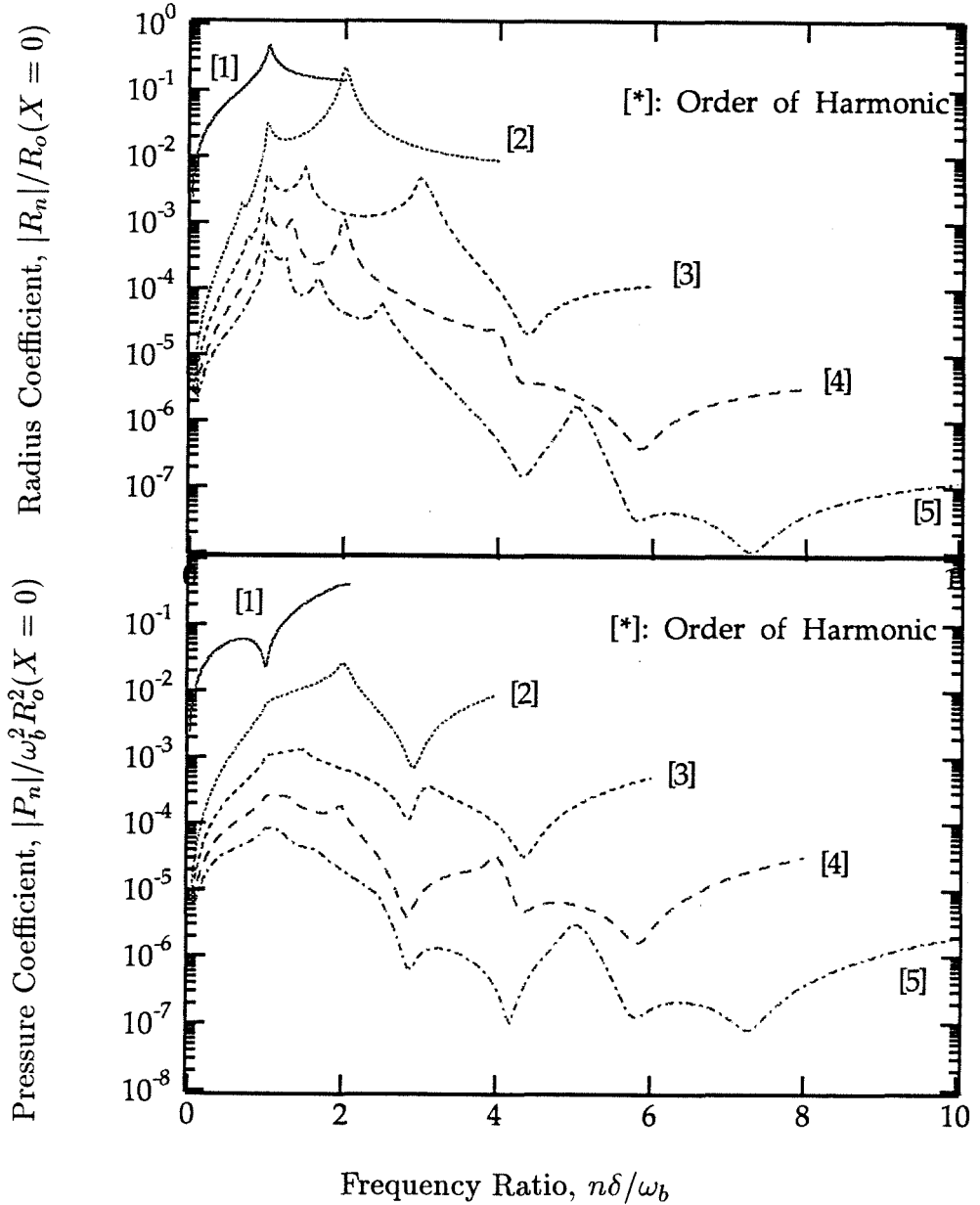


Figure 2.6: The frequency response of the bubbly cloud; $|R_n|/R_o(X=0)$ and $|P_n|/\omega_b^2 R_o^2(X=0)$ are plotted against the frequency ratio, $n\delta/\omega_b$, for the first five harmonics. The parameters: $X_n(0)/R_o = 0.03$, $\alpha_o = 0.02$ and $\nu/\omega_b R_o^2$ and $S/\rho\omega_b^2 R_o^3$ are for the water tunnel conditions.

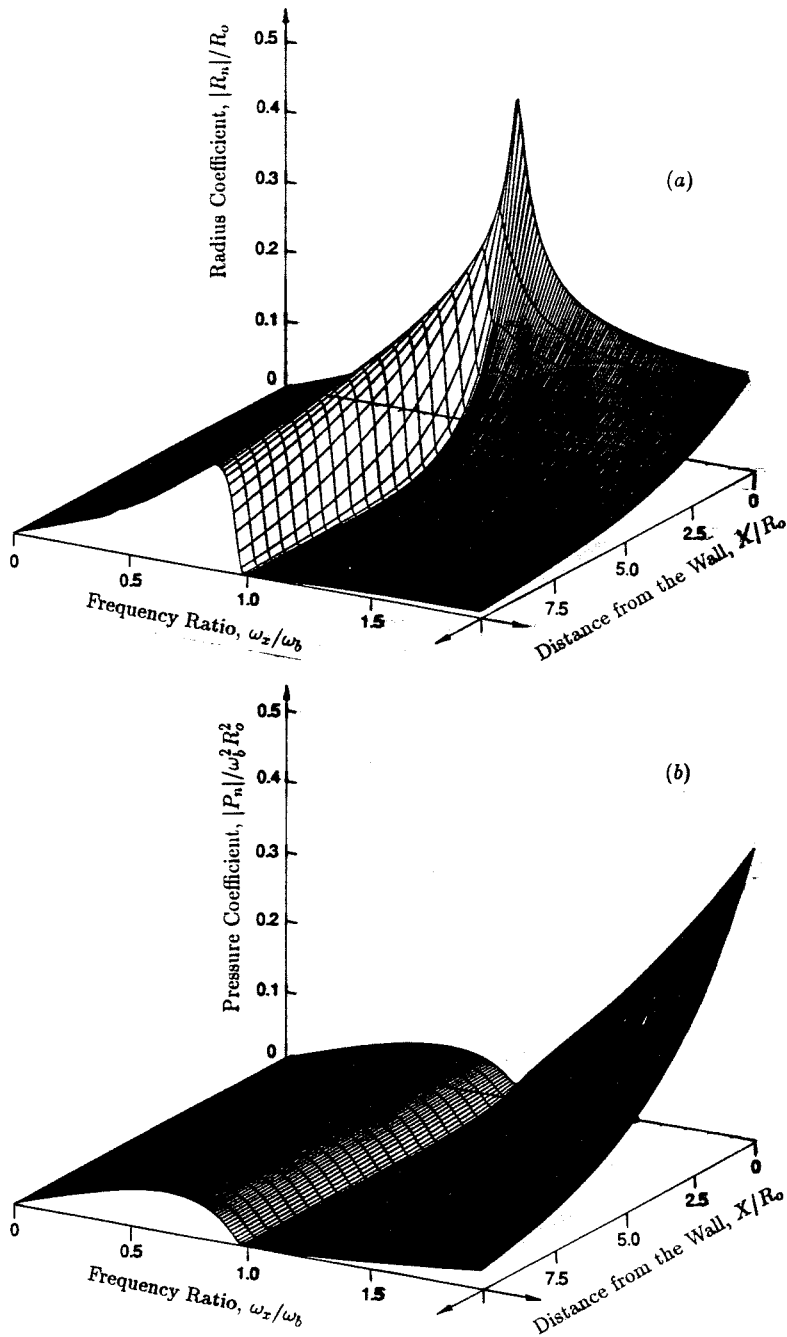


Figure 2.7: The frequency response of the bubbly cloud; (a) $|R_n|/R_o$ and (b) $|P_n|/\omega_b^2 R_o^2$ for the fundamental harmonic are plotted against the frequency ratio, ω_x/ω_b , and the distance from the oscillating wall, X/R_o , to illustrate the decay away from the wall. The parameters: $X_n(0)/R_o = 0.03$, $\alpha_o = 0.02$ and $\nu/\omega_b R_o^2$ and $S/\rho\omega_b^2 R_o^3$ for the water tunnel conditions.

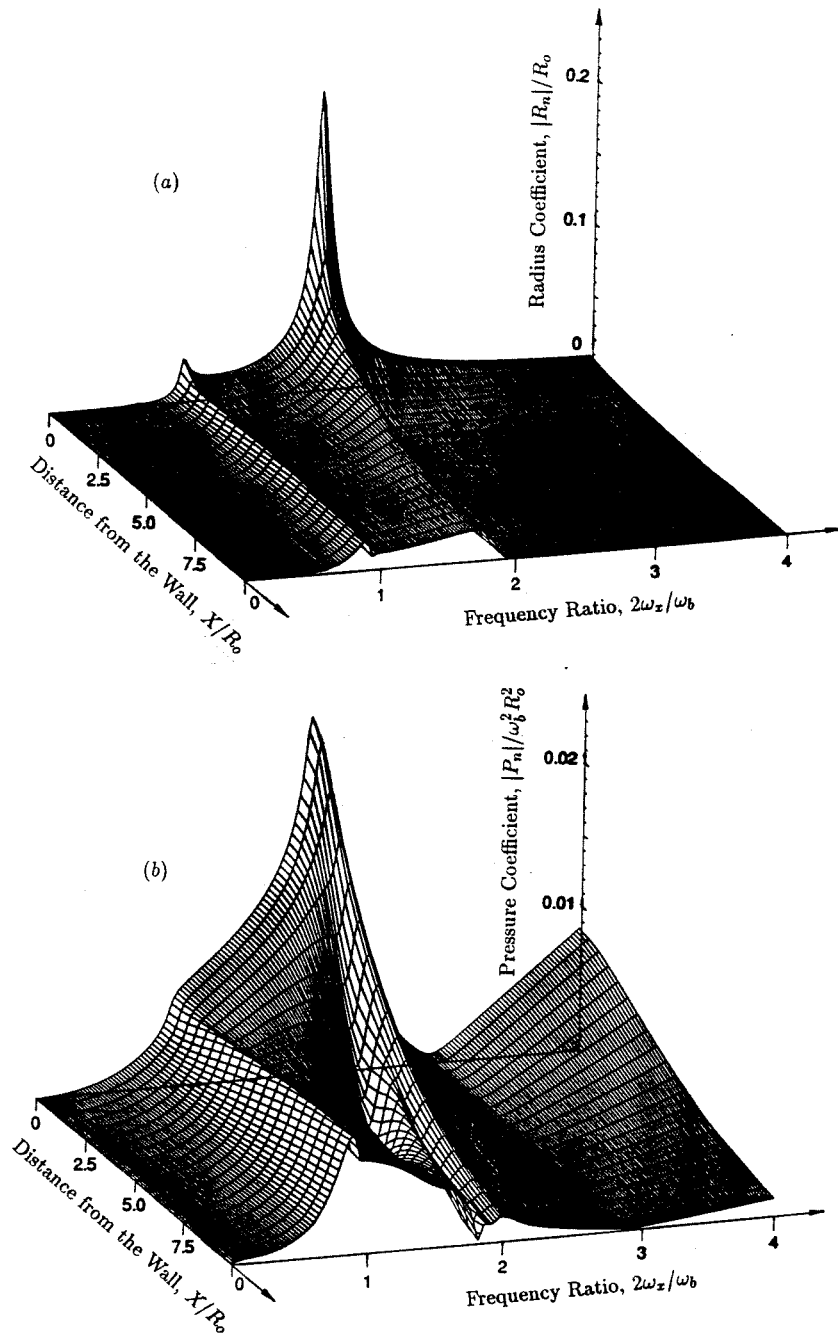


Figure 2.8: The frequency response of the bubbly cloud; (a) $|R_n|/R_o$ and (b) $|P_n|/\omega_b^2 R_o^2$ for the second harmonic are plotted against the frequency ratio, $2\omega_x/\omega_b$, and the distance from the oscillating wall, X/R_o , to illustrate the decay away from the wall. The parameters: $X_n(0)/R_o = 0.03$, $\alpha_o = 0.02$ and $\nu/\omega_b R_o^2$ and $S/\rho\omega_b^2 R_o^3$ are for the water tunnel conditions.

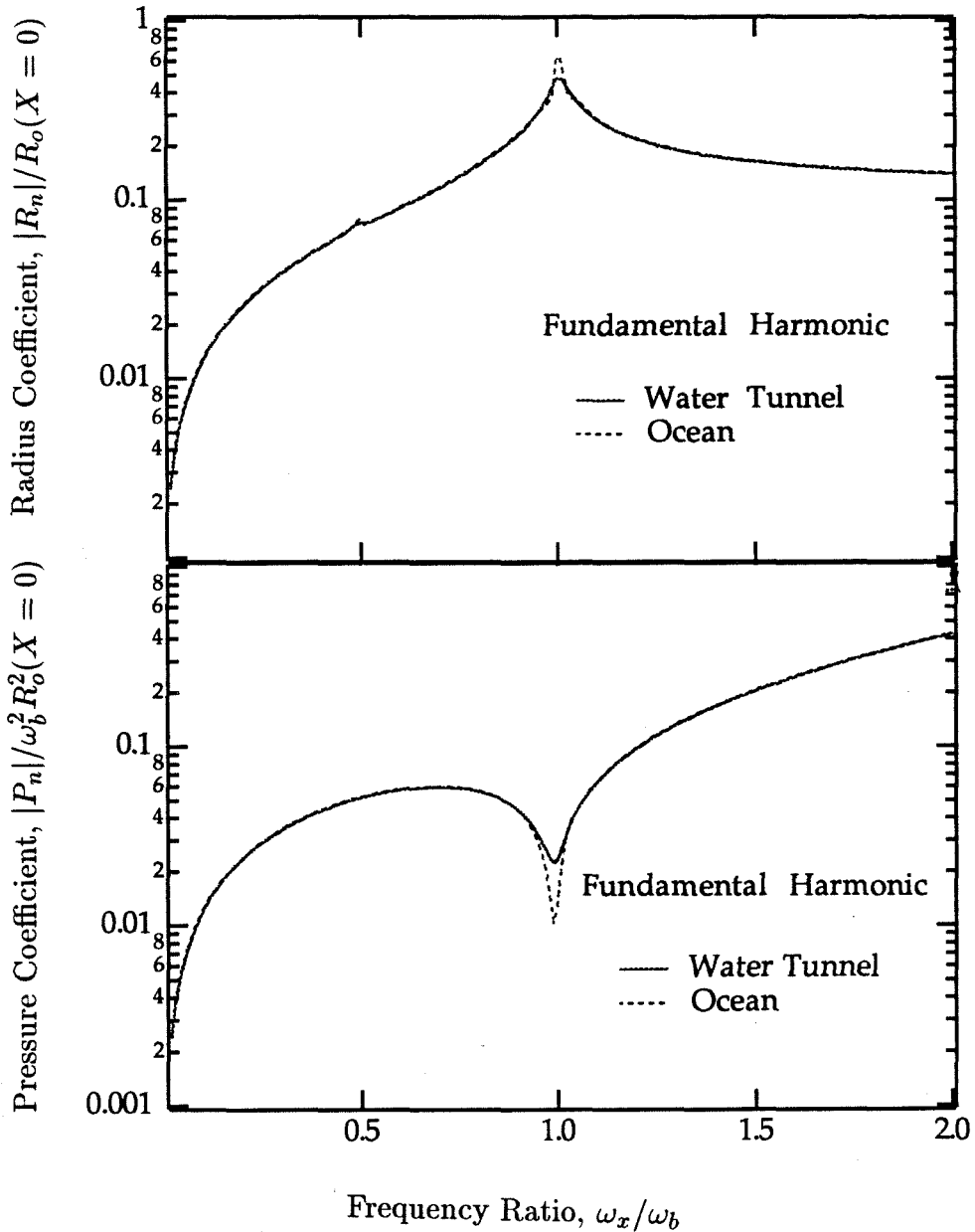


Figure 2.9: The effect of variation in $\nu/\omega_b R_o^2$ and $S/\rho\omega_b^2 R_o^3$ on the fundamental harmonic; $|R_n|/R_o(X=0)$ and $|P_n|/\omega_b^2 R_o^2(X=0)$ for the fundamental harmonic are plotted against the frequency ratio, ω_x/ω_b . The parameters: $X_n(0)/R_o = 0.03$, $\alpha_o = 0.02$ and $\nu/\omega_b R_o^2$ and $S/\rho\omega_b^2 R_o^3$ are for the water tunnel and the ocean conditions.

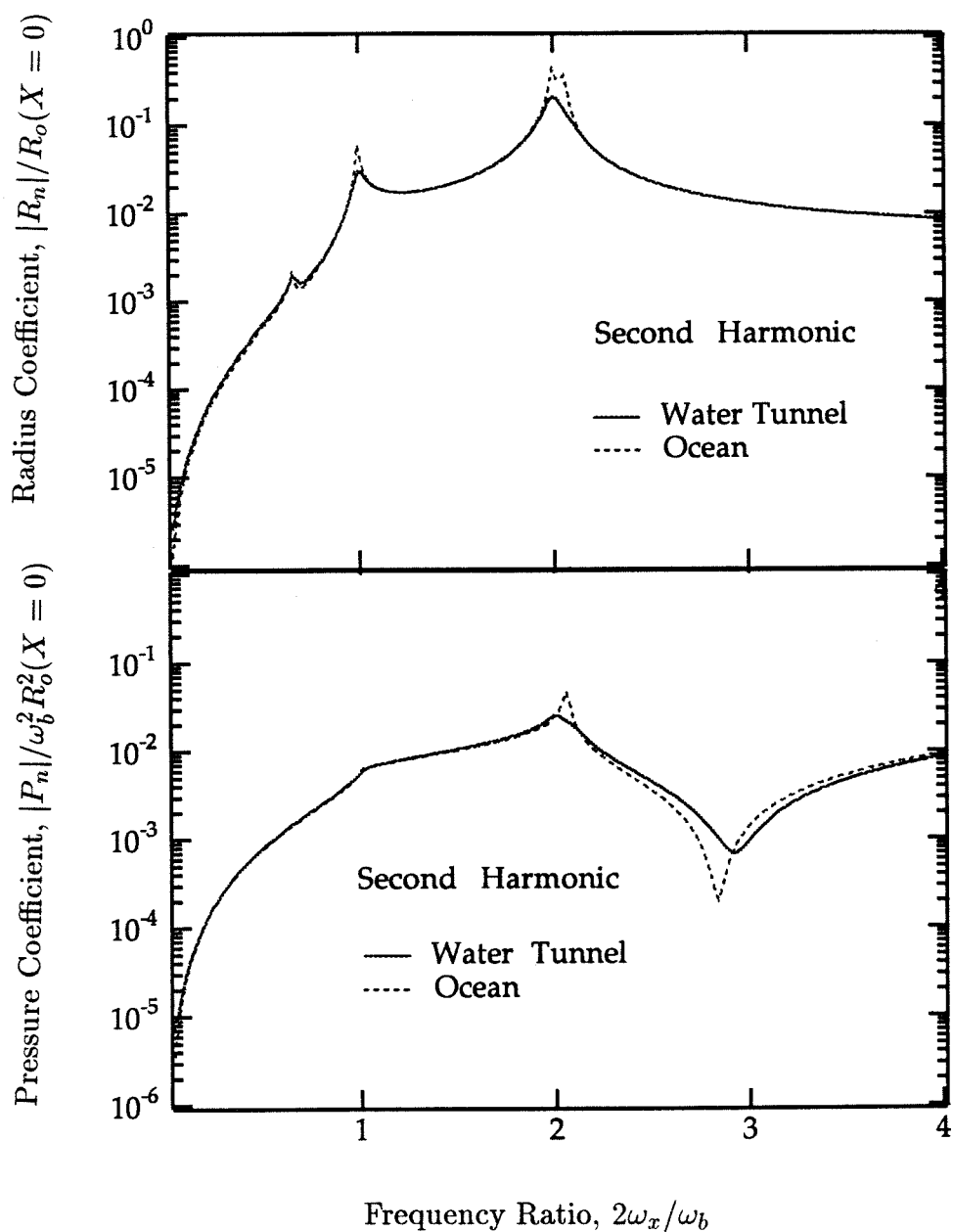


Figure 2.10: The effect of variation in $\nu/\omega_b R_o^2$ and $S/\rho\omega_b^2 R_o^3$ on the second harmonic; $|R_n|/R_o(X=0)$ and $|P_n|/\omega_b^2 R_o^2(X=0)$ for the second harmonic are plotted against the frequency ratio, $2\omega_x/\omega_b$. The parameters: $X_n(0)/R_o = 0.03$, $\alpha_o = 0.02$ and $\nu/\omega_b R_o^2$ and $S/\rho\omega_b^2 R_o^3$ are for the water tunnel and the ocean conditions.

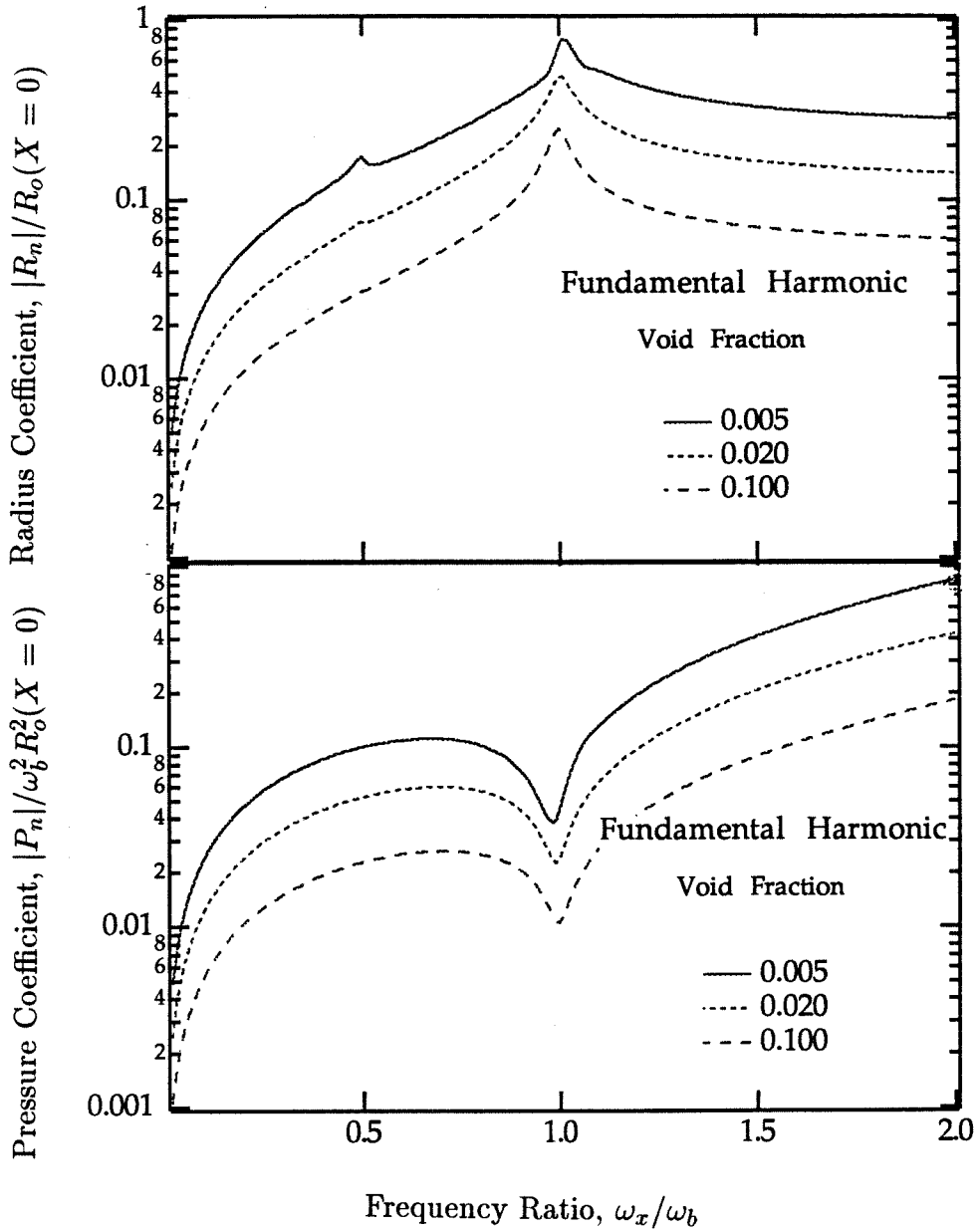


Figure 2.11: The effect of change in the void fraction, α_o , on the fundamental harmonic; $|R_n|/R_o(X=0)$ and $|P_n|/\omega_b^2 R_o^2(X=0)$ for the fundamental harmonic are plotted against the frequency ratio, ω_x/ω_b . The parameters: $X_n(0)/R_o = 0.03$ and $\nu/\omega_b R_o^2$ and $S/\rho\omega_b^2 R_o^3$ are for the water tunnel conditions. Values of the void fraction, α_o , of 0.005, 0.020 and 0.100 are used.

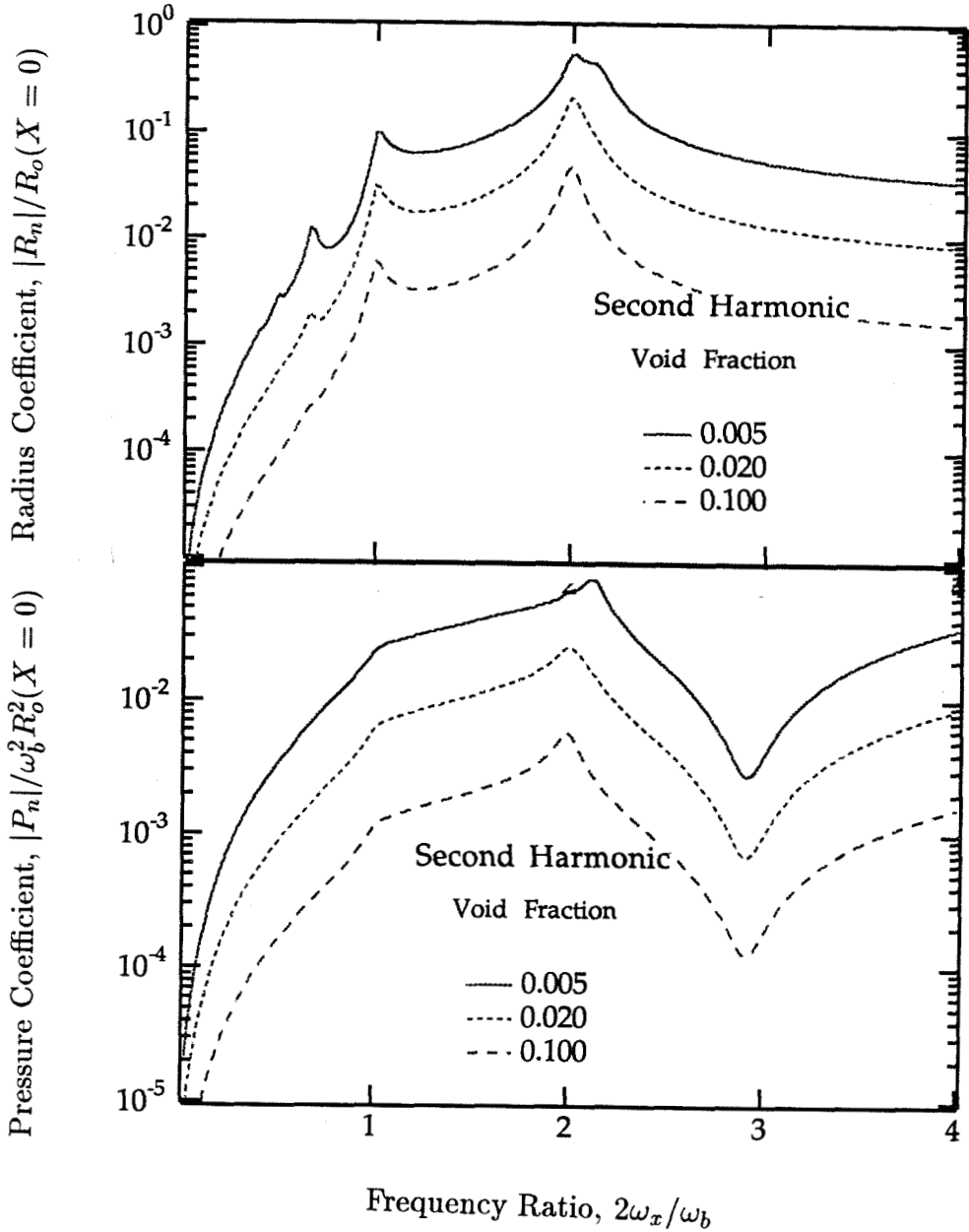


Figure 2.12: The effect of change in the void fraction, α_o , on the second harmonic; $|R_n|/R_o(X=0)$ and $|P_n|/\omega_b^2 R_o^2(X=0)$ for the second harmonic are plotted against the frequency ratio, $2\omega_x/\omega_b$. The parameters: $X_n(0)/R_o = 0.03$ and $\nu/\omega_b R_o^2$ and $S/\rho\omega_b^2 R_o^3$ are for the water tunnel conditions. Values of the void fraction, α_o , of 0.005, 0.020 and 0.100 are used.

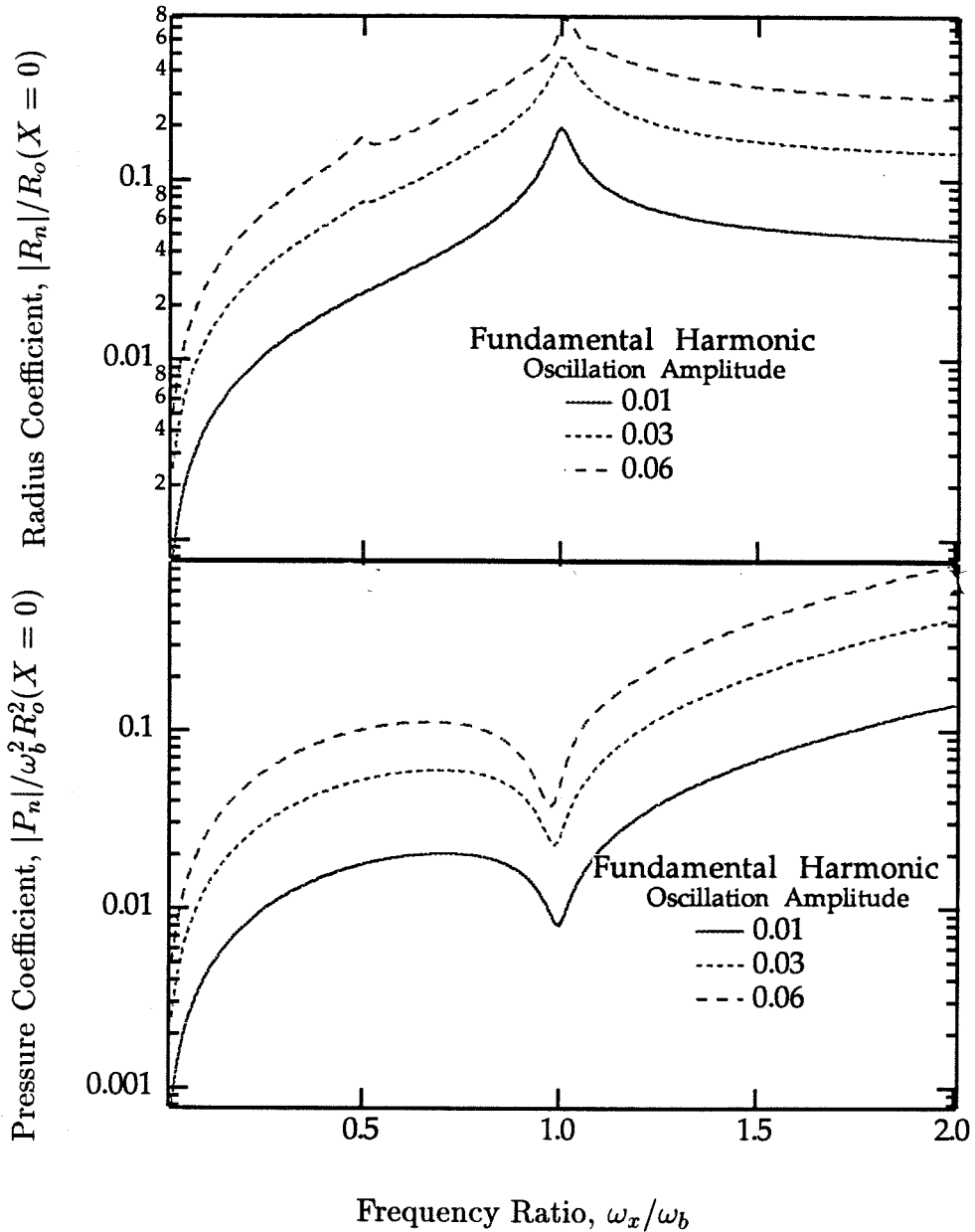


Figure 2.13: The effect of change in the amplitude of wall oscillation, $X_n(0)/R_o$, on the fundamental harmonic; $|R_n|/R_o(X=0)$ and $|P_n|/\omega_b^2 R_o^2(X=0)$ for the fundamental harmonic are plotted against the frequency ratio, ω_x/ω_b . The parameters: $\alpha_o=0.02$ and $\nu/\omega_b R_o^2$ and $S/\rho\omega_b^2 R_o^3$ are for the water tunnel conditions. $X_n(0)/R_o$ values of 0.01, 0.03 and 0.06 are used.

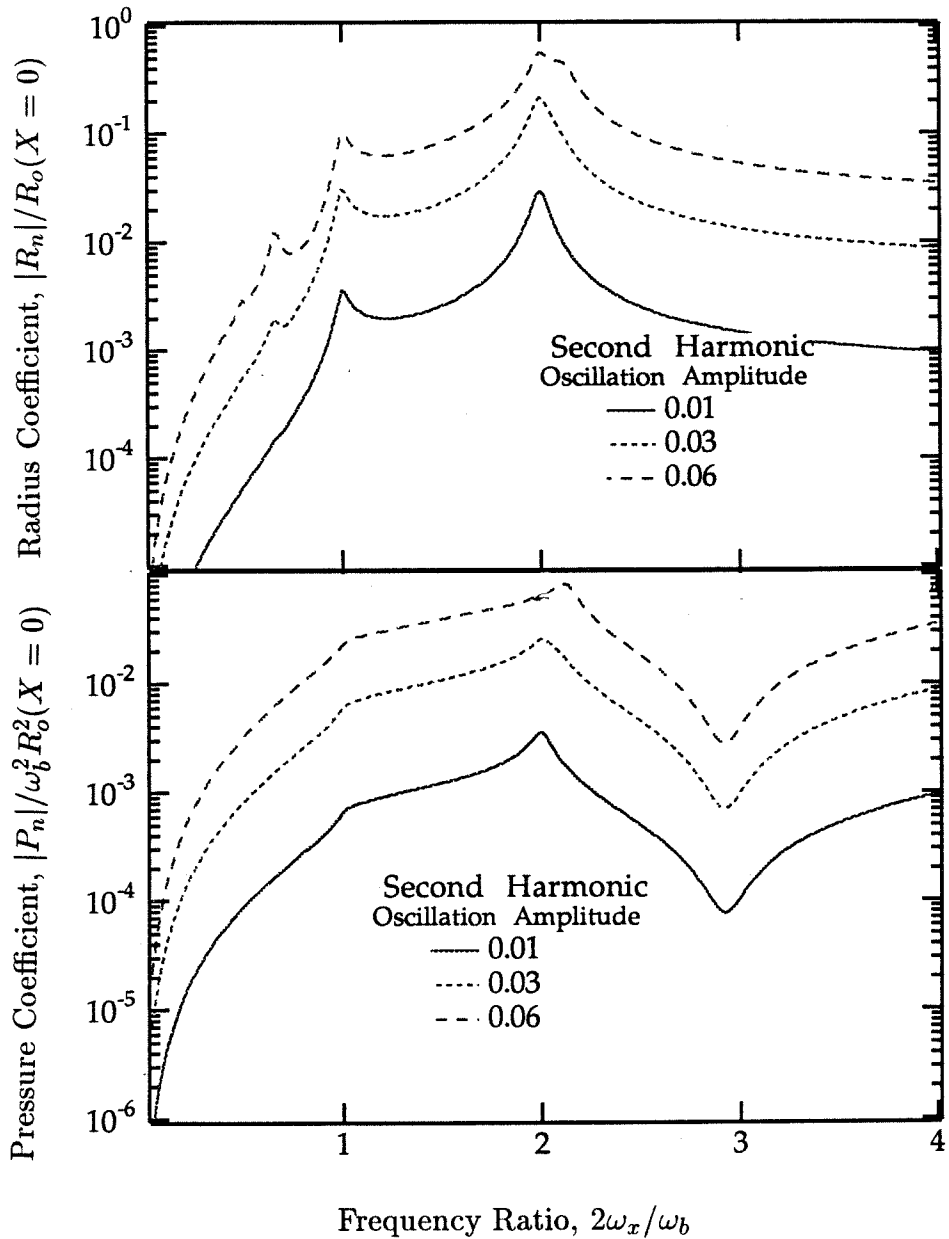


Figure 2.14: The effect of change in the amplitude of wall oscillation, $X_n(0)/R_o$, on the second harmonic; $|R_n|/R_o(X=0)$ and $|P_n|/\omega_b^2 R_o^2(X=0)$ for the second harmonic are plotted against the frequency ratio, $2\omega_x/\omega_b$. The parameters: $\alpha_o=0.02$ and $\nu/\omega_b R_o^2$ and $S/\rho\omega_b^2 R_o^3$ are for the water tunnel conditions. $X_n(0)/R_o$ values of 0.01, 0.03 and 0.06 are used.

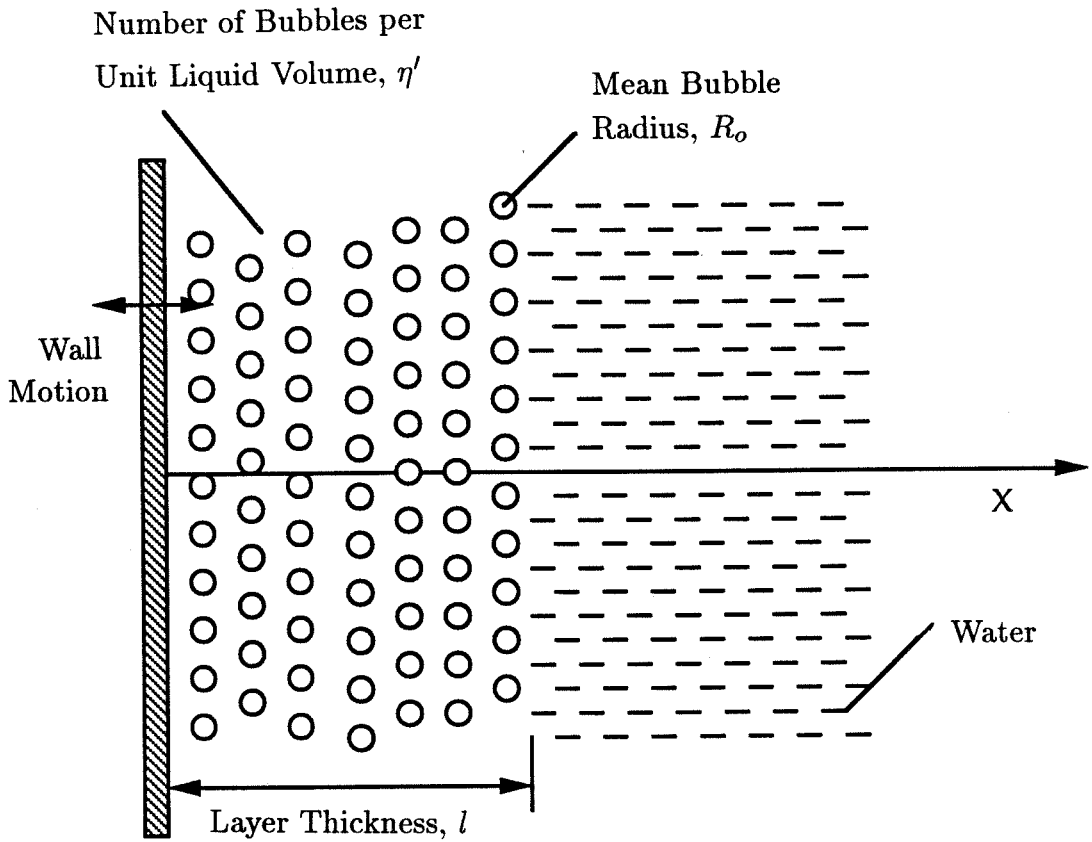


Figure 2.15: Schematic of the Oscillating Wall Problem With a Layer of Finite Thickness.

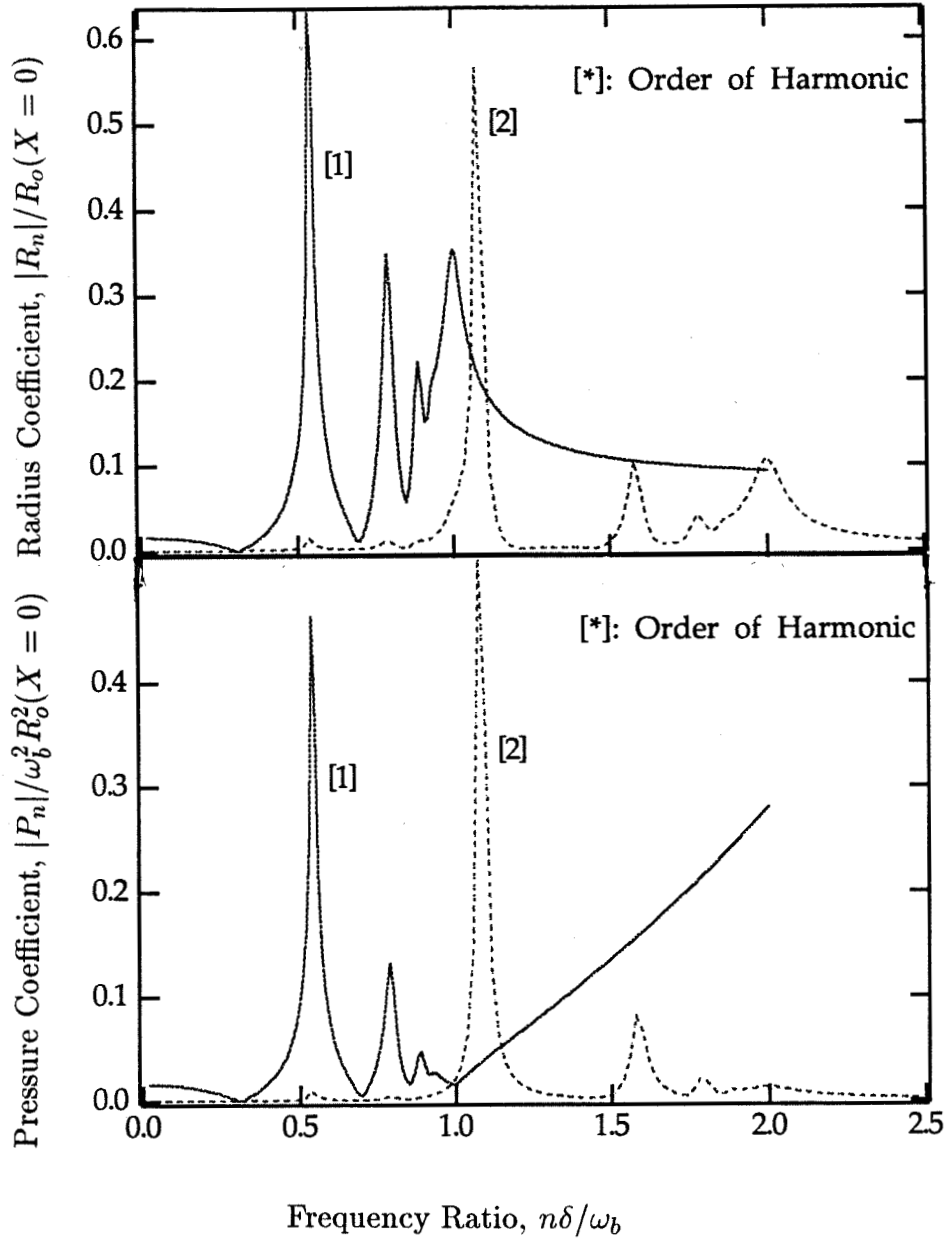


Figure 2.16: The frequency response of a bubbly layer of finite thickness; $|R_n|/R_o(X=0)$ and $|P_n|/\omega_b^2 R_o^2(X=0)$ are plotted against the frequency ratio, $n\delta/\omega_b$, for the first two harmonics. The parameters: $X_n(0)/R_o = 0.02$, $\alpha_o = 0.02$, $l/R_o = 20$ and $\nu/\omega_b R_o^2$ and $S/\rho\omega_b^2 R_o^3$ are for the water tunnel conditions.

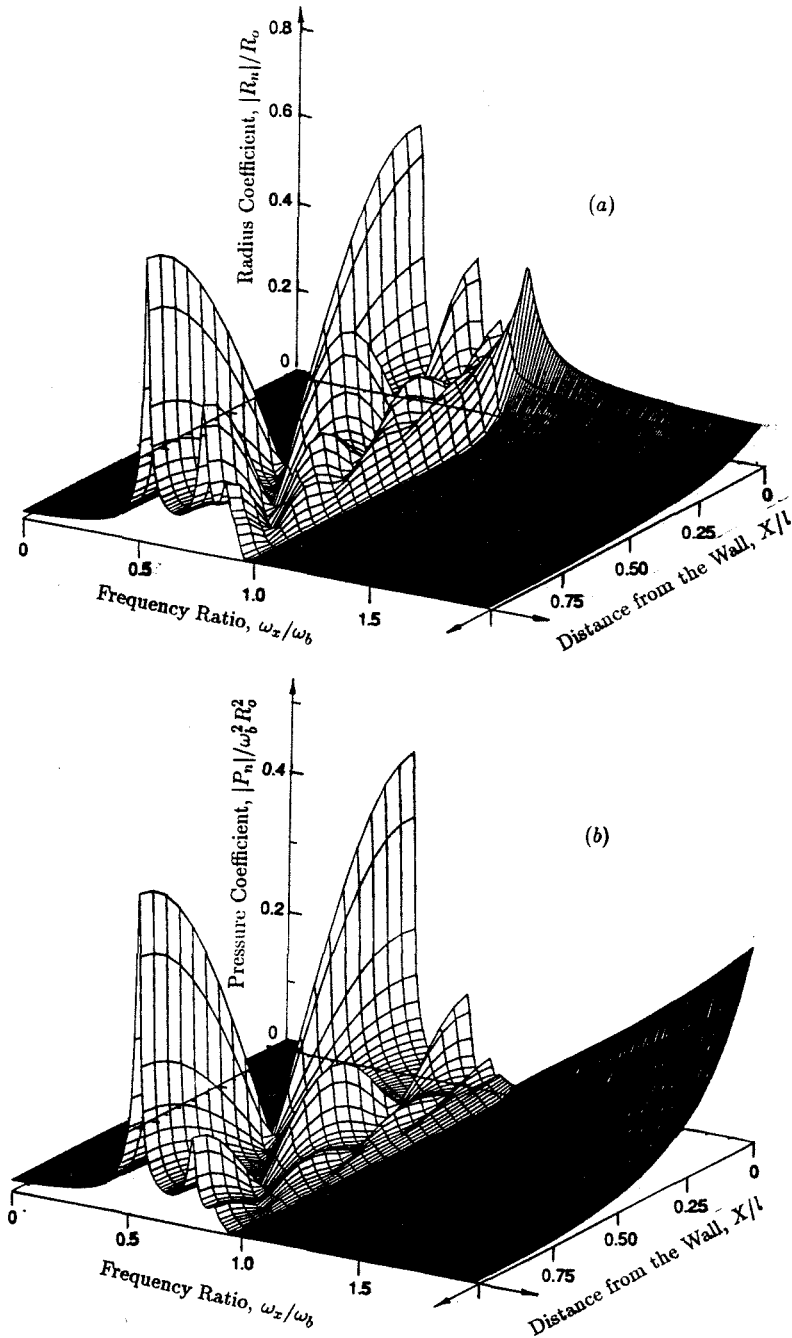


Figure 2.17: The frequency response of a bubbly layer of finite thickness; (a) $|R_n|/R_o$ and (b) $|P_n|/\omega_b^2 R_o^2$ for the fundamental harmonic are plotted against the frequency ratio, ω_x/ω_b , and the distance from the oscillating wall, X/l , for the first harmonic. The parameters: $X_n(0)/R_o = 0.02$, $\alpha_o = 0.02$, $l/R_o = 20$ and $\nu/\omega_b R_o^2$ and $S/\rho\omega_b^2 R_o^3$ are for the water tunnel conditions.

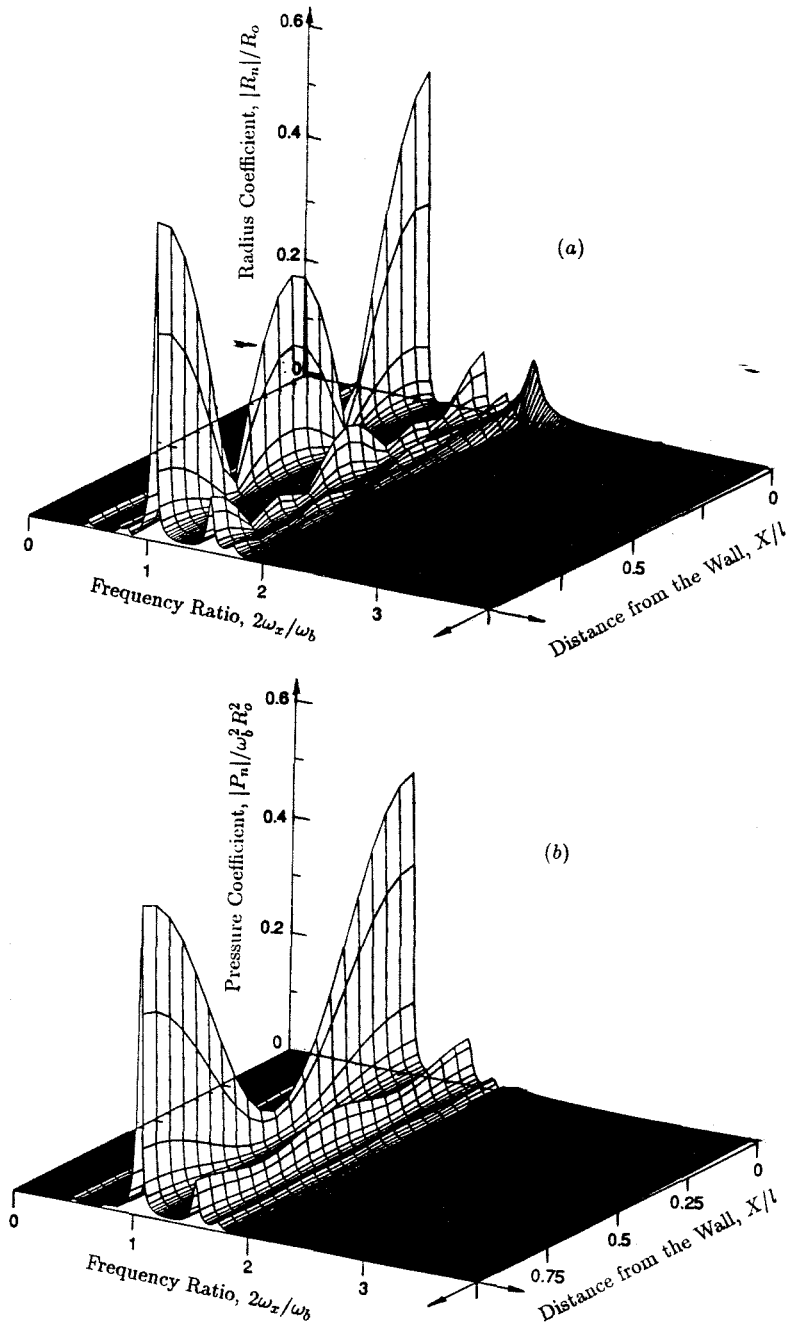


Figure 2.18: The frequency response of a bubbly layer of finite thickness; (a) $|R_n|/R_o$ and (b) $|P_n|/\omega_b^2 R_o^2$ for the second harmonic are plotted against the frequency ratio, $2\omega_x/\omega_b$, and the distance from the oscillating wall, X/l , for the second harmonic. The parameters: $X_n(0)/R_o = 0.02$, $\alpha_o = 0.02$, $l/R_o = 20$ and $\nu/\omega_b R_o^2$ and $S/\rho\omega_b^2 R_o^3$ are for the water tunnel conditions.

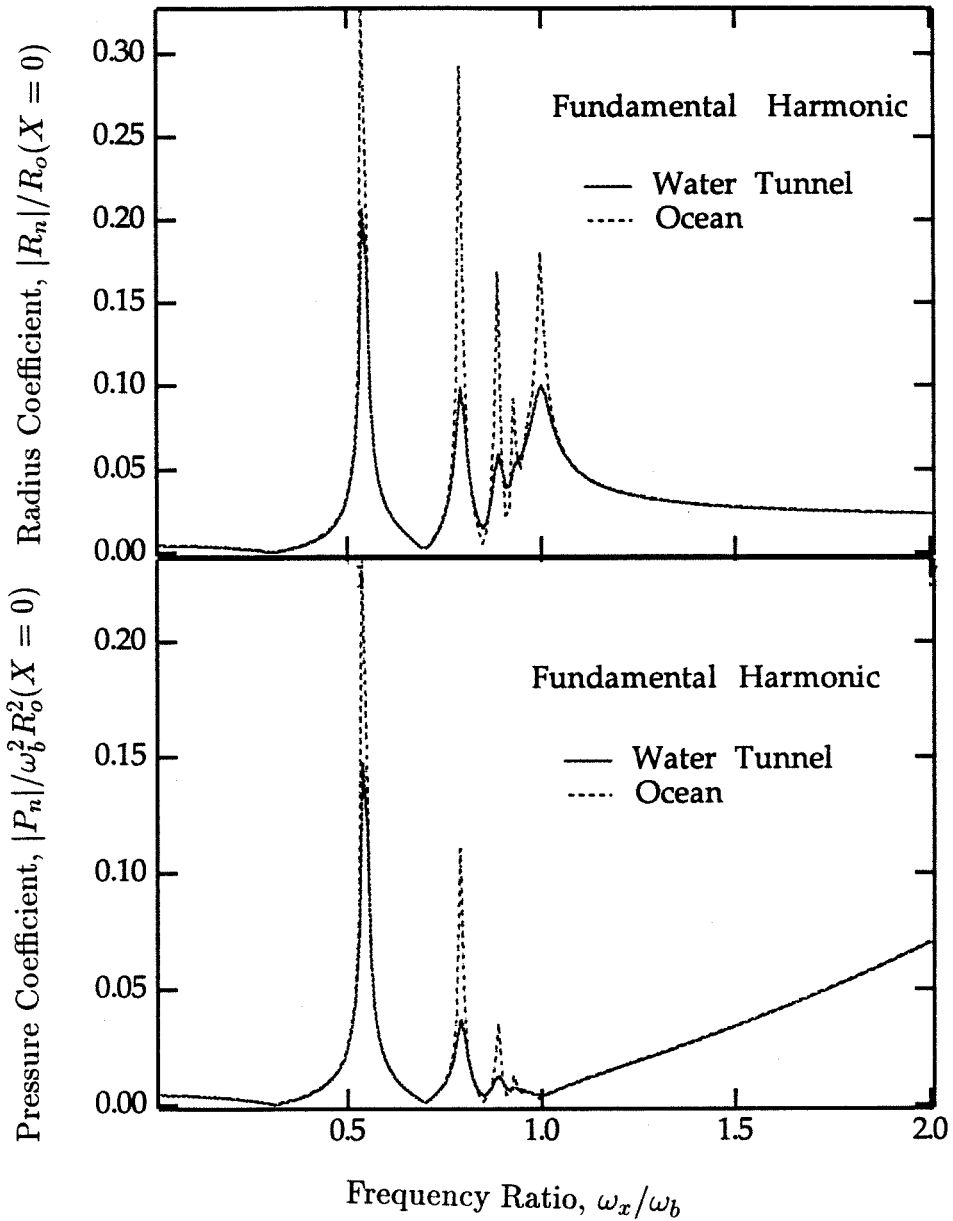


Figure 2.19: The effect of variation in $\nu/\omega_b R_o^2$ and $S/\rho\omega_b^2 R_o^3$ on the fundamental harmonic; $|R_n|/R_o(X=0)$ and $|P_n|/\omega_b^2 R_o^2(X=0)$ for the fundamental harmonic are plotted against the frequency ratio, ω_x/ω_b . The parameters: $X_n(0)/R_o = 0.005$, $\alpha_o = 0.02$, $l/R_o = 20$ and $\nu/\omega_b R_o^2$ and $S/\rho\omega_b^2 R_o^3$ are for the water tunnel and the ocean conditions.

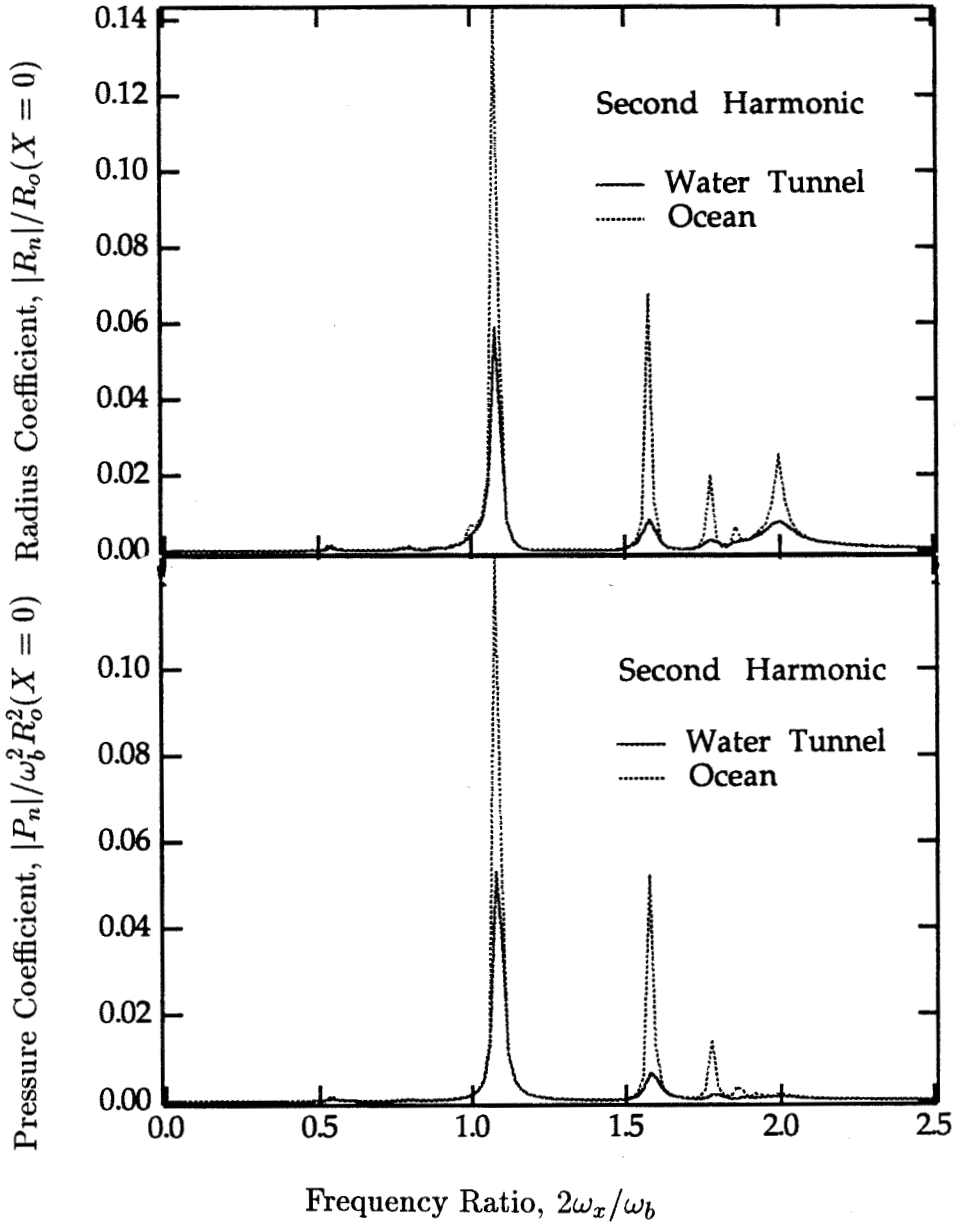


Figure 2.20: The effect of variation in $\nu/\omega_b R_o^2$ and $S/\rho\omega_b^2 R_o^3$ on the second harmonic; $|R_n|/R_o(X=0)$ and $|P_n|/\omega_b^2 R_o^2(X=0)$ for the second harmonic are plotted against the frequency ratio, $2\omega_x/\omega_b$. The parameters: $X_n(0)/R_o = 0.005$, $\alpha_o = 0.02$, $l/R_o = 20$ and $\nu/\omega_b R_o^2$ and $S/\rho\omega_b^2 R_o^3$ are for the water tunnel and the ocean conditions.

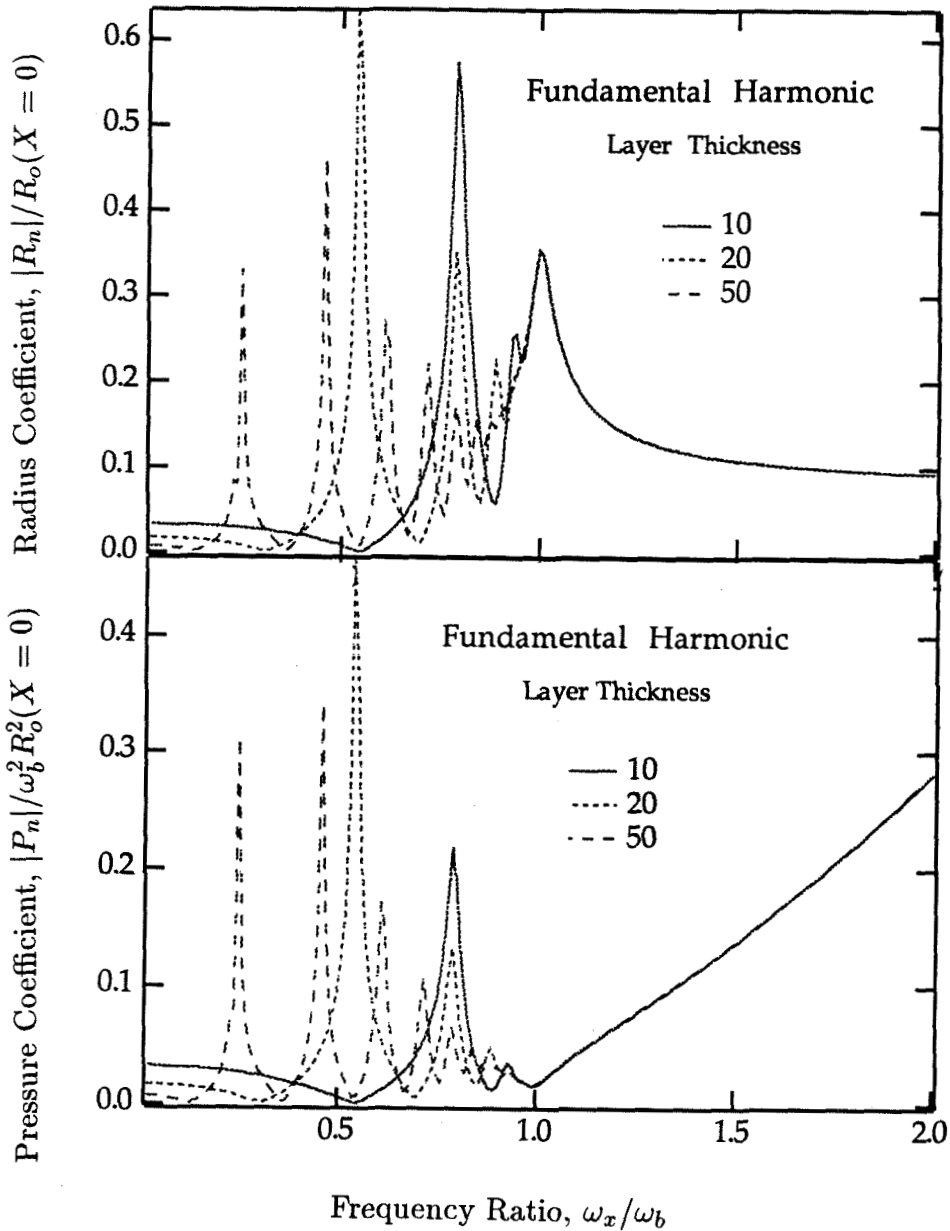


Figure 2.21: The effect of change in the thickness of the bubble layer, l/R_o , on the fundamental harmonic; $|R_n|/R_o(X=0)$ and $|P_n|/\omega_b^2 R_o^2(X=0)$ for the fundamental harmonic are plotted against the frequency ratio, ω_x/ω_b . The parameters: $X_n(0)/R_o = 0.02$, $\alpha_o = 0.02$ and $\nu/\omega_b R_o^2$ and $S/\rho\omega_b^2 R_o^3$ are for the water tunnel conditions. Values of the thickness of the bubble layer, l/R_o , of 10, 20 and 50 are used.

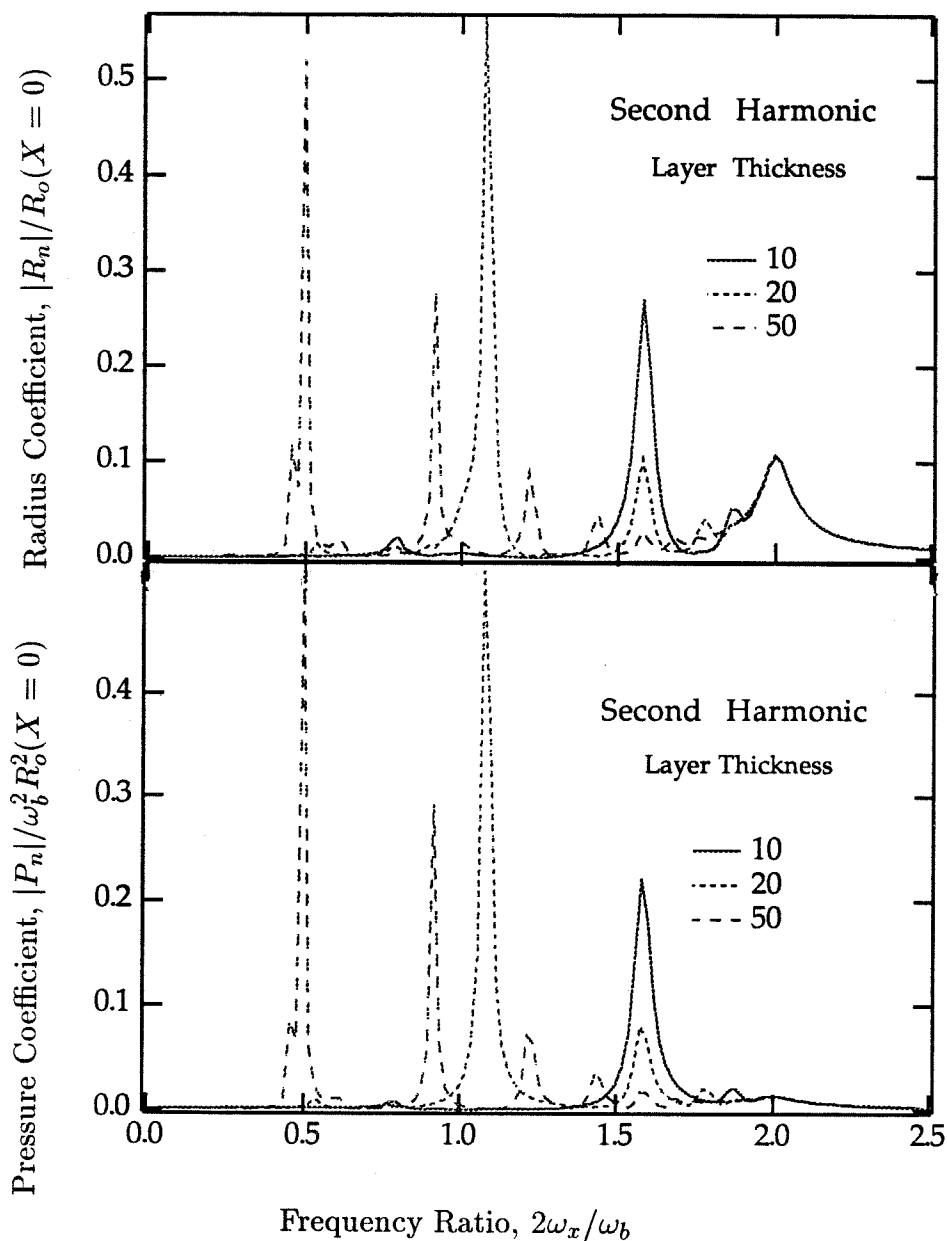


Figure 2.22: The effect of change in thickness of the bubble layer, l/R_o , on the second harmonic; $|R_n|/R_o(X=0)$ and $|P_n|/\omega_b^2 R_o^2(X=0)$ for the second harmonic are plotted against the frequency ratio, $2\omega_x/\omega_b$. The parameters: $X_n(0)/R_o = 0.02$, $\alpha_o = 0.02$ and $\nu/\omega_b R_o^2$ and $S/\rho\omega_b^2 R_o^3$ are for the water tunnel conditions. Values of the thickness of the bubble layer, l/R_o , of 10, 20 and 50 are used.

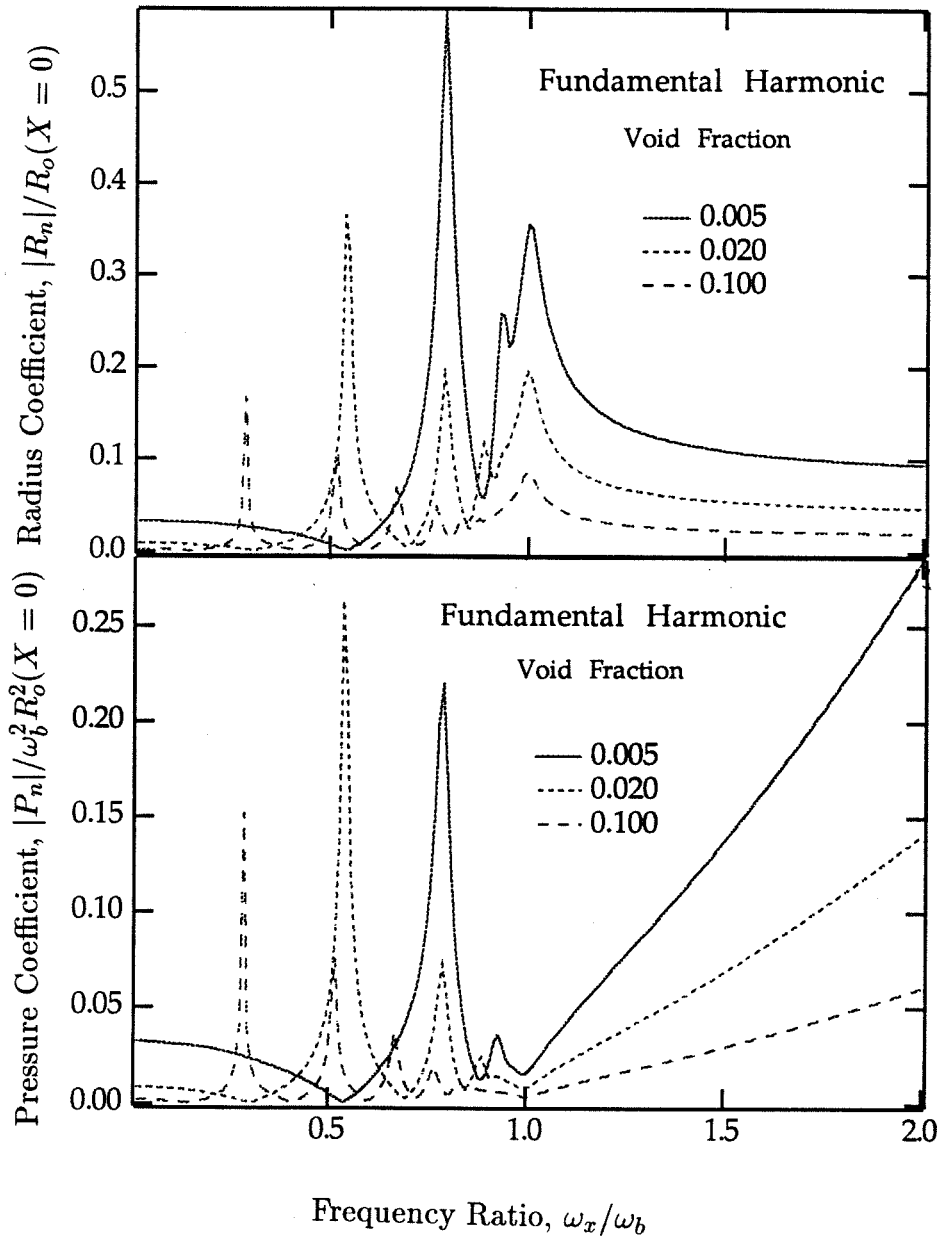


Figure 2.23: The effect of change in the void fraction, α_o , on the fundamental harmonic; $|R_n|/R_o(X=0)$ and $|P_n|/\omega_b^2 R_o^2(X=0)$ for the fundamental harmonic are plotted against the frequency ratio, ω_x/ω_b . The parameters: $X_n(0)/R_o = 0.02$, $l/R_o = 20$ and $\nu/\omega_b R_o^2$ and $S/\rho\omega_b^2 R_o^3$ are for the water tunnel conditions. Values of the void fraction, α_o , of 0.005, 0.020 and 0.100 are used.

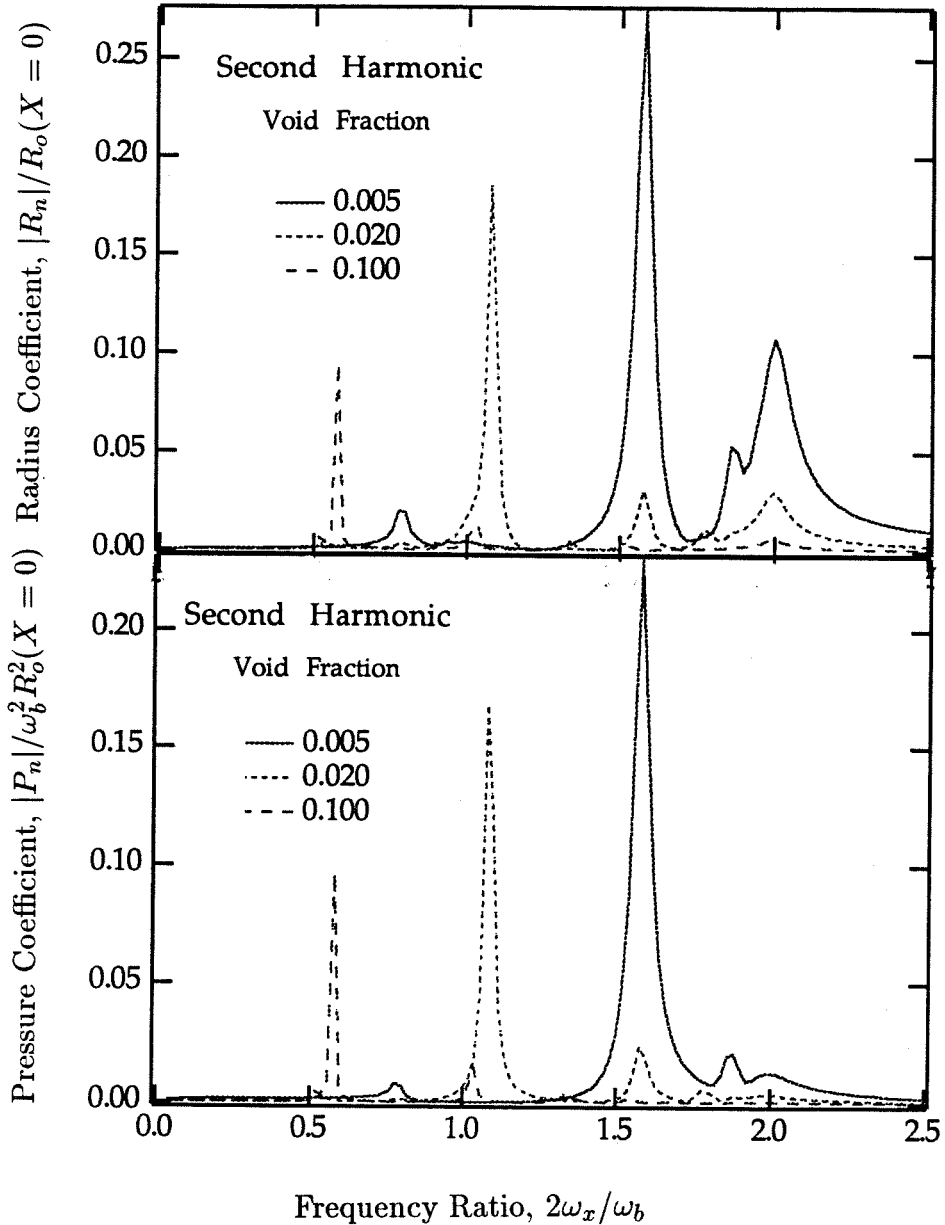


Figure 2.24: The effect of change in the void fraction, α_o , on the second harmonic; $|R_n|/R_o(X = 0)$ and $|P_n|/\omega_b^2 R_o^2(X = 0)$ for the second harmonic are plotted against the frequency ratio, $2\omega_x/\omega_b$. The parameters: $X_n(0)/R_o = 0.02$, $l/R_o = 20$ and $\nu/\omega_b R_o^2$ and $S/\rho\omega_b^2 R_o^3$ are for the water tunnel conditions. Values of the void fraction, α_o , of 0.005, 0.020 and 0.100 are used.

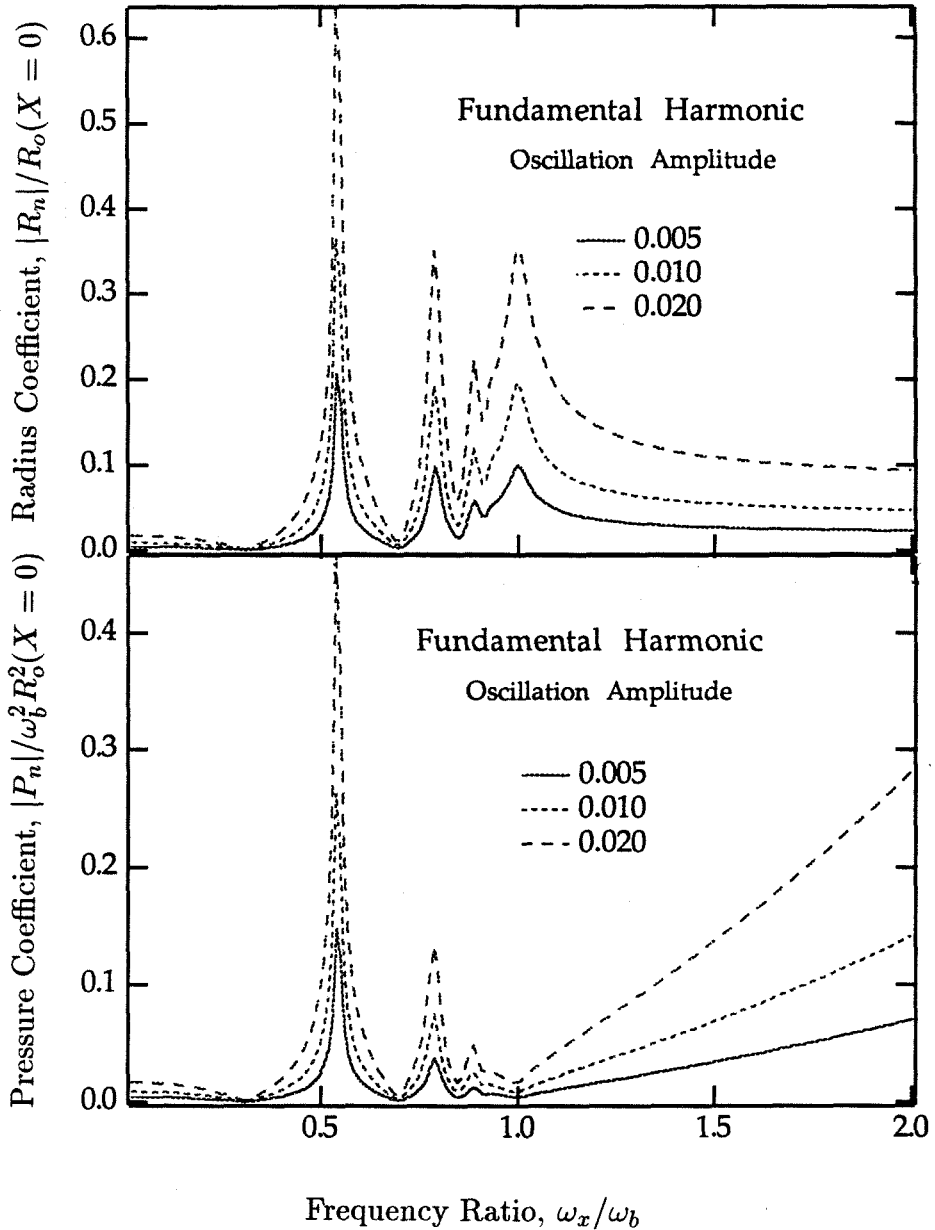


Figure 2.25: The effect of change in the amplitude of wall oscillation, $X_n(0)/R_o$, on the fundamental harmonic; $|R_n|/R_o(X=0)$ and $|P_n|/\omega_b^2 R_o^2(X=0)$ for the fundamental harmonic are plotted against the frequency ratio, ω_x/ω_b . The parameters: $\alpha_o = 0.02$, $l/R_o = 20$ and $\nu/\omega_b R_o^2$ and $S/\rho\omega_b^2 R_o^3$ are for the water tunnel conditions. Values of the amplitude of wall oscillation, $X_n(0)/R_o$, of 0.005, 0.010 and 0.020 are used.

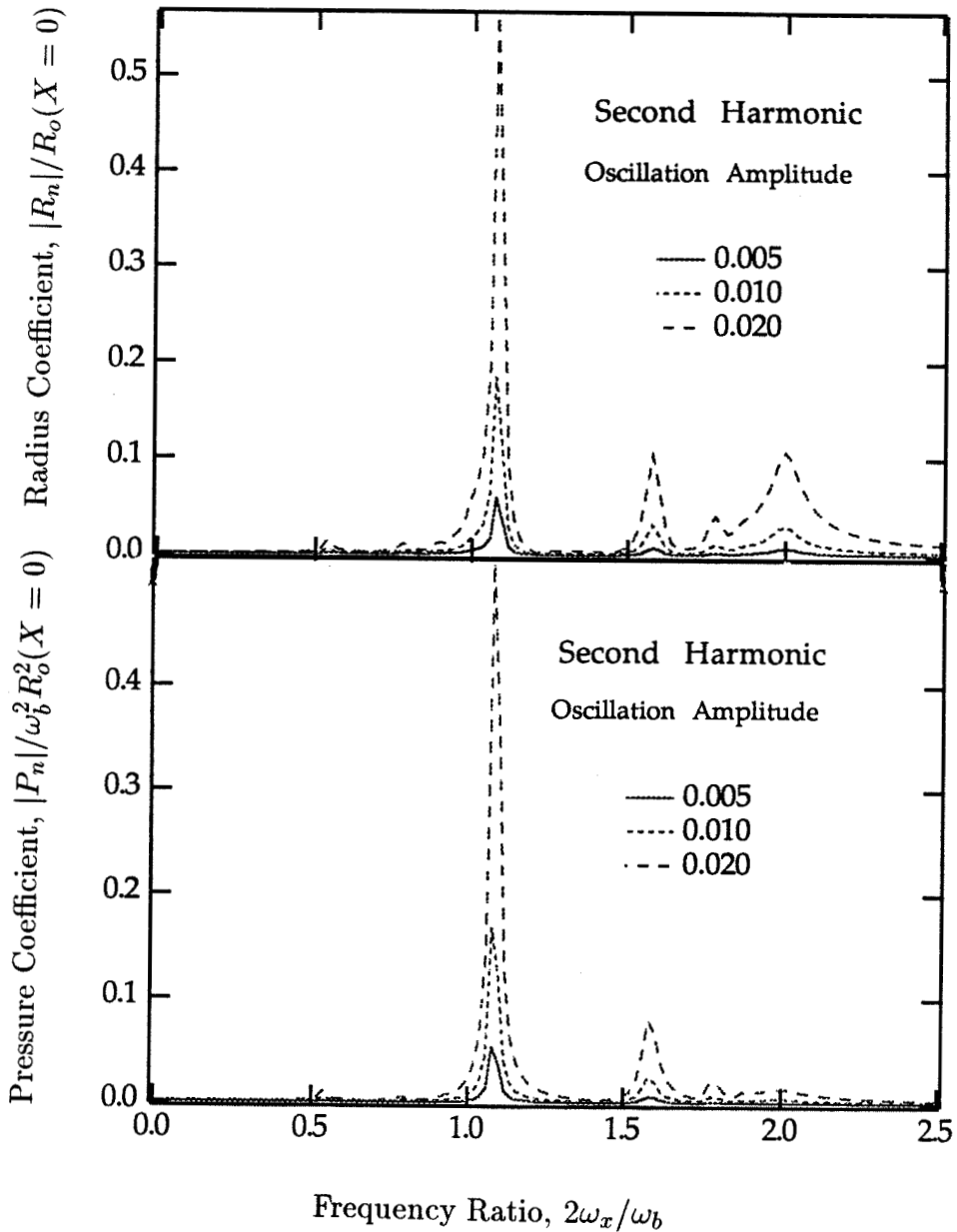


Figure 2.26: The effect of change in the amplitude of wall oscillation, $X_n(0)/R_o$, on the second harmonic; $|R_n|/R_o(X=0)$ and $|P_n|/\omega_b^2 R_o^2(X=0)$ for the second harmonic are plotted against the frequency ratio, $2\omega_x/\omega_b$. The parameters: $\alpha_o=0.02$, $l/R_o=20$ and $\nu/\omega_b R_o^2$ and $S/\rho\omega_b^2 R_o^3$ are for the water tunnel conditions. Values of the amplitude of wall oscillation, $X_n(0)/R_o$, of 0.005, 0.010 and 0.020 are used.

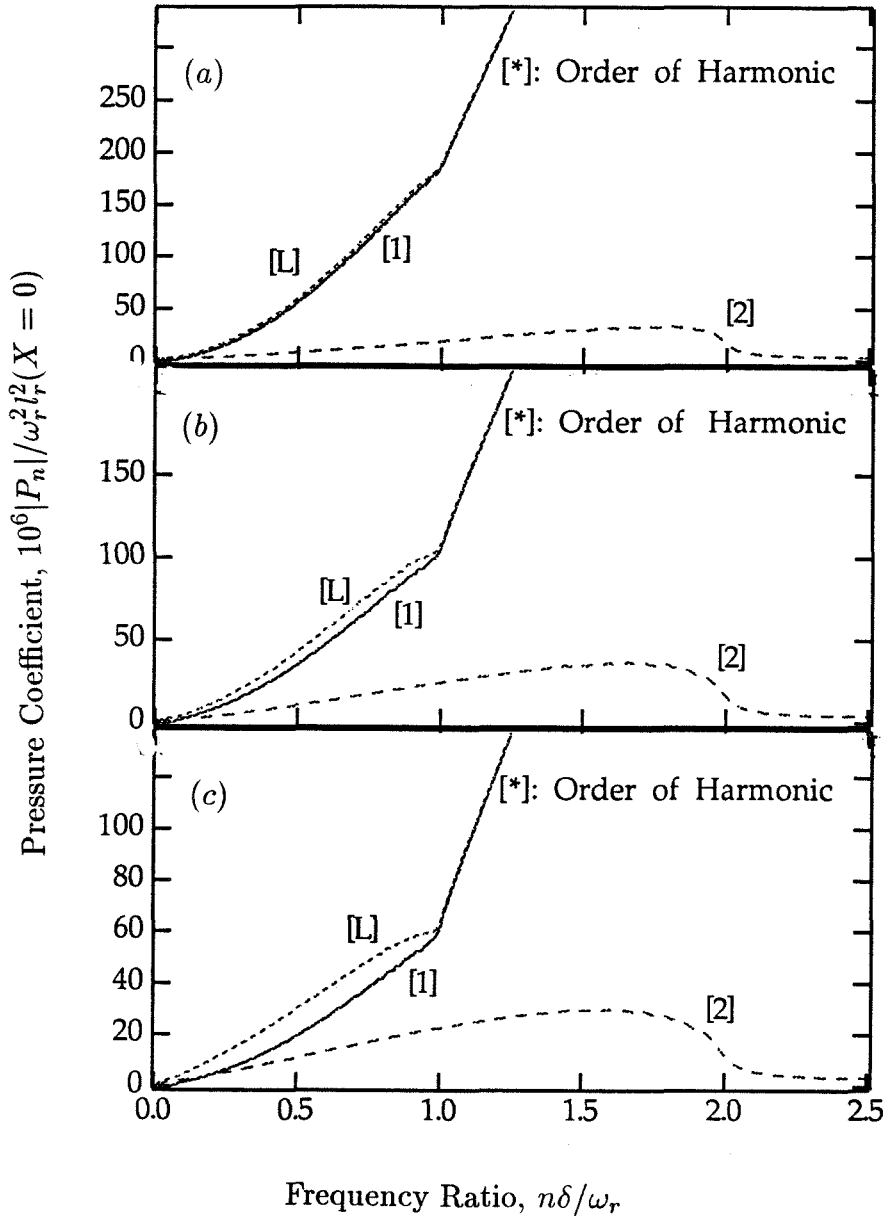


Figure 2.27: The frequency response of a bubbly layer with a given size distribution of bubbles; $|P_n| / \omega_r^2 l_r^2 (X=0)$ is plotted against the frequency ratio, $n\delta / \omega_r$, for the first two harmonics and the linear solution for (a) $m=2$, (b) $m=3$ and (c) $m=4$. The parameters: $X_n(0) / l_r = 0.0002$, $\alpha_o = 0.05$ and the ambient conditions are for the water tunnel.

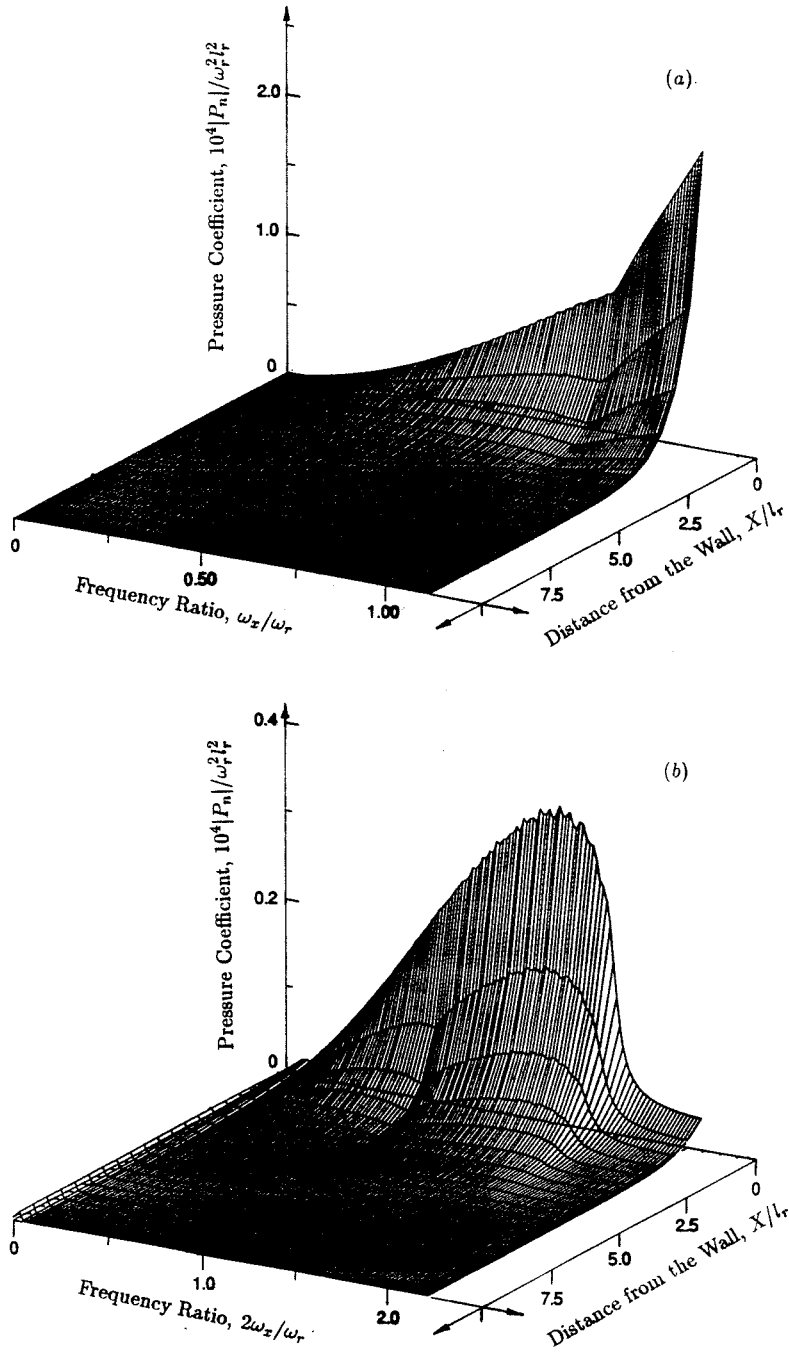


Figure 2.28: The frequency response of a bubbly layer with a given size distribution of bubbles; $|P_n|/\omega_r^2 l_r^2$ for the (a) first and (b) second harmonic is plotted against the distance from the wall, X/l_r , and the frequency ratio, (a) ω_x/ω_r and (b) $2\omega_x/\omega_r$, respectively. The parameters: $X_n(0)/l_r = 0.0002$, $\alpha_o = 0.05$, $m = 3$ and the ambient conditions are for the water tunnel.

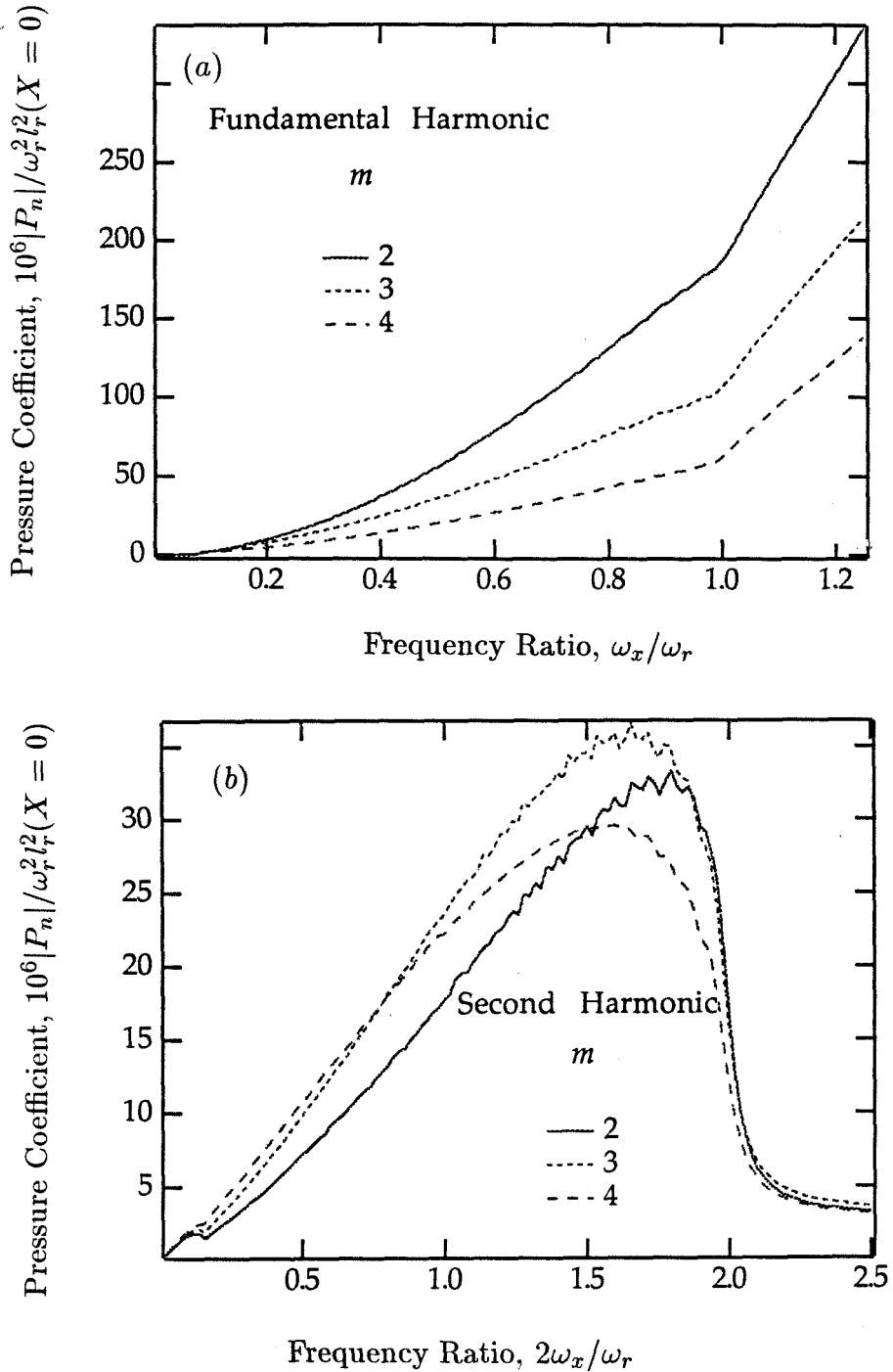


Figure 2.29: The effect of variation in the bubble size density distribution slope, m , on the (a) first and (b) second harmonic; $|P_n| / \omega_r^2 l_r^2 (X=0)$ is plotted against the frequency ratio, (a) ω_x / ω_r and (b) $2\omega_x / \omega_r$, respectively. The parameters: $X_n(0) / l_r = 0.0002$, $\alpha_o = 0.05$ and the ambient conditions are for the water tunnel.

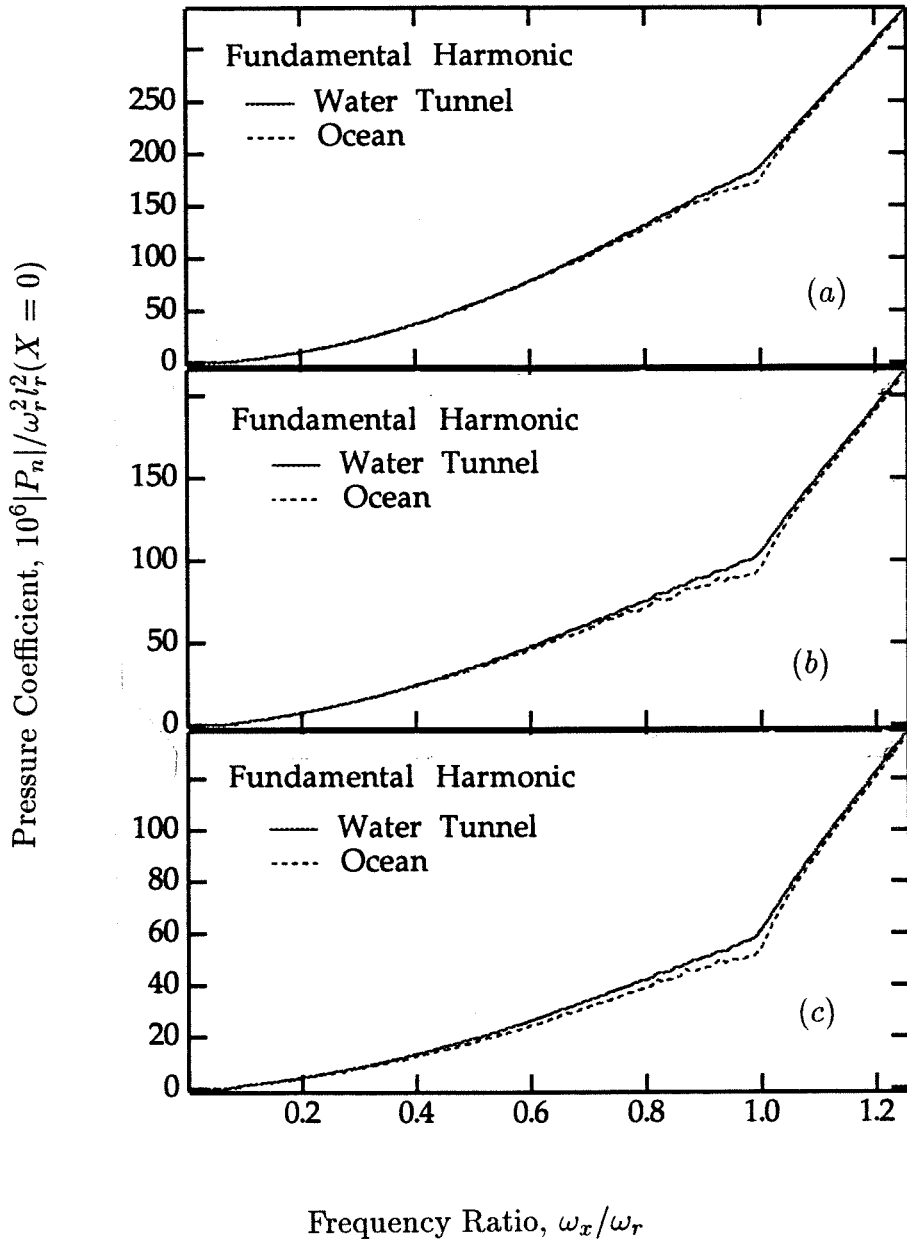


Figure 2.30: The effect of variation in ambient conditions on the fundamental harmonic; $|P_n| / \omega_r^2 l_r^2 (X=0)$ for the fundamental harmonic is plotted against the frequency ratio, ω_x / ω_r , for (a) $m=2$, (b) $m=3$ and (c) $m=4$. The parameters: $X_n(0) / l_r = 0.0002$, $\alpha_o = 0.05$ and the ambient conditions are for the water tunnel and the ocean.

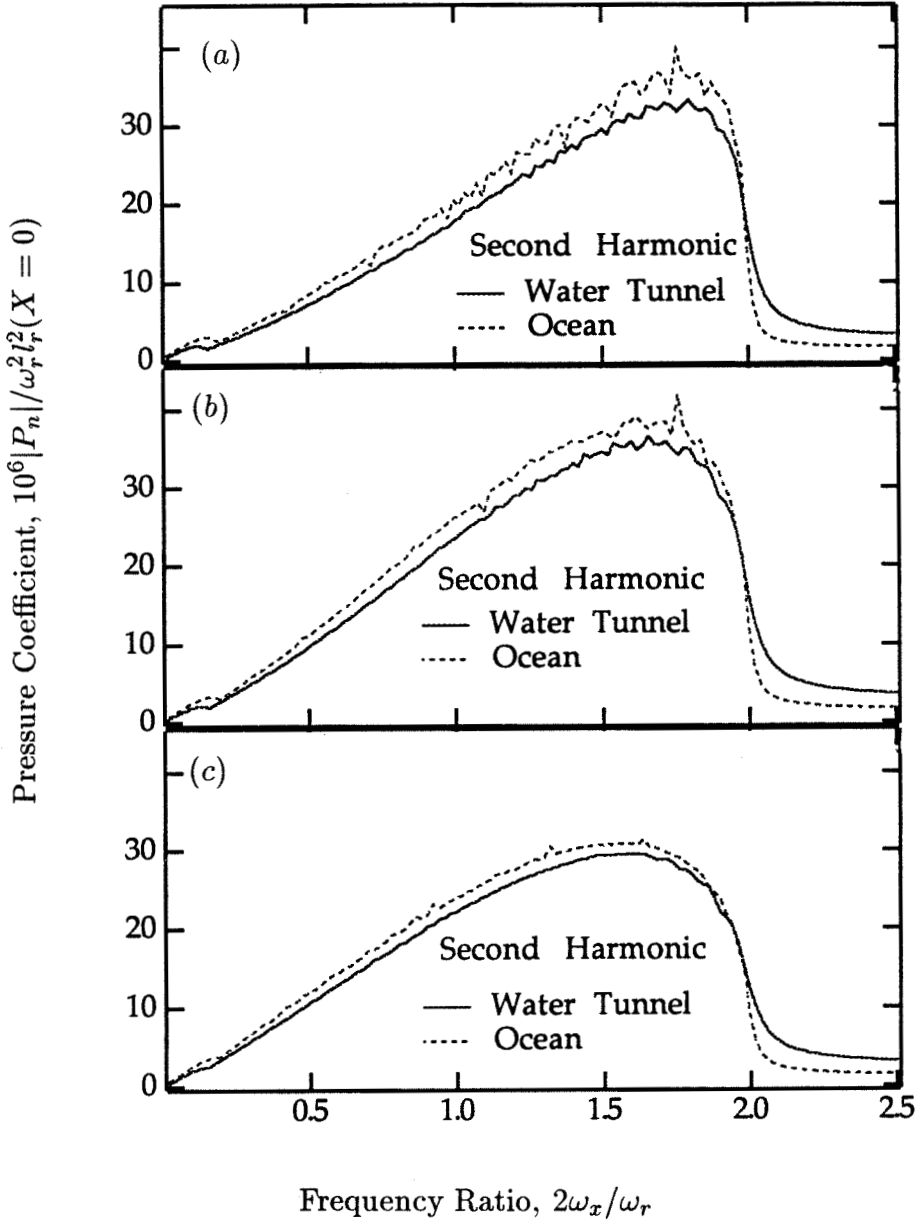


Figure 2.31: The effect of variation in ambient conditions on the second harmonic; $|P_n|/\omega_r^2 l_r^2 (X=0)$ for the second harmonic is plotted against the frequency ratio, $2\omega_x/\omega_r$, for (a) $m=2$, (b) $m=3$ and (c) $m=4$. The parameters: $X_n(0)/l_r=0.0002$, $\alpha_o=0.05$ and the ambient conditions are for the water tunnel and the ocean.

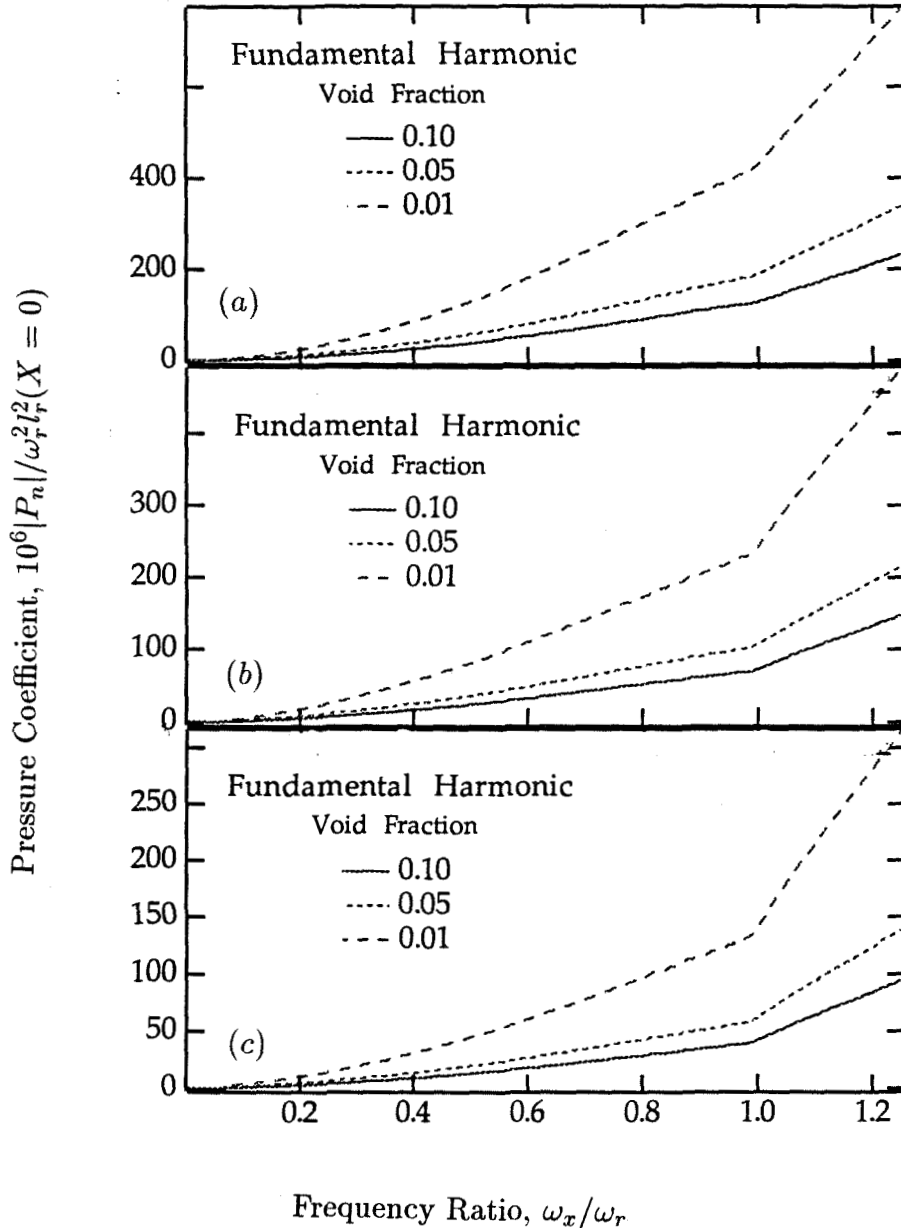


Figure 2.32: The effect of changes in void fraction, α_o , on the fundamental harmonic; $|P_n|/\omega_r^2 l_r^2 (X=0)$ for the fundamental harmonic is plotted against the frequency ratio, ω_x/ω_r , for (a) $m=2$, (b) $m=3$ and (c) $m=4$. The parameters: $X_n(0)/l_r=0.0002$ and the ambient conditions are for the water tunnel. Values of the void fraction, α_o , of 0.01, 0.05 and 0.10 are used.

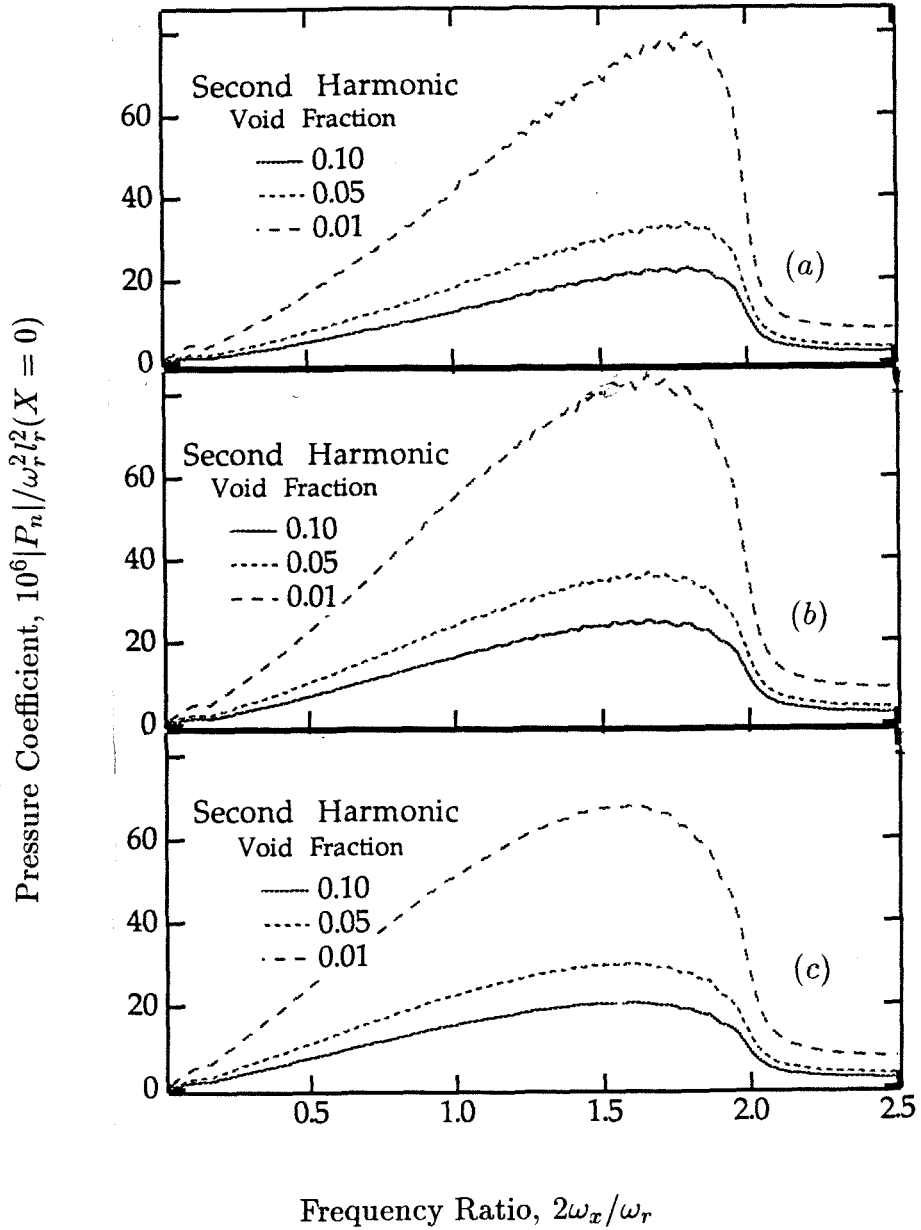


Figure 2.33: The effect of changes in void fraction, α_o , on the second harmonic; $|P_n|/\omega_r^2 l_r^2 (X = 0)$ for the second harmonic is plotted against the frequency ratio, $2\omega_x/\omega_r$, for (a) $m = 2$, (b) $m = 3$ and (c) $m = 4$. The parameters: $X_n(0)/l_r = 0.0002$ and the ambient conditions are for the water tunnel. Values of the void fraction, α_o , of 0.01, 0.05 and 0.10 are used.

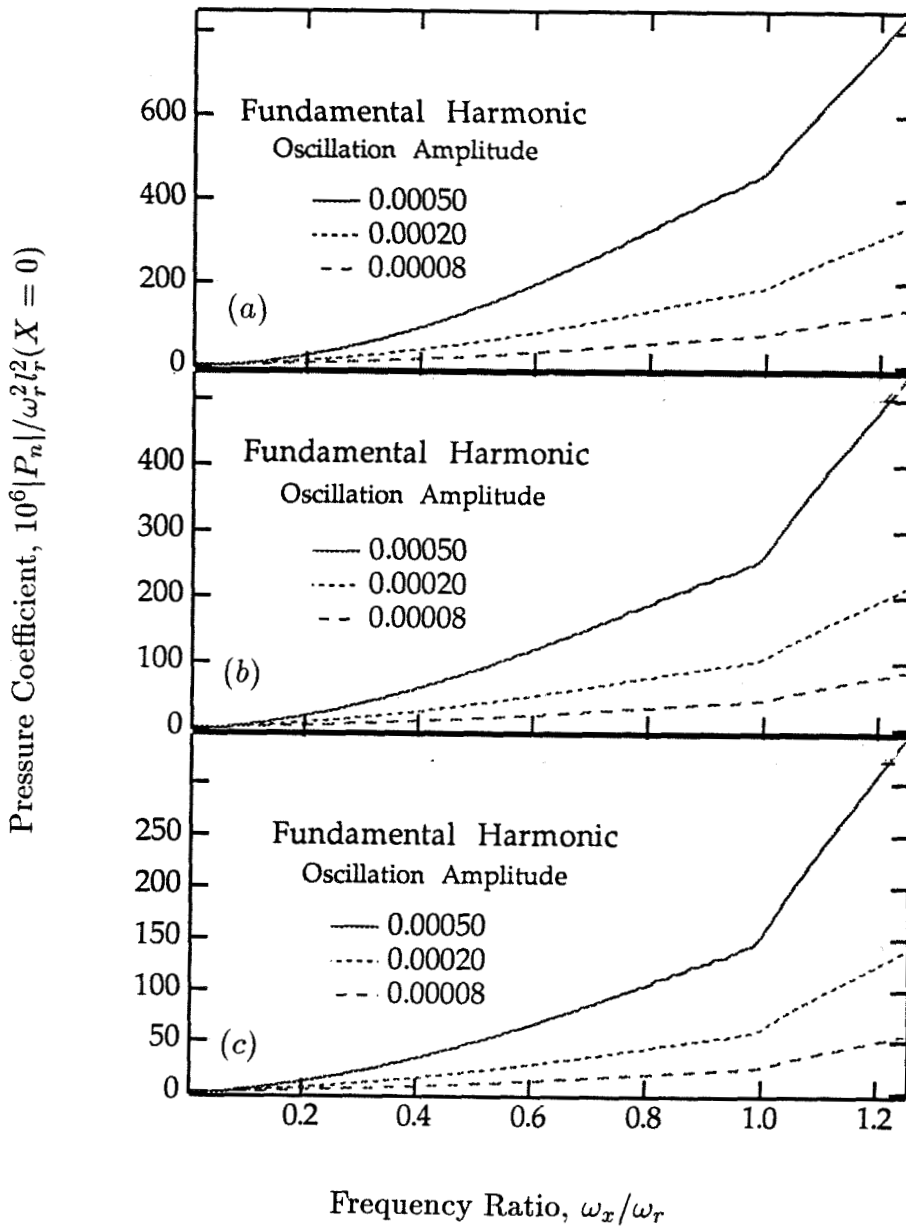


Figure 2.34: The effect of changes in the amplitude of wall oscillation, $X_n(0)/l_r$, on the fundamental harmonic; $|P_n|/\omega_r^2 l_r^2(X=0)$ for the fundamental harmonic is plotted against the frequency ratio, ω_x/ω_r , for (a) $m = 2$, (b) $m = 3$ and (c) $m = 4$. The parameters: $X_n(0)/l_r = 0.0002$ and the ambient conditions are for the water tunnel. Values of the amplitude of wall oscillation, $X_n(0)/l_r$, of 0.00008, 0.0002 and 0.0005 are used.

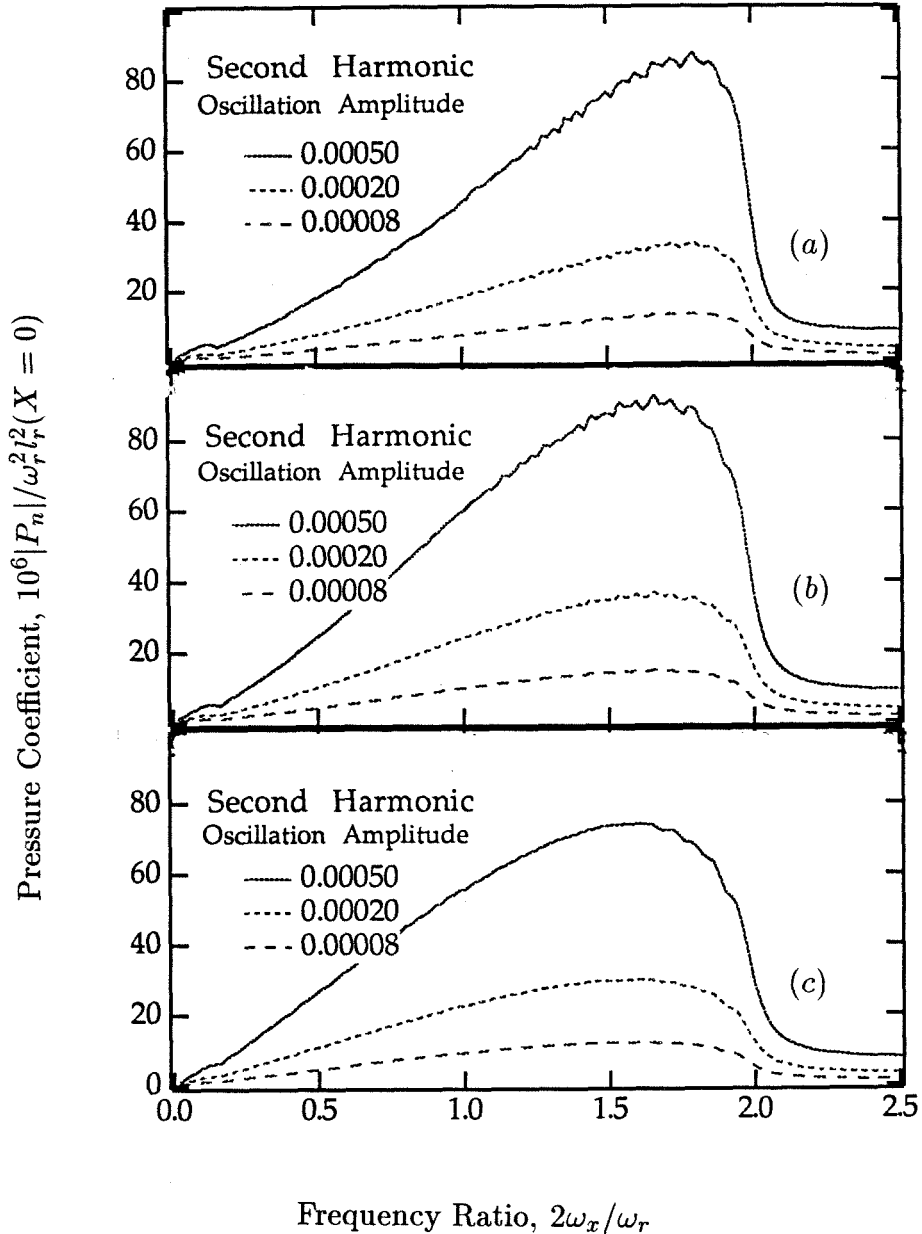
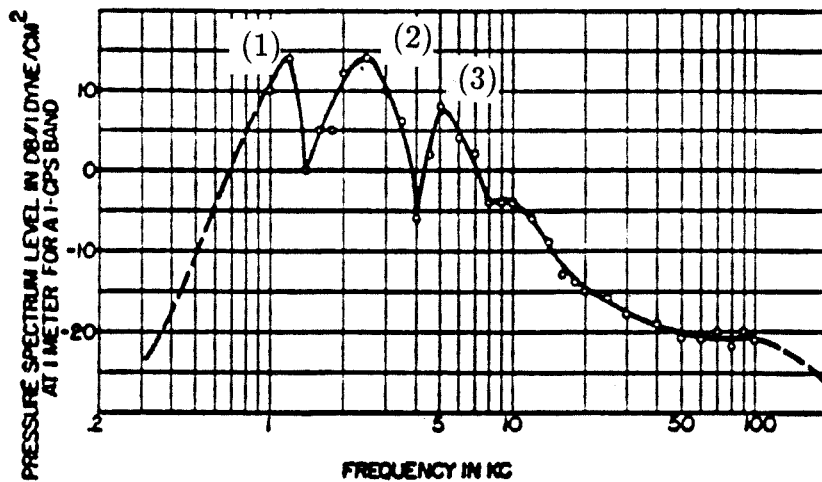


Figure 2.35: The effect of changes in amplitude of wall oscillation, $X_n(0)/l_r$, on the second harmonic; $|P_n|/\omega_r^2 l_r^2 (X=0)$ for the second harmonic is plotted against the frequency ratio, $2\omega_x/\omega_r$, for (a) $m=2$, (b) $m=3$ and (c) $m=4$. The parameters: $X_n(0)/l_r=0.0002$ and the ambient conditions are for the water tunnel. Values of the amplitude of wall oscillation, $X_n(0)/l_r$, of 0.00008, 0.0002 and 0.0005 are used.



Acoustic power spectrum of a 2-in. rod in the Thames River, 0.2-100 kc.

Figure 2.36: The power spectra of noise that is due to cavitation produced by rotating rods in the Thames river (from Mellen (1954)). The peaks at 1.25, 2.5 and 5 kHz (marked respectively as (1), (2) and (3)) may be due to *harmonic cascading*.

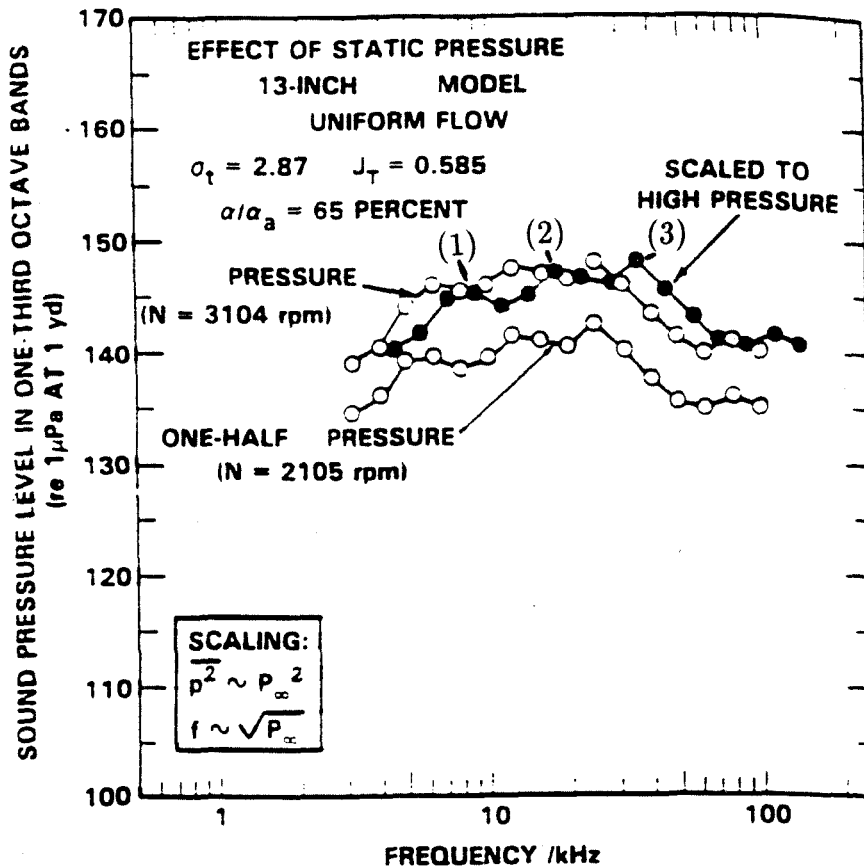


Figure 2.37: The spectra of noise that is due to cavitation on the suction side of a propeller blade (from Blake (1986)). The peaks at 8.5, 17 and 34 kHz (marked respectively as (1), (2) and (3)) may be due to *harmonic cascading*.

Chapter 3

AN ACOUSTICAL STUDY OF TRAVELLING BUBBLE CAVITATION

3.1. Introduction

The dynamics and acoustics of travelling bubble cavitation have been extensively studied both experimentally and theoretically for many years. Most of the theoretical work has focussed on modifications of the Rayleigh equation for a spherically collapsing cavity. Plesset contributed a substantial body of work in this area, and Gilmore (1952) included compressible effects. Deviations from the spherical geometry that are due to the presence of a wall, and the resulting shape deformations were investigated by Plesset and Chapman (1971) and more recently by Blake *et al.* (1986). Fitzpatrick and Strasberg (1956) proposed using the Rayleigh - Plesset equation in combination with the pressure history in the flow to calculate the bubble radius and the resulting noise from the collapse process. Brooke Benjamin (1958) related the presence of f^{-2} variation in the power spectra of the resulting noise to the generation of shocks that are due to effects of compressibility during the bubble collapse process. This research has been summarized in the excellent review by Plesset and Prosperetti (1977).

Experimentally, researchers initially measured the cavitation noise generated in a venturi (Harrison (1952)) and by stirring rods (Mellen (1954)). Photographic and acoustical studies of the collapse of a spark or laser generated cavity in a quiescent liquid have also been used by a number of researchers including Harrison (1952), Mellen (1956a and 1956b) and more recently, Kimoto (1987) and Vogel *et al.* (1989). Photographic studies in such quiescent environments have revealed the presence of a reentrant jet generated by the collapsing bubble as seen in numerical calculations of Plesset and Chapman (1971). Vogel *et al.* have also photographed shock waves resulting from the collapse of such cavities, thus confirming the importance of the effects of liquid compressibility.

A number of researchers, notably Knapp and Hollander (1948), Parkin (1952), Blake *et al.* (1977), Hamilton (1981), Hamilton *et al.* (1982), Marboe *et al.* (1986) and Ceccio and Brennen (1991) have studied the collapse of hydrodynamically generated cavitation bubbles. These studies show that cavitation bubbles are usually hemispherical (Knapp and Hollander (1948), Parkin (1952)). Blake *et al.* (1977) have photographed the collapse of a bubble in cavitation over a tripped hydrofoil where the bubble deforms into a hemispherical shape before collapsing and also breaks up into pieces during the collapse process. A similar pattern of bubble breakup has been observed photographically in travelling bubble cavitation around axisymmetric headforms by Ceccio and Brennen (1991). van der Meulen and van Renesse (1989) have acoustically and photographically studied the collapse of laser produced cavities around hemispherical headforms.

Mellen (1954, 1956a and 1956b) made measurement of spectra of the noise produced by a collapsing cavity and of the cavitation noise produced by stirring rods. The noise generated by hydrodynamic cavitation has been measured by Hamilton (1981), Hamilton *et al.* (1982), Marboe *et al.* (1986), Blake *et al.* (1977). Arakeri and Shanmuganathan (1985) used spectra measurements to determine the value of the void fraction above which interactive effects between bubbles became important. Many researchers have suggested treating the noise pulses as a stochastic process (Morozov (1969), Illichev and Lesunovskii (1963) and Baiter (1974)). This involves using the noise generated by a single collapsing bubble to synthesize the spectra of the noise generated by travelling bubble cavitation (Baiter (1986)).

Some of the earliest studies of a single bubble in cavitation observed the bubble collapsing, growing and collapsing again (Knapp and Hollander (1948)). Harrison (1952) traced the origins of the rebound to the presence of permanent gas in the bubble. Since that time rebounding has been observed in both flow induced cavitation and in the collapse of spark or laser produced cavities. Rebounding

generates two or more pressure pulses separated by a comparatively low pressure level produced by the intermediate growth phase. Another phenomenon called *multipeaking* can be seen in the acoustic signal generated by the collapse of spark produced cavities (Mellen (1956a) and Teslenko (1979)). Ceccio and Brennen (1991) also observed the multiple peaked pulses in the noise from single events.

Thus *rebounding* and *multipeaking* are seen to be characteristic features of the noise generated by collapse of a bubble. The present investigation examines these characteristic features as well as their impact on measures of the acoustic signal such as the spectra. The dependence of multipeaking and rebounding on flow conditions such as cavitation number, flow velocity and to a limited extent on the local flow structure has also been investigated in order to understand the collapse mechanism in travelling bubble cavitation. The results will be compared to the calculations using the Rayleigh–Plesset equation in a manner similar to that proposed by Fitzpatrick and Strasberg (1956). It is hoped that the information yielded by such an investigation can be used in a model similar to the one suggested by Baiter (1986) to construct the spectra of travelling bubble cavitation.

3.2. Experimental Details

The experiments were conducted in the Low Turbulence Water Tunnel (Gates (1977)) at the California Institute of Technology. It is shown schematically in Fig. 3.1. The experimental equipment and installation used by Ceccio and Brennen (1991) were employed in these experiments. All the experiments were conducted at a fixed velocity with the desired cavitation number obtained by lowering the static pressure in the water tunnel. The air content was measured by a Van Slyke apparatus and was maintained between 8 and 10 *ppm*.

Travelling bubble cavitation was produced on the two axisymmetric headforms used by Ceccio and Brennen (1991) namely, a Schiebe headform of diameter 5.08 *cm* (Gates *et al.* (1979)) and an I.T.T.C. headform of 5.59 *cm* diameter

(Lindgren and Johnsson (1966)). The Schiebe headform was designed to suppress laminar separation in cavitating conditions (Schiebe (1972)). It possesses a sharp pressure drop with a minimum pressure coefficient of -0.75. The I.T.T.C. headform possesses a laminar separation region. It has a relatively smooth pressure drop with a minimum pressure coefficient of -0.62. Fig. 3.2 shows profiles and pressure coefficients for these headforms. The headforms were made of lucite in order to make them approximately acoustically transparent in water. An ITC-1042 hydrophone was placed inside the headform interior, which was filled with water. This allows relatively reverberation-free recording of the initial portion of the acoustic signal generated by the cavitation on the surface of the headform. A collapsing bubble is a sound source of monopole type and the sound gets weaker away from this source. Thus reverberation from the tunnel walls reaching the hydrophone is considerably weaker than the original acoustic emission. It means that since the cavitation site is much closer to the hydrophone than it would be if the hydrophone were placed near tunnel walls, the distortion of the signal that is due to the natural acoustic modes of the water tunnel and the acoustic reflections from the water tunnel walls are minimized. However, the acoustic path between the bubble and the hydrophone is not perfectly transparent and some sound may have been lost due to reflection and refraction at the surfaces of the headform. This has been found qualitatively to be insignificant by Ceccio (1990) by comparing the signal to the signal recorded by a far field hydrophone. Also, the output voltage of the hydrophone was converted to pressures using a steady state calibration and this may have introduced some errors since the signals in this experiment are transient. An experimental schematic is included in Figure 3.1.

The signal from the hydrophone was amplified and extremely low frequencies ($\ll 1 \text{ Hz}$) were removed by a high pass filter. The filtered signal was then digitally sampled at 500 kHz . It should be noted that the hydrophone has a corner frequency of 80 kHz . Therefore, the sampling rate of 500 kHz is more than sufficient to

capture the details of the acoustic signal detected by the hydrophone. Thus, for example, the peak amplitudes are meaningful and do not differ appreciably from the actual peak amplitudes measured by the hydrophone. The signals generated by a number of bubbles collapsing next to the headform almost simultaneously have been eliminated by the software used to process the acoustic data. Around 500 acoustic traces were collected for each of six operating conditions comprised of 3 cavitation numbers (0.45, 0.50 and 0.55) and two flow velocities (8 and 9 *m/sec*). The duration of the recording was adjusted to capture the complete acoustic trace from an individual bubble collapse. A typical acoustic trace is shown in Fig. 3.3, and a sketch illustrating the definition of some of the measured quantities is included as Fig. 3.4. These records were digitally processed in the following way. First peaks were detected and classified as belonging to the main pulse or the rebound pulse. Then quantities such as the peak amplitude and the time interval between the peaks were evaluated. In addition, the following quantities were also evaluated:

$$I_m = \int_{t_1}^{t_2} p dt \quad (86)$$

$$I_s = \int_{t_1}^{t_2} p^2 dt \quad (87)$$

$$\tau_w = t_1 - t_2 \quad (88)$$

Here I_m is the acoustic impulse, t_1 and t_2 being times of the beginning and the end of the main pulse (or the rebound pulse). The integral, I_s , is an alternative measure of the strength of the pulse, and τ_w is the duration of the pulse. Also measured were the time between the maximum peaks in the main and the rebound pulses, d and the ratio of maximum amplitude in the main pulse to the maximum amplitude in the rebound pulse, r .

3.3. Experimental Results

3.3.1. Occurrence of Multipeaking and Rebounding

First, the probabilities of occurrence of the phenomena of rebounding and multipeaking were examined statistically in order to gain some insight into these phenomena. The dependence of these probabilities on cavitation number, σ , and to a limited extent on flow velocity, u , are presented in Fig. 3.5 for both headforms. Consider first the phenomenon of multipeaking in the main pulse. The following trends can be clearly seen from the data of Fig. 3.5. First note that changing the flow velocity from 8 to 9 *m/sec* has little effect on results. This is not surprising since change in velocity is small; significantly different velocities could not be obtained because of operational limits on this water tunnel. van der Meulen and van Renesse (1989) also found the flow velocity to have very small effect. Second, the probability of rebounding increases as the cavitation number, σ , is reduced, and this appears to be the case for both the headforms. It is particularly evident that rebounding almost never occurs for the highest of the three cavitation numbers tested, $\sigma = 0.55$. The probability of occurrence of both multipeaking and rebounding is higher for the I.T.T.C. headform than for the Schiebe headform. The main difference between the two headforms is in the probability of multipeaking. For the I.T.T.C. headform, the probability of occurrence of double peaked events is almost independent of σ . Events with more than two peaks almost never occur with the Schiebe headform. The probability of occurrence of multipeaking in the rebound pulse was also examined and exhibited trends similar to the main pulse. As seen in Fig. 3.6, the rebounds are predominantly single peaked (approximately 80 % for the I.T.T.C. headform and 90 % for the Schiebe headform).

It is convenient to classify the cavitation events with a rebound by a combination of two letters, where the first letter represents the number of peaks in the main pulse and the second letter represents the number of peaks in the rebound pulse. We use *m* to denote multiple peaks and *s* to denote a single peak. The

probability of occurrence of different kinds of events is shown in Fig. 3.7. It can be seen that I.T.T.C. headform has mostly *ms*-type events [50 %] but *mm* and *ss*-type events are also present in significant numbers [25 %]. The Schiebe headform has mostly *ss*-type events with *ms*-type events also present about 20 % of the time. It is observed that *sm* events are rare, indicating that a multi-peaked rebound pulse is unlikely if the main pulse is single peaked.

Obviously, the two headforms produce characteristically different events because of the differences in the interaction between the bubble dynamics and the flow structure. The rebound pulse indicates a second collapse separated from the first collapse by a growth phase. van der Meulen and van Renesse (1989) have related the rebounding of the bubble to its distance from the headform. In their study of collapse of the laser produced cavities around hemispherical headforms, the bubbles very close to the headform were observed not to rebound. Thus, the pattern of rebounding may be governed by the distance between the growing nuclei and the headform. Because of the presence of boundary layer separation on the I.T.T.C. headform, the nuclei are expected to be farther from the surface than they are for the Schiebe headform, which does not produce boundary layer separation. Thus, the probability of rebounding would be greater with the I.T.T.C. headform as observed in the present experiments.

The multi-peaking, however, could be the result of several mechanisms as follows:

[a] Multiple peaks may be the result of multiple shock waves emitted during the bubble collapse process (Mellen (1954) and (1956), Kimoto (1987), and Vogel *et al.* (1989)). Collapsing cavities have been observed to generate microjets (Kimoto (1987) and van der Meulen and van Renesse (1989)). Kimoto (1987) has separately measured the pulse resulting from microjet impact and the subsequent pulse generated when the remnant cloud of smaller bubbles collapses. He found that

the remnant cloud shock was about 3 times stronger than the microjet shock and that the time between them was about 0.1 *msec*. The peak separation was roughly 0.015 *msec* in the present experiments. Furthermore, using a Schlieren technique, Vogel *et al.* have observed two shock waves emitted that were due to nonspherical bubble collapse. Hence, the multiplicity of peaks could be the result of a number of shock waves generated during the bubble collapse.

[b] Cavitation bubbles can break up into several pieces while collapsing (as seen by Ceccio (1990) and as shown in Fig. 3.8) and therefore generate two or more peaks. From the photographs of Ceccio one can estimate the two pieces to be 1 mm apart, which at a flow velocity of about 10 *m/sec* would lead to peaks roughly 0.1 *msec* apart. This is substantially larger than the observed peak separation of about 0.015 *msec*. The bubble may break up during the collapse due to shear in the flow or as a result of the onset of higher order oscillations.

[c] Volume oscillations during the collapse process could cause multiple peaks. Since the natural period of oscillation for a 20 μm bubble is 0.015 *msec*, which is consistent with the observed peak separation, volume oscillations during the collapse may be a plausible reason for multiple peaks. The natural oscillations of the bubble can be caused by the strong pressure gradient that the bubble passes through while travelling next to the headform.

[d] van der Meulen and van Renesse (1989) have reported generation of a jet, a counter jet and disintegrating vortex rings during the collapse of a bubble in the flow around a headform. The multiple peaks may be caused by the jet, the counter jet and the disintegrating vortex rings. The production of a counter jet was seen to be promoted by larger distances between the bubble and the surface of the headform.

In particular, this may explain the greater degree of multipeaking for the I.T.T.C. headform than for the Schiebe headform.

The above variations in the probabilities of multipeaking and rebounding are probably governed by the size distribution of the nuclei and by the manner in which the nuclei are ingested into the low pressure zone around the headform. Distinctly different pressure distributions (Fig 3.2) and presence (absence) of the laminar separation probably cause the differences in travelling bubble cavitation around the I.T.T.C. and Schiebe headforms.

3.3.2. Some Characteristic Measures of the Acoustic Signal

We now turn to other statistical features in the acoustic signal by first examining the mean value of the measured quantities. The error bars in the figures 3.10–3.15 have been calculated using a 95 % confidence level following Bendat and Piersol (1971). First, the ratio of the maximum amplitude in the main pulse to the maximum amplitude in the rebound pulse, r , is shown in Fig. 3.9 for the two velocities, for the various types of events and for the two headforms. It is seen that most of the data is clustered around the value of 2. With a 95 % confidence level, we find that the mean value of r will lie between 1.5 and 2.5. It seems that the bubble fission observed by Ceccio and Brennen (1991) happens in such a way that the collapse of the bubble cloud, which is generated by the first collapse, generates only half of the maximum pressure generated by the first collapse. This may mean that during the first collapse, certain nonlinear modes of surface oscillation are set up, which cause the bubble to break up in a repeatable way. A somewhat similar behavior was observed to occur in the results for the ratio of the pulse width, τ_w for the first collapse to the same quantity for the second collapse. This ratio varied between 2 to 4 for the Schiebe headform and 3.5 to 8.25 for the I.T.T.C. headform. Also, the ratio of the impulse, I_m , for the first collapse to that for the second collapse exhibited a similar behavior. Thus, it is clear that collapse after

rebound generates less sound than the main collapse in contrast to the observation made by Hamilton (1981).

The time between the maximum peak in the main pulse and the maximum peak in the rebound pulse, d , was also measured and exhibited a mean value between 0.5 and 1.4 *msec*. We have examined the classic film of Knapp entitled *Studies of Cavitation*, which shows travelling bubble cavitation around a 1.5 caliber ogilvie. The value of d from that film is approximately 1.5 *msec*, which is of the same order of magnitude as the present observation. This lends confirmation to the conclusion that the two pulses in the present acoustic records are emitted by two collapses separated by a growth phase. It is observed that the value of d increased with reduction in the cavitation number and as expected, is larger at 8 *m/sec* than at 9 *m/sec* for both the headforms (Fig. 3.10). van der Meulen and van Renesse (1989) also observed delayed rebound at smaller flow velocities.

Also, the value of d is larger for the I.T.T.C. headform than for the Schiebe headform at both flow velocities and the smaller values of σ (0.50 and 0.45). The reason for this may be the larger radius of the I.T.T.C. headform, which enlarges length scales requiring larger times between the collapses. Also, multipeaking is seen to delay the rebound for reasons that are not understood.

The quantities P , I_m , I_s , τ_w , and τ_s were also examined in order to understand the effect of multipeaking and rebounding on these representative measurements of the acoustic signal. We consider first the variation in the mean value of these quantities with the cavitation number for both headforms. The previously mentioned two letter symbols are used to denote the types of events with a rebound. In addition, *sp* and *mp* indicate single and multipeaked events without a rebound. It is seen from Fig. 3.11 that I_m increases with reduction in cavitation number. The mean values of P and I_s behave in a similar fashion, though the dependence of τ_w on σ is quite different. The pulse width, τ_w , has maximum value for the intermediate cavitation numbers in most cases. An exception to this

trend are *mp* type events for the Schiebe headform for which the pulse width, τ_w , decreases with the decrease in the cavitation number at the flow velocity of 9 *m/sec* and increases with decrease in the cavitation number at the flow velocity of 8 *m/sec*. Fig. 3.12 shows the variation in the peak separation, τ_s . It remains close to 12 μs for the Schiebe headform but increases from 15 μs to 23 – 28 μs for the I.T.T.C. headform as the cavitation number is reduced.

Next, the dependence of the mean value of the above characteristics on the flow velocity, the type of event and the headform will be examined. It was seen from the data that the characteristic measures P , I_m , I_s and τ_w changed in a similar way with changes in the type of event, the flow velocity and the headform. Figs. 3.11 and 3.13–3.15 show some of these results. In case of the I.T.T.C. headform, the mean values of these characteristics for *mp* and *ms* type events are roughly the same, and which are larger than the values for *sp* type events (Fig.3.11). In case of the Schiebe headform, the values for *sp* and *ss* type events are roughly the same, and which are less than the values for *mp* type events. This pattern for the Schiebe headform can be seen only at the cavitation number of 0.45, the uncertainty in the estimate being larger at larger values of σ .

The effect of flow velocity on P , I_m , I_s and τ_w is shown in Fig. 3.13 for the I.T.T.C. headform and Fig. 3.14 for the Schiebe headform. The values of these characteristics at 8 *m/sec* are larger than the values at 9 *m/sec* for the cavitation number of 0.45. This inequality is reversed as the cavitation number is increased to 0.55. The exceptions to this trend are *sp*-type events on the Schiebe headform for which an increase in the flow velocity increases the values of these characteristics.

The value of these characteristics for two headforms were compared for corresponding cases, and typical observations are presented in Fig. 3.15. It is seen that the values of these characteristics for the I.T.T.C. headform are larger than the values for the Schiebe headform at the cavitation number of 0.45. This

inequality disappears as the cavitation number is increased to 0.50 and 0.55. In addition, P has a larger value for the Schiebe headform than for the I.T.T.C. headform at the cavitation number of 0.55 in case of sp -type events. The reasons for these variations are not understood.

3.3.3. Comparison Between Experimental Results and Theoretical Calculations

It is useful to compare the current experimental results to the analytical results calculated from the Rayleigh–Plesset equation:

$$R \frac{D^2 R}{Dt^2} + \frac{3}{2} \left(\frac{DR}{Dt} \right)^2 = \frac{P_v - P_\infty(t)}{\rho} + \frac{P_{go}}{\rho} \left(\frac{R_o}{R} \right)^{3k} - \frac{4\nu}{R} \frac{DR}{Dt} - \frac{2S}{\rho R} \quad (89)$$

This equation governs the response, $R(t)$ of a bubble subject to pressure disturbance, $P_\infty(t)$. R_o is the equilibrium radius. Equation (89) is integrated numerically for different bubble radii, experimental conditions and pressure history for comparison with the experimental data. Pressure distributions for the Schiebe headform (Gates *et al.* (1979)) and the I.T.T.C. headform (Hoyt (1966)) have been determined previously and were employed to construct the pressure time history that a nucleus passing close to the headform would experience, assuming no slip between the fluid and the bubble and a small offset from the stagnation stream line. These pressure distributions are given in Fig 3.2. The radiated acoustic pressure, P_r , is then calculated as

$$P_r(x, t) = \frac{\rho}{4\pi x} \frac{d^2 V}{dt^2} \quad (90)$$

where $V(t)$ is the volume of the bubble and x is the distance from the bubble to the point of measurement. Acoustic pressures resulting from nuclei of various sizes were calculated and used to calculate the impulse, I_m , pulse width, τ_w and time interval between two successive collapses following Equations (86)–(88). Here, t_1 and t_2 were taken to be times when $d^2 V/dt^2 = 0$ on either side of a collapse. The distance x is assumed to be R_h , the headform radius, since that is the location of

the hydrophone in the experiments. To facilitate comparison, these quantities are nondimensionalized as follows:

$$I^* = \frac{4\pi I_m}{\rho U R_h} \quad (91)$$

$$\tau_w^* = \frac{\tau_w U}{R_h} \quad (92)$$

$$d^* = \frac{dU}{R_h} \quad (93)$$

These calculations were used to obtain an envelope for the theoretical data. Values of I^* , τ_w^* , d^* from individual cavitation events have been plotted along with the theoretically obtained envelope in Figs. 3.16 and 3.17, which show τ_w^* and d^* as functions of the impulse, I^* , for the I.T.T.C. headform. The solid and dashed lines indicate the theoretical values for cavitation numbers of 0.6 and 0.3 and form the theoretical envelope. It can be seen from Fig. 3.16 that the data points form a small cluster near the origin for the cavitation number of 0.55. These values are close to the theoretical solution. This cluster becomes larger with the same orientation on the plot as the cavitation number is reduced to 0.50 when most of the data points lie above the theoretical envelope. However, the cluster moves downward and rightward with large values of I^* and small values of τ_w^* when the cavitation number is reduced further to 0.45. Now most of the data are seen to lie below the theoretical values. Though the model based on the Rayleigh–Plesset equation yields results that are the right order of magnitude, it fails to predict the dependence of the pulse width, τ_w^* , on the cavitation number. It might be argued that experimentally obtained values of τ_w^* are highly susceptible to error. However, τ_w^* is halved as the cavitation number is reduced from 0.50 to 0.45, which is larger than any uncertainty in the measurement.

Fig. 3.17 shows a similar plot for the time between the first and the second collapses, d^* , as a function of the impulse, I^* . It is seen that most of the experimental values for the cavitation numbers of 0.55 and 0.50 lie in the

theoretical envelope. However, as the cavitation number is reduced to 0.45, the data show a wide scatter. Note that definitive conclusions were difficult to arrive at since rebounds are not numerous.

Figs. 3.18 and 3.19 illustrate the dependence of the data on the flow velocity. A smaller flow velocity delays the rebound (Fig. 3.18). It appears that the first and second collapses occur at specific locations (determined by the pressure distribution) on the headform. The smaller flow velocity is expected to increase this interval for negligible slip between the bubble and the flow. On the other hand, a larger flow velocity is seen to increase the pulse width, τ_w^* (Fig. 3.19), which is contrary to what may be expected and this may indicate significant relative motion between the bubble and the fluid during the collapse process.

It is noteworthy that the time between the main pulse and the rebound, d^* , is well correlated to the impulse, I^* for cavitation number of 0.50 (Fig. 3.18) but shows wide scatter for the cavitation number of 0.45 (Fig. 3.17). The reasons for this are not understood.

It is clear from Figs. 3.16–3.19 that present experimental data for I^* , τ_w^* and d^* are closer to the values predicted by the Rayleigh–Plesset model than the Impulse and maximum bubble volume data by Ceccio and Brennen (1991). It appears that the Rayleigh–Plesset model overestimates the maximum volume of the bubble while it predicts right order of magnitude for the Impulse, I^* , pulse width, τ_w^* and the time between the first and second collapse, d^* . It should also be noted that the Rayleigh–Plesset equation includes only viscous dissipation and does not model break up of a bubble which is the primary source of energy dissipation in our experiments. Thus a bubble undergoes at most one rebound in our experiments while multiple rebounds are predicted by the Rayleigh–Plesset equation.

3.3.4. Power Spectra Measurement

In order to examine the spectral content of the cavitation, the hydrophone output was sampled at 1 MHz and about 200 acoustic traces of 16384 data points each were collected for each operating condition. These data records were processed to obtain a separate record of 8192 points for each cavitation event in the record, which were then used to calculate the power spectra. These data sets were processed to classify each of them by the two letter combination used earlier. It was found that the data sets predominantly contained events of *mp* and *sp* type. Thus, power spectra calculations can be meaningfully used to examine the effect of multi-peaking and its variation with flow conditions. All the individual spectral density data available for each type of event are averaged to yield mean power spectral density relevant to that type.

We first examine the variation in total spectral power with the type of event and the flow conditions. Secondly, the distribution of total spectral power over different frequencies will be examined. This has been achieved by nondimensionalizing the power spectral density by total spectral power to yield nondimensional power spectral density. The sum of the ordinates lying between two frequencies in such a graph gives the fraction of total spectral power emitted between those two frequencies. The nondimensionalization has been carried out as follows. The mean power spectral density is given by A_i , $i = 1, (N + 1)/2$, where i indicates the frequency of $(i - 1)R'/N$, R' is the sampling rate and N is the total number of data points in the record. Then, P_s^* is defined as

$$P_s^* = 0.5[A_1 + A_{N/2+1}] + \sum_{i=2}^{N/2} A_i \quad (94)$$

and the total spectral power is given as

$$P_s \approx P_s^*/R'N \quad (95)$$

Nondimensional values of A_i are defined as

$$a_i = A_i/P_s^* \quad (96)$$

Then the value of $\sum_{i=m}^n a_i$ gives the fraction of total spectral power contained between the frequencies given by $(m-1)R'/N$ and $(n-1)R'/N$. This nondimensional spectral density is used to understand the distribution of spectral energy. Similar nondimensionalized power spectral densities may be used to study the interference effects in bubbly mixtures in a manner similar to that of Arakeri and Shanmuganathan (1985).

The error in the spectra calculation is estimated using the methods of Bendat and Piersol (1980) in which the normalized standard error ϵ is given by

$$\epsilon = 1/\sqrt{\eta} \quad (97)$$

where η is number of data sets used to calculate the average power spectra. The bias error in the calculation is assumed to be negligible. With a 95 % confidence level, the percentage limits on the average value of power spectra are approximately given by $100.0/[1 \pm 2\epsilon]$. This error is listed in Table 3.1 for different types of flow conditions and events and represents the maximum percentage uncertainty in the value of spectral power density at every frequency in the measurement range. The total spectral power will have the same maximum percentage uncertainty. The total spectral power is assumed to have zero uncertainty in order to estimate maximum percentage uncertainty in the nondimensional spectral density. Furthermore, percentage errors listed in Table 3.1 also represent maximum percentage uncertainty in nondimensional spectral density.

Figs. 3.20 and 3.21 illustrate the variation in the total spectral power with flow conditions for the two headforms. The total spectral power, P_s , is a measure of the sound energy emitted. The results for the I.T.T.C. headform, shown in Fig.

3.20, are considered first. It is clear that P_s is larger for mp -type events compared to sp -type events and does not show any consistent variation with flow velocity or cavitation number. On the other hand, for the Schiebe headform, P_s decreases monotonically with increasing cavitation number and increases with increasing velocity (Fig. 3.21). Again, P_s is larger for mp -type events than for sp -type events at the cavitation number of 0.45, though the difference is small at larger cavitation numbers.

The above results for P_s differ from the results for I_s explored earlier. But it is important to recall that the total spectral power, P_s , contains the effects of reverberations from the water tunnel, whereas I_s is a measure of the total spectral power in the acoustic pulse alone.

The nondimensional spectral power density is also calculated from the model based on the Rayleigh-Plesset equation. The radiated acoustic pressure calculated from the volume oscillations of the bubble is used to obtain the power spectrum, which is nondimensionalized in the same manner as the power spectrum of the experimental acoustic records (Equation (96)). A typical comparison of the nondimensional spectral power density is shown in Fig. 3.22. The cavitation noise has a larger fraction of P_s emitted in the low frequency region compared to the noise calculated from the Rayleigh-Plesset equation. Consider some features of the experimental power spectrum. The spectrum decays as $f^{-1.2}$ for frequencies less than 80 kHz . It is clear that no shock waves are detected through the hydrophone since their presence would be indicated by an f^{-2} decay in the spectra (Brooke Benjamin(1958)). The decay of $f^{-0.6}$ predicted by the Rayleigh-Plesset model is not seen in the data. The reasons for the discrepancy between the theoretical and experimental results are probably that the complex processes of bubble collapse are not adequately modeled by the Rayleigh-Plesset equation.

The changes in the nondimensional power spectra were examined in order to understand the redistribution of the spectral energy that was due to changes

in the cavitation number, the flow velocity, the type of event and the headform. Some of the significant results are shown in Figs. 3.23–3.30 and are discussed below. The details are listed in Tables 3.2–3.5. It is important to note that these differences are meaningful since uncertainty is around 30 % in most cases, while the differences in the spectra are in the orders of magnitude.

The changes in nondimensional spectral density that are due to reduction in the cavitation number are shown in Fig. 3.23 for the I.T.T.C. headform and Fig. 3.24 for the Schiebe headform, and the details are summarized in Table 3.2. The spectral energy of the cavitation events on the I.T.T.C. headform shifts from medium and high frequencies to low frequencies as the cavitation number is reduced at a flow velocity of 8 m/sec (Fig. 3.23). In particular, the spectral energy contained between the frequencies of 30 kHz and 60 kHz is significantly reduced. Note that the peak separation, τ_s , also increases from 15 μsec ($1/66 kHz^{-1}$) to 28 μsec ($1/36 kHz^{-1}$) with the same reduction in the cavitation number, which suggests that changes in the spectral energy distribution and the *effective width* of the acoustic pulse represented by the peak separation τ_s are correlated. For mp -type events on the Schiebe headform, the spectral energy is transferred from high frequencies to medium frequencies (Fig. 3.24), and the fraction of spectral energy contained between the frequencies of 50 kHz and 80 kHz is significantly reduced. However, these changes do not appear related to the variation in the peak separation. The details of the changes in spectral energy distribution in other cases are listed in the Table 3.2.

Spectral energy distribution is not affected by multi-peaking except in a few cases for the Schiebe headform (Table 3.3). Fig 3.25 shows a typical comparison between the nondimensional spectra for sp - and mp -type events on the Schiebe headform. It appears that spectral energy is transferred from high frequencies to medium frequencies as a result of multi-peaking. In particular, reduction of the fraction of spectral energy contained between the frequencies of 50 kHz and 75 kHz

is significant. Such a reduction may be caused by the increase in *effective width* of the acoustic pulse as a result of the multi-peaking.

The effect of flow velocity on nondimensional spectral density has been examined next. For low cavitation number events on the I.T.T.C. headform, the spectral energy is transferred from low frequencies to medium and high frequencies as a result of increase in flow velocity (Fig. 3.26). The fraction of spectral energy contained between 25 *kHz* and 65 *kHz* is observed to be significantly increased by the increase in flow velocity. On the other hand, the spectral energy is transferred from high and medium frequencies to very low frequencies with increase in flow velocity for the events on the Schiebe headform (Fig. 3.27). The extent of this energy transfer decreases with the reduction in cavitation number. The details of the effect of change in flow velocity on nondimensional spectral density are summarized in Table 3.4.

Nondimensional spectral density for the two headforms are compared next. At the flow velocity of 8 *m/sec*, the Schiebe headform has a larger fraction of spectral energy in the low frequency range as compared to the I.T.T.C. headform (Fig. 3.28) at the cavitation number of 0.55. As the cavitation number is reduced to 0.45, the Schiebe headform has a smaller fraction of spectral energy in the low frequency range as compared to the I.T.T.C. headform (Fig. 3.29). In comparison, the Schiebe headform has a larger fraction of spectral energy in the low frequency range at the flow velocity of 9 *m/sec* (Fig. 3.30). The details of the differences in spectral energy distribution between two headforms are summarized in Table 3.5.

3.4. Summary

In present experiments on travelling bubble cavitation around axisymmetric headforms, the cavitation bubbles were seen to collapse, rebound and collapse again, resulting in an acoustic signal consisting of two pulses, a phenomenon known as rebounding. Each of the pulses in the acoustic signal produced by

a single cavitation event may contain more than one peak. This is known as multi-peaking. The occurrence of rebounding and multi-peaking and their impact on some of the characteristic measures of the acoustic signal such as spectra have been investigated in order to learn more about the process of cavitation bubble collapse and about sound emission in travelling bubble cavitation.

It is observed that for the I.T.T.C. headform, multi-peaking and rebounding increase with reduction in cavitation number. However, for the Schiebe headform, multi-peaking decreases and rebounding increases as the cavitation number is reduced. The flow velocity seems to have little effect on these results. In the case of the Schiebe headform, most events with a rebound produced single peaked acoustic pulses, whereas in the case of the I.T.T.C. headform, most such events produced a multi-peaked pulse from the first collapse, followed by a single peaked pulse from the second collapse. The ratio of peak amplitude of the main pulse to the peak amplitude of the rebound pulse is close to 2.0 for all flow conditions and types of events. This may indicate a fairly repeatable process of bubble fission and rebound. Some factors such as smaller cavitation number, smaller flow velocity and multi-peaking are seen to delay the rebound.

Other features of the single bubble acoustic output such as P , I_m , I_s and τ_w were examined to understand the effect of changes in cavitation number, flow velocity and local flow structure. It was found that all of these except the pulse width τ_w increased significantly in magnitude with the reduction in cavitation number. Multi-peaking and rebounding were seen to increase the magnitude of these characteristics. The peak separation, τ_s , was practically constant at $12 \mu s$ for the Schiebe headform but increased from $15 \mu s$ to $23-28 \mu s$ with reduction in cavitation number for the I.T.T.C. headform. These characteristics had larger values for the smaller flow speed than at cavitation number of 0.45, and this inequality was reversed with an increase in the cavitation number to 0.55. These characteristics also had larger values for the I.T.T.C. headform than for the Schiebe

headform at cavitation number of 0.45 and this inequality disappeared with an increase in cavitation number to 0.55. Both of these variations were observed for all of the characteristics, P , I_m , I_s and τ_w .

Theoretical investigation based on the Rayleigh–Plesset equation is seen to predict right order of magnitude for these quantities but fails to predict properly the dependence of pulse width on cavitation number. The theory does not predict the distribution of spectral energy well.

The fraction of spectral energy contained in the high frequency range (30kHz–80kHz) is reduced by reduction in the cavitation number. This appears correlated to an increase in *effective width* of the pulse represented by peak separation, τ_s , in the case of the I.T.T.C. headform. Similar reduction in the fraction of the spectral energy contained in high frequencies occurs for the Schiebe headform because of multi-peaking. This may also be due to an increase in the *effective width* of the acoustic signal caused by multi-peaking.

An increase in flow velocity increases the fraction of spectral energy contained in high frequencies for the I.T.T.C. headform. However, the effect is just the opposite for the Schiebe headform for which the fraction of spectral energy contained in high frequencies is reduced by an increase in flow velocity.

All these variations do not appear correlated, and thus each of these details is an important piece in the detailed picture of bubble collapse in travelling bubble cavitation.

Table 3.1
Percentage Errors in Power Spectral Density

Headform	σ	U <i>m/sec</i>	Range of	Range of
			% error	% error
			Single Peaked Events (<i>sp</i>)	Double Peaked Events (<i>dp</i>)
I.T.T.C.	0.55	8.0	-17.332 → 26.527	-21.394 → 37.394
I.T.T.C.	0.50	8.0	-18.274 → 28.801	-22.773 → 41.821
I.T.T.C.	0.45	8.0	-18.661 → 29.772	-21.713 → 38.380
I.T.T.C.	0.55	9.0	-17.411 → 26.714	-22.967 → 42.479
I.T.T.C.	0.50	9.0	-17.656 → 27.295	-23.583 → 44.635
I.T.T.C.	0.45	9.0	-18.274 → 28.801	-22.584 → 41.189
Schiebe	0.55	8.0	-14.119 → 19.674	-22.401 → 40.583
Schiebe	0.50	8.0	-13.166 → 17.872	-37.618 → 151.904
Schiebe	0.45	8.0	-16.202 → 23.969	-32.663 → 94.202
Schiebe	0.55	9.0	-13.437 → 18.375	-26.428 → 56.058
Schiebe	0.50	9.0	-13.333 → 18.182	-36.603 → 136.603
Schiebe	0.45	9.0	-16.879 → 25.481	-32.663 → 94.202

Table 3.2

Changes in the Nondimensional Power Spectral Density

Cavitation Number Reduction

	0.55 \rightarrow 0.50		0.50 \rightarrow 0.45	
	increase	decrease	increase	decrease
I.T.T.C. - <i>sp</i> - 8	<i>No Change</i>	<i>No Change</i>	0 - 0.2	0.2 - 13, 30 - 70
I.T.T.C. - <i>mp</i> - 8	<i>No Change</i>	<i>No Change</i>	0 - 0.2	0.2 - 5, 23 - 60
I.T.T.C. - <i>sp</i> - 9	<i>No Change</i>	<i>No Change</i>	<i>No Change</i>	<i>No Change</i>
I.T.T.C. - <i>mp</i> - 9	0 - 0.15, 1 - 2.5 4.5 - 23, 57 - 71	0.15 - 1, 2.5 - 4.5	<i>No Change</i>	
Schiebe - <i>sp</i> - 8	<i>No Change</i>	<i>No Change</i>	<i>No Change</i>	<i>No Change</i>
Schiebe - <i>mp</i> - 8	0.25 - 10	30 - 97	<i>No Change</i>	<i>No Change</i>
Schiebe - <i>sp</i> - 9	<i>No Change</i>	<i>No Change</i>	0.5 - 61	0 - 0.2
Schiebe - <i>mp</i> - 9	<i>No Change</i>	<i>No Change</i>	0.2 - 60	0 - 0.2, 60 - 77

The left column indicates the headform, the type of event and the flow velocity.

The numbers indicate the frequency range (in *kHz*) in which the spectral energy content is increased (decreased) as a result of change in the flow condition given at the top of the columns.

No Change indicates that no change in the spectral energy distribution is observed as a result of change in the flow condition.

Table 3.3

Changes in the Nondimensional Power Spectral Density

Effect of Multipeaking

sp → *mp*

	increase	decrease
I.T.T.C. - 0.55 - 8	<i>No Change</i>	<i>No Change</i>
I.T.T.C. - 0.55 - 9	<i>No Change</i>	<i>No Change</i>
I.T.T.C. - 0.50 - 8	<i>No Change</i>	<i>No Change</i>
I.T.T.C. - 0.50 - 9	<i>No Change</i>	<i>No Change</i>
I.T.T.C. - 0.45 - 8	<i>No Change</i>	<i>No Change</i>
I.T.T.C. - 0.45 - 9	<i>No Change</i>	<i>No Change</i>
Schiebe - 0.55 - 8	<i>No Change</i>	<i>No Change</i>
Schiebe - 0.55 - 9	<i>No Change</i>	<i>No Change</i>
Schiebe - 0.50 - 8	0 - 10	10 - 100
Schiebe - 0.50 - 9	<i>No Change</i>	<i>No Change</i>
Schiebe - 0.45 - 8	0.3 - 10	0 - 0.3, 30 - 70
Schiebe - 0.45 - 9	0.5 - 10	40 - 74

The left column indicates the headform, the cavitation number and the flow velocity.

The numbers indicate the frequency range (in *kHz*) in which the spectral energy content is increased (decreased) as a result of change in the flow condition given at the top of the columns.

No Change indicates that no change in the spectral energy distribution is observed as a result of change in the flow condition.

Table 3.4

Changes in the Nondimensional Power Spectral Density
Effect of Flow Velocity

	8 → 9 m/sec	
	increase	decrease
I.T.T.C. - <i>sp</i> - 0.55	<i>No Change</i>	<i>No Change</i>
I.T.T.C. - <i>sp</i> - 0.50	<i>No Change</i>	<i>No Change</i>
I.T.T.C. - <i>sp</i> - 0.45	0.23 - 64	0 - 0.23
I.T.T.C. - <i>mp</i> - 0.55	<i>No Change</i>	<i>No Change</i>
I.T.T.C. - <i>mp</i> - 0.50	0 - 0.2, 5 - 24	0.2 - 5, 24 - 51
	57 - 68	
I.T.T.C. - <i>mp</i> - 0.45	0.2 - 14, 24 - 64	0 - 0.2
Schiebe - <i>sp</i> - 0.55	0 - 0.2	0.2 - 100
Schiebe - <i>sp</i> - 0.50	0 - 0.2	0.2 - 100
Schiebe - <i>sp</i> - 0.45	<i>No Change</i>	<i>No Change</i>
Schiebe - <i>mp</i> - 0.55	0 - 0.2	0.2 - 100
Schiebe - <i>mp</i> - 0.50	0 - 0.2	0.2 - 10
	52-85	
Schiebe - <i>mp</i> - 0.45	<i>No Change</i>	<i>No Change</i>

The left column indicates the headform, the type of event and the cavitation number.

The numbers indicate the frequency range (in *kHz*) in which the spectral energy content is increased (decreased) as a result of change in the flow condition given at the top of the columns.

No Change indicates that no change in the spectral energy distribution is observed as a result of change in the flow condition.

Table 3.5

Changes in the Nondimensional Power Spectral Density

Difference Between Two Headforms

I.T.T.C. → Schiebeheadform

	increase	decrease
<i>sp</i> - 8 - 0.55	0 - 0.32, 61 - 108	2 - 9.3
<i>sp</i> - 8 - 0.50	0 - 0.3, 20 - 74	0.3 - 6
<i>sp</i> - 8 - 0.45	0.2 - 100	0 - 0.2
<i>sp</i> - 9 - 0.55	0 - 0.3	0.3 - 64
<i>sp</i> - 9 - 0.50	0 - 0.3	0.3 - 37
<i>sp</i> - 9 - 0.45	0.1 - 0.4	2 - 21
<i>mp</i> - 8 - 0.55	0 - 0.3, 16 - 90	0.3 - 9
<i>mp</i> - 8 - 0.50	0 - 0.3, 6 - 10	0.3 - 3.6, 66 - 80
<i>mp</i> - 8 - 0.45	0.17 - 53	0 - 0.17, 55 - 70
<i>mp</i> - 9 - 0.55	0 - 0.3	0.3 - 66
<i>mp</i> - 9 - 0.50	0 - 0.3	0.3 - 24
<i>mp</i> - 9 - 0.45	0 - 0.3	1 - 7, 45 - 66

The left column indicates the type of event, the flow velocity and the cavitation number.

The numbers indicate the frequency range (in *kHz*) in which the spectral energy content is increased (decreased) as a result of change in the flow condition given at the top of the columns.

No Change indicates that no change in the spectral energy distribution is observed as a result of change in the flow condition.

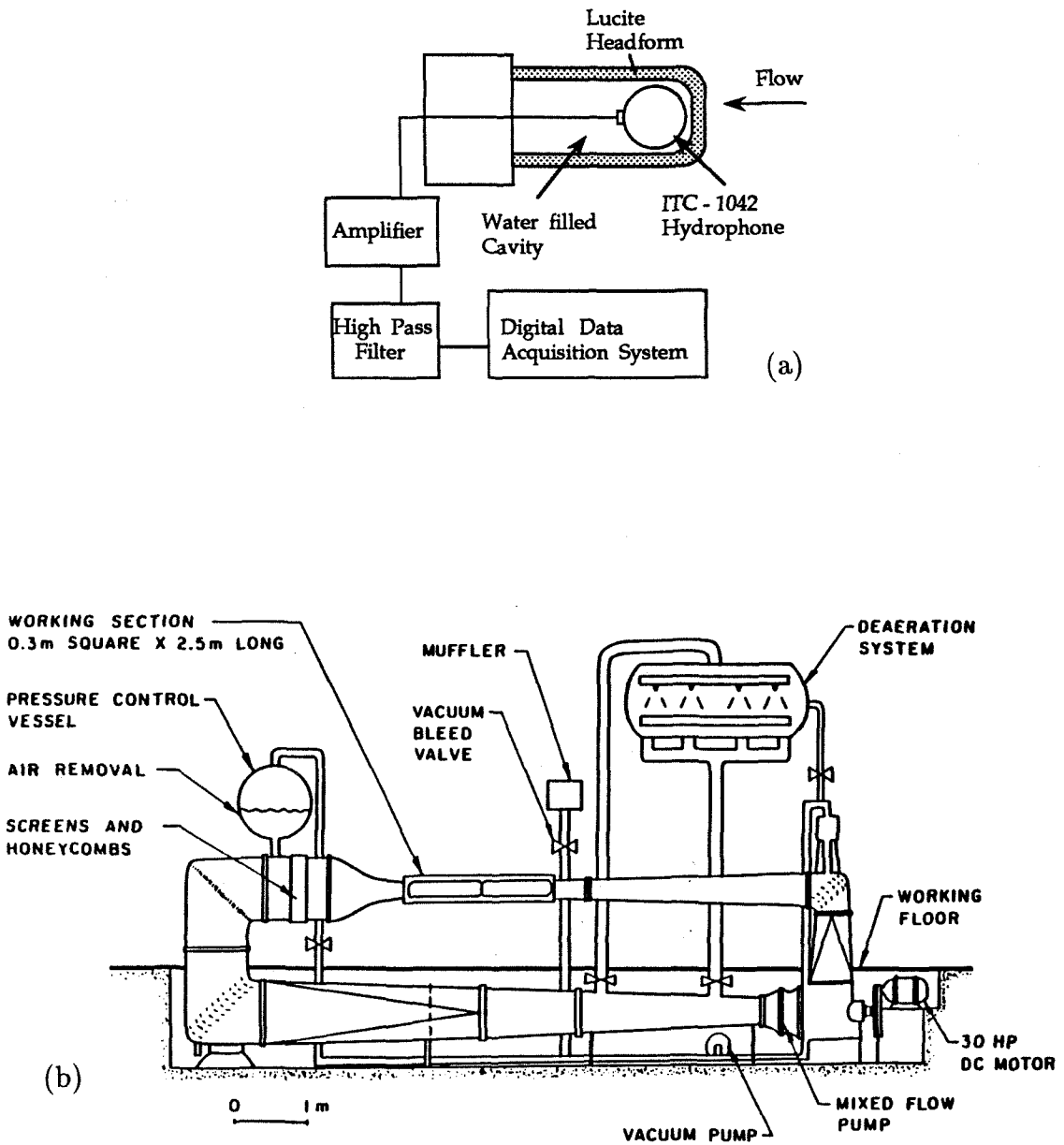


Figure 3.1: Schematics illustrating (a) instrumentation of the headform and (b) Low Turbulence Water Tunnel.

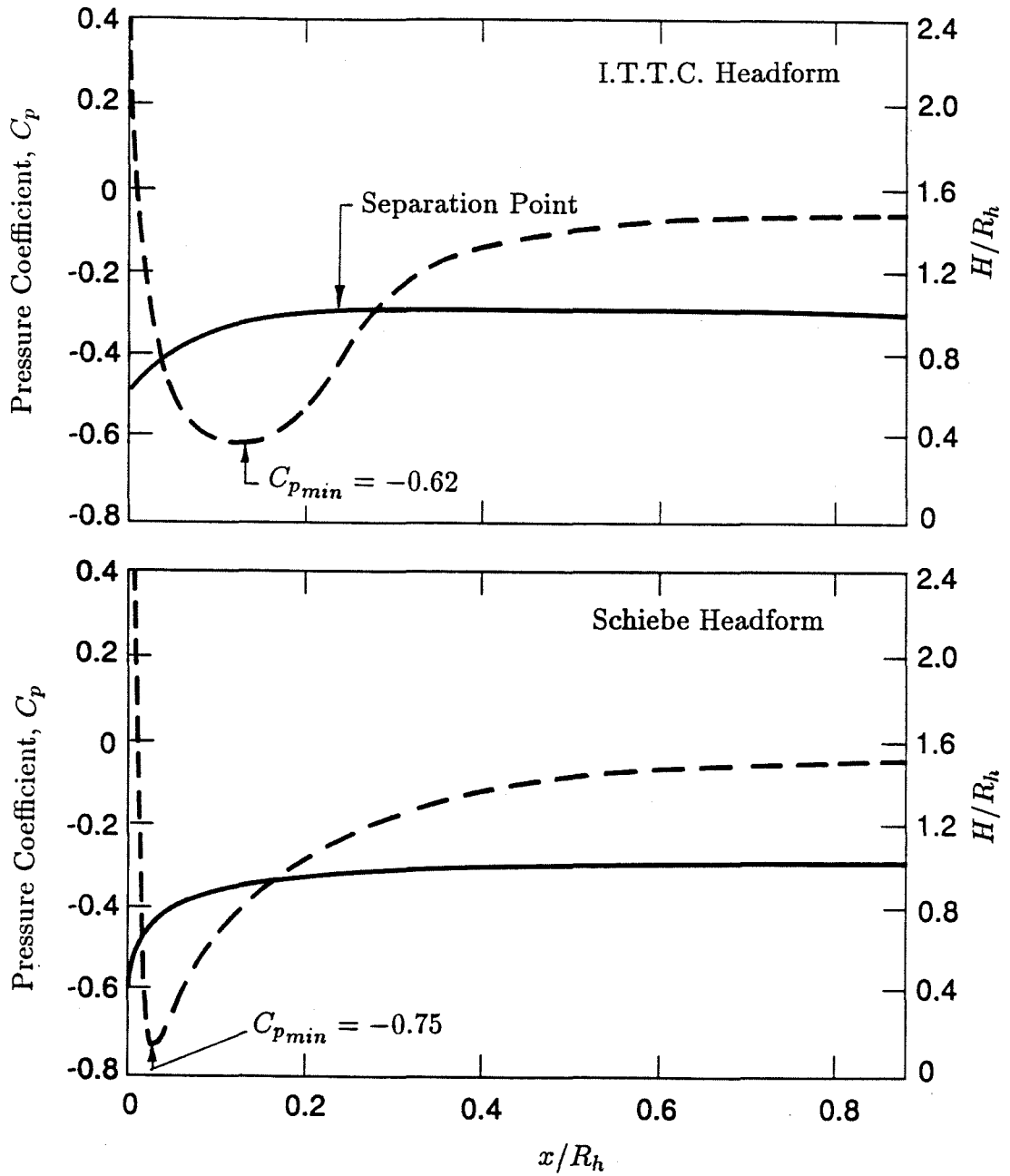


Figure 3.2: Pressure distributions on the (a) I.T.T.C. and (b) Schiebe headforms.

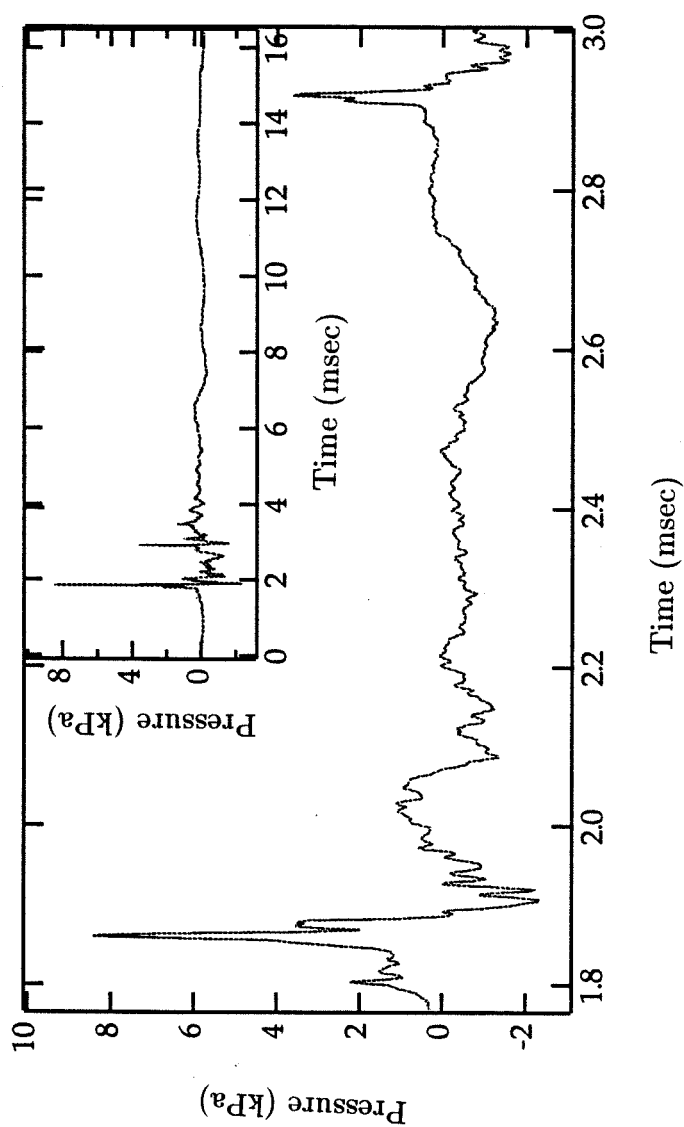


Figure 3.3: A typical amplified and filtered signal for a single cavitation event illustrating multiple peaks and a rebound. Inset shows the complete acoustic trace.

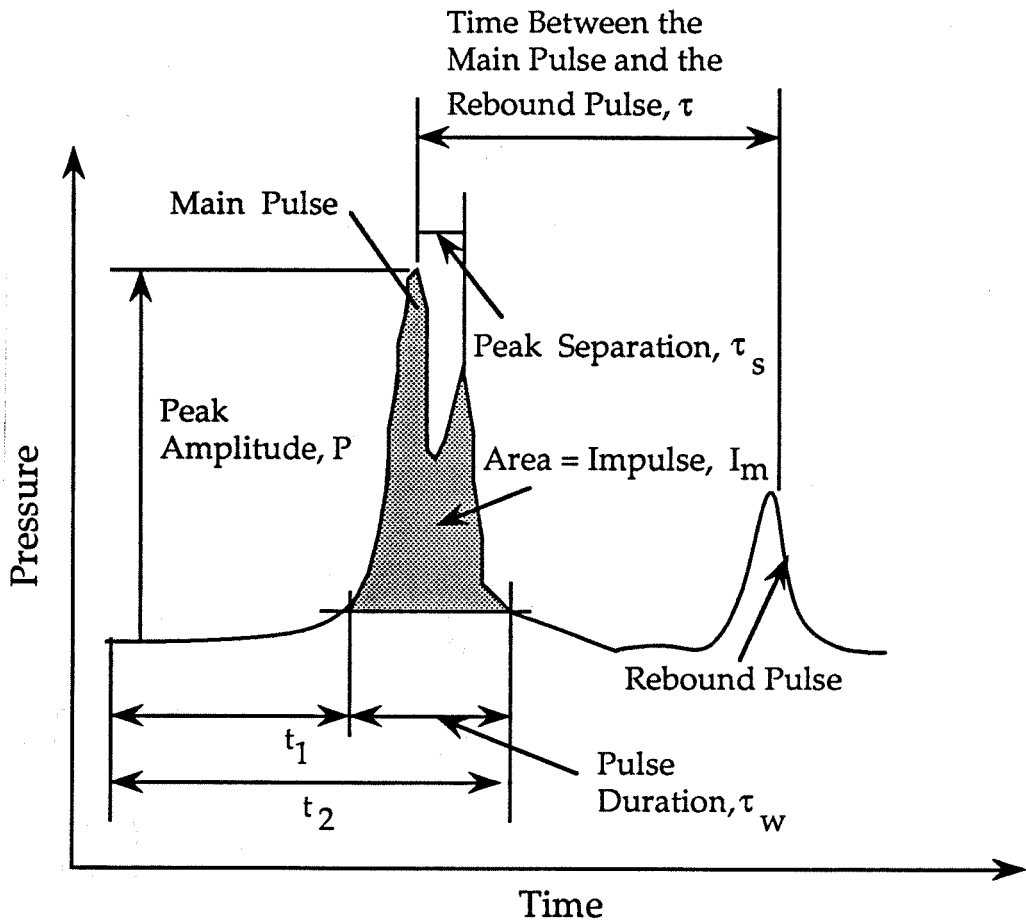


Figure 3.4: Sketch of a typical acoustic trace with the definitions of some measured quantities.

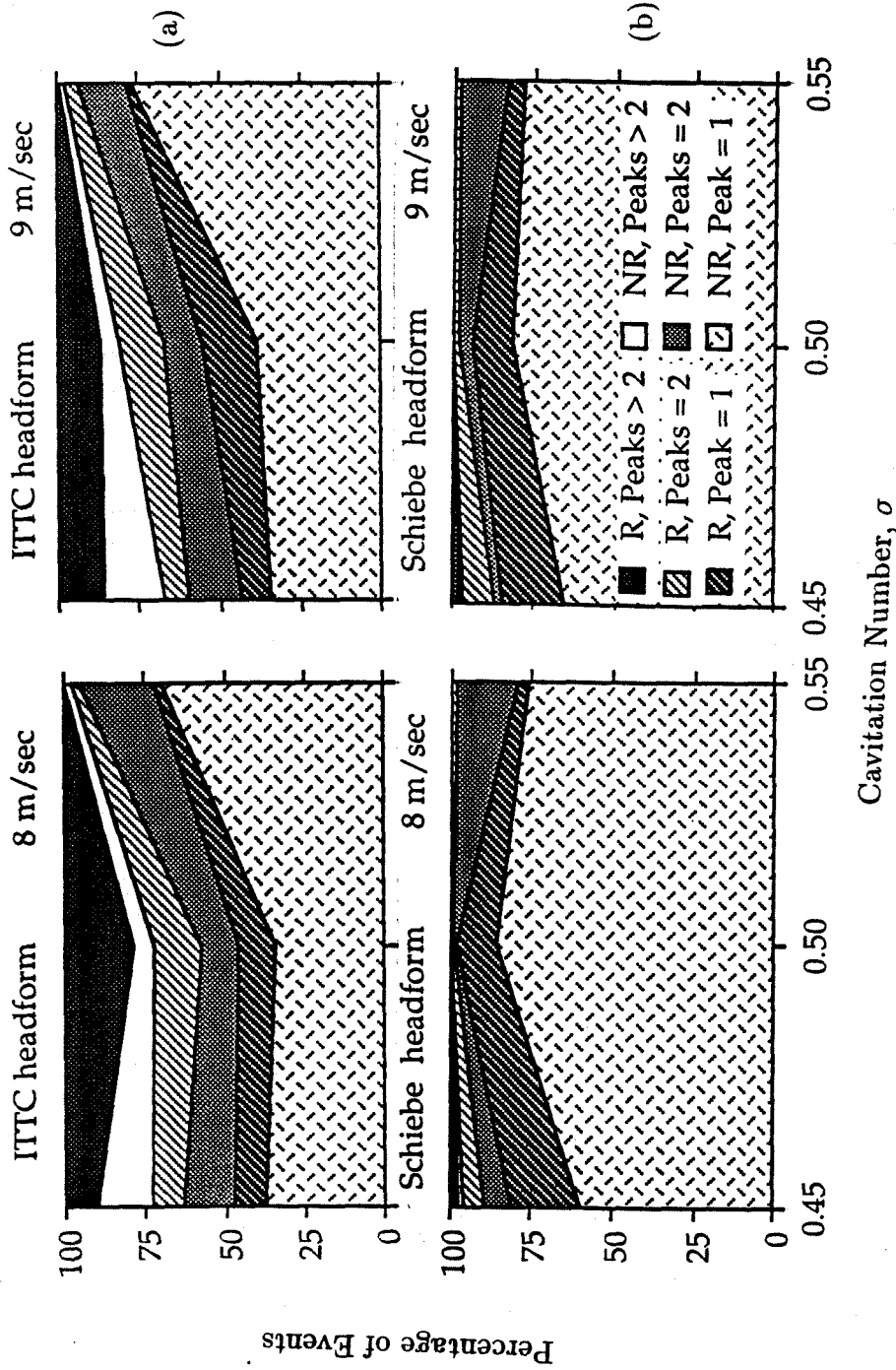


Figure 3.5: Probabilities of different types of cavitation events on the (a) I.T.T.C. headform and (b) Schiebe headform indicating the occurrence of multiple peaks or a rebound. R and NR respectively denote events with and without rebound. The number alongside indicates the number of peaks in the main pulse.

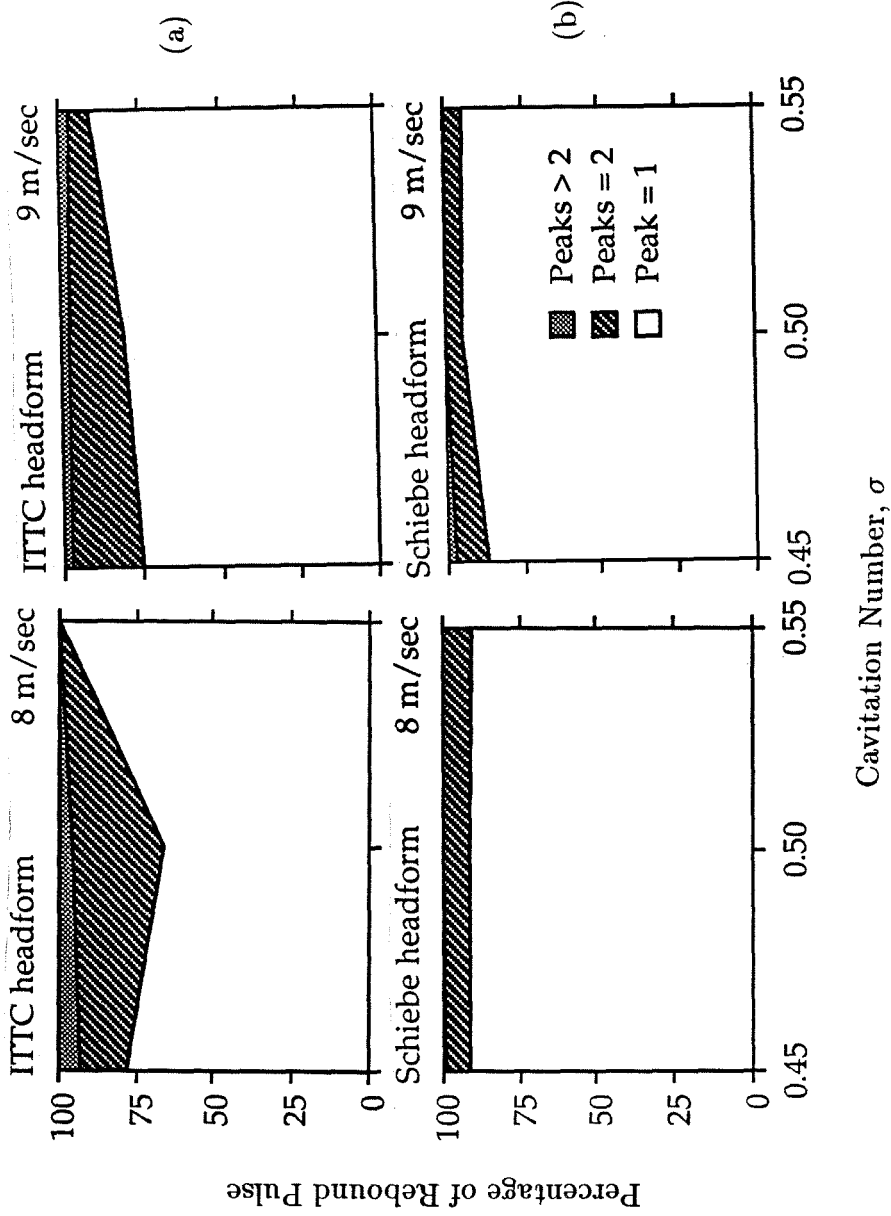


Figure 3.6: Probabilities of different number of peaks in the rebound pulse for cavitation events on the (a) I.T.T.C. headform and (b) Schiebe headform. The legend indicates number of peaks in the rebound pulse.

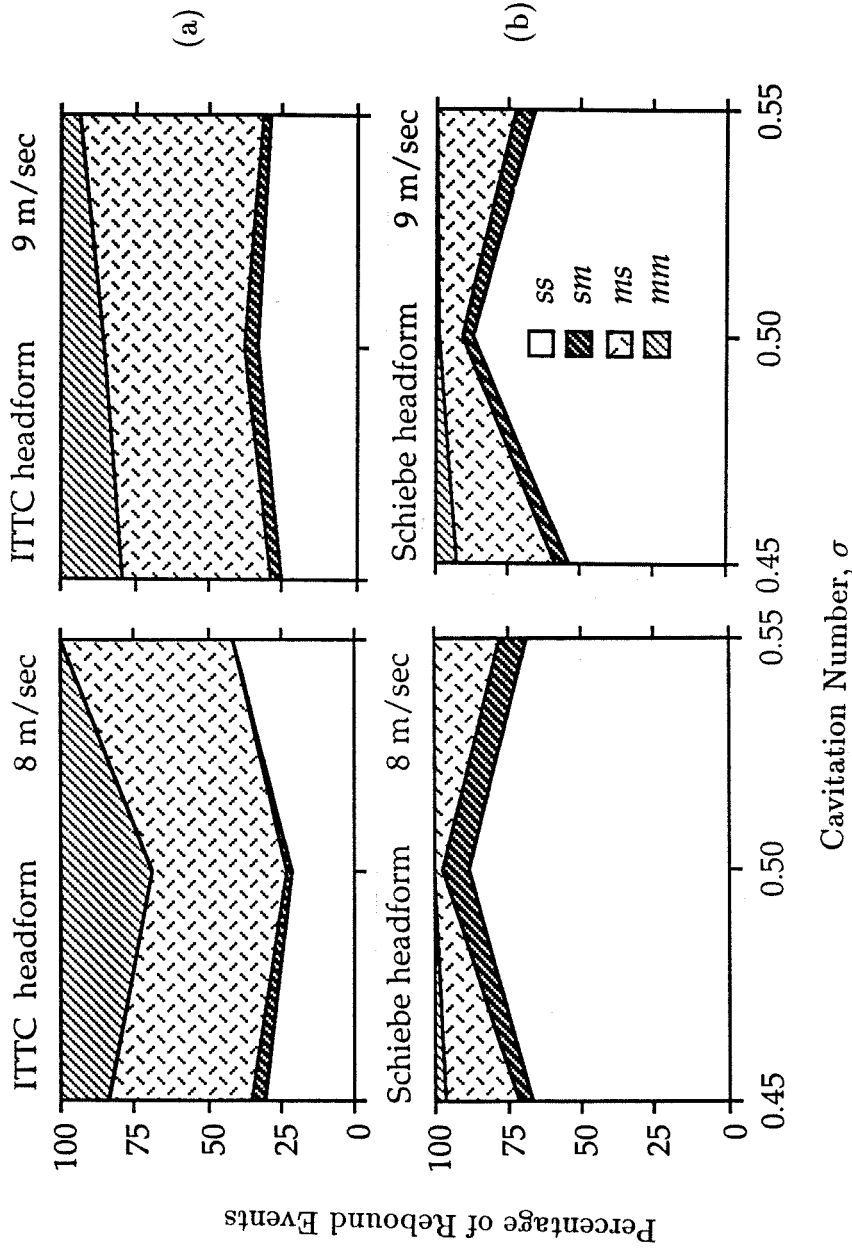


Figure 3.7: Probabilities of different types of cavitation events with rebound for the (a) I.T.T.C. headform and (b) Schiebe headform. A two-letter symbol is used to classify the event with the first letter indicating the number of peaks in the main pulse and the second letter, the number of peaks in the rebound pulse; *s* indicates single peak and *m* indicates more than one peak.

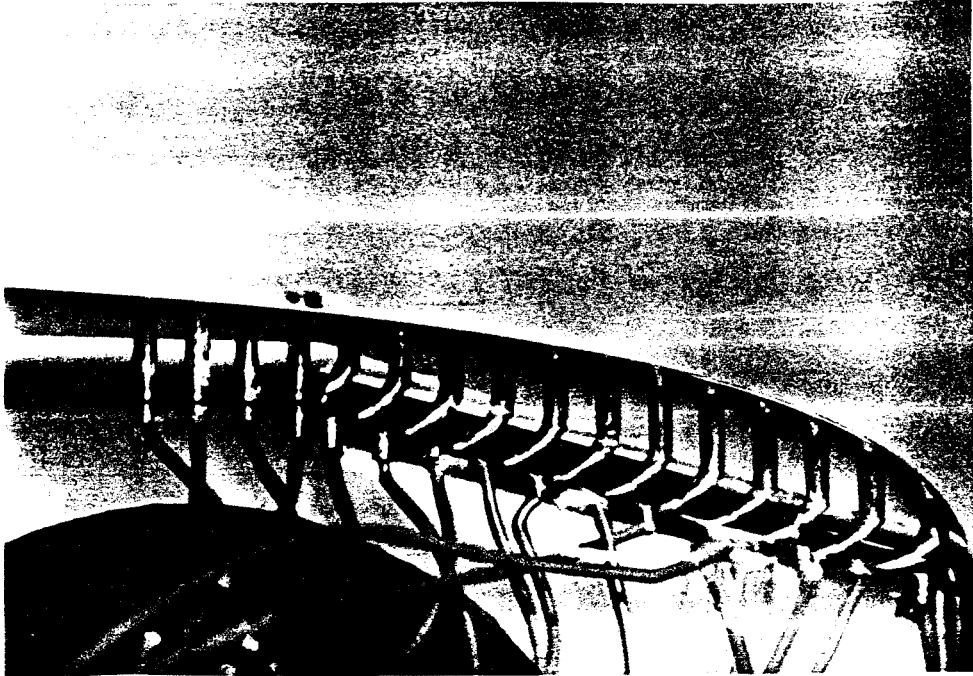


Figure 3.8: A typical photograph from Ceccio and Brennen (1991) illustrating the bubble breaking up into two or more pieces during the collapse.

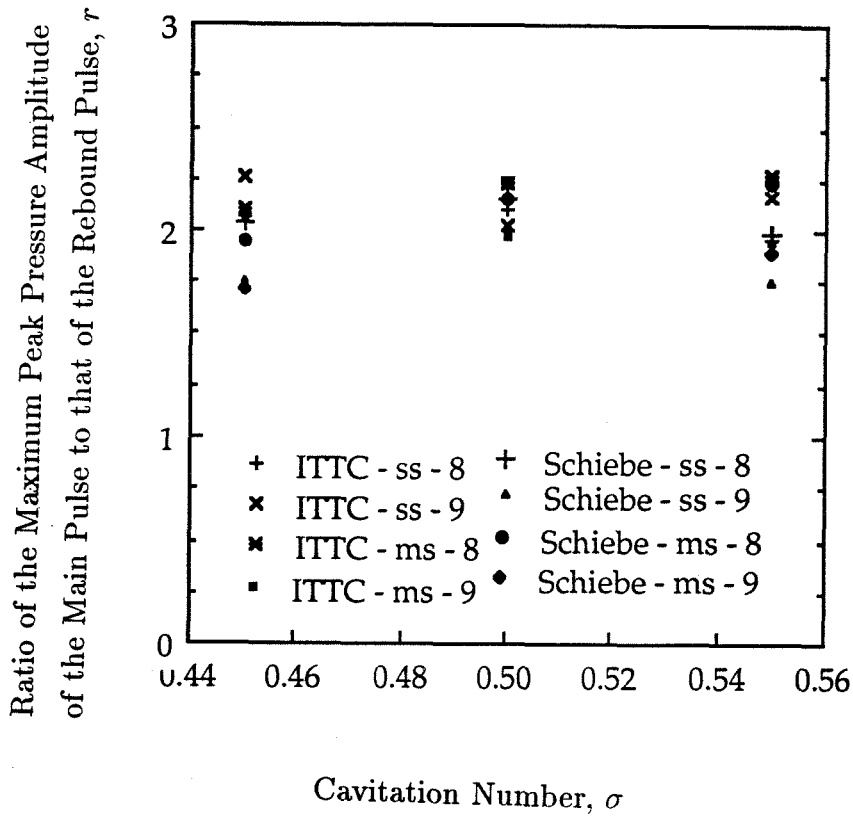


Figure 3.9: Ratio of the peak pressure amplitude of the main pulse to peak pressure amplitude of the rebound pulse, r , as a function of the cavitation number. The legend indicates the headform, the type of event and the flow velocity.

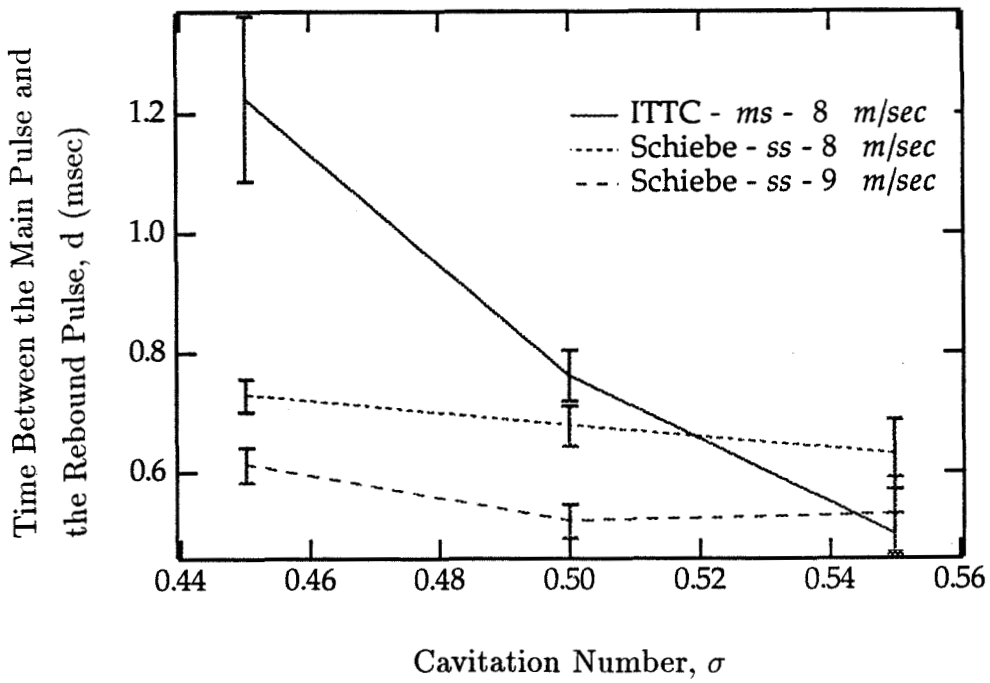


Figure 3.10: Variation of the time between the main pulse and the rebound pulse as a function of the cavitation number. The legend indicates the headform, the type of event and the flow velocity.

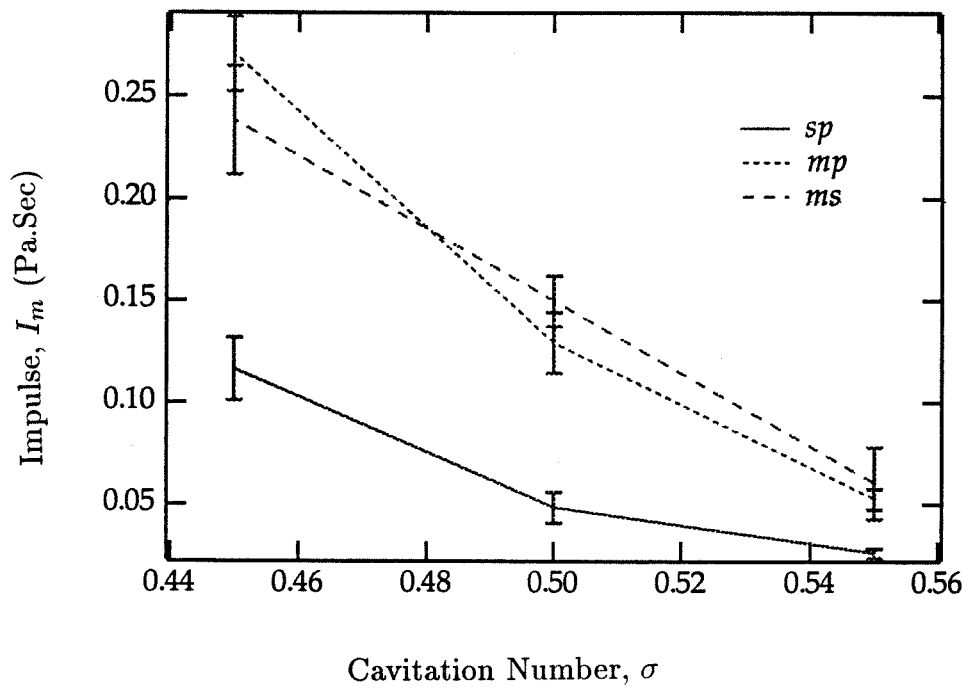


Figure 3.11: The figure illustrates the dependence of the acoustic impulse, I_m , on the type of event for the I.T.T.C. headform. The flow velocity is 8 m/sec.

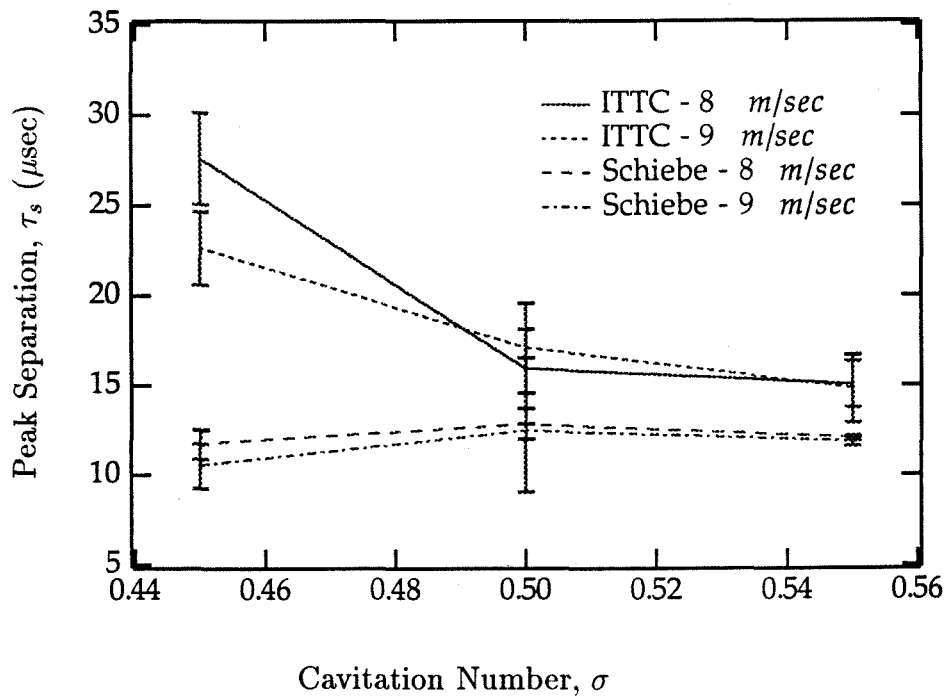


Figure 3.12: The peak separation, τ_s , as a function of the flow velocity for each headform. The legend indicates the type of headform and the flow velocity.

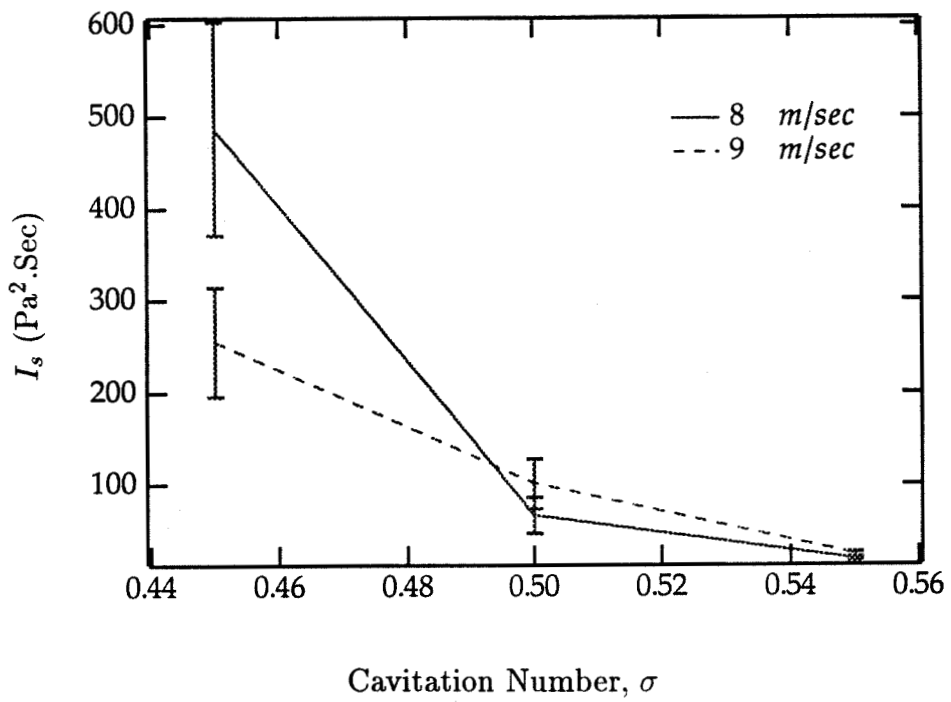


Figure 3.13: The figure illustrates the dependence of I_s on the flow velocity for sp -type event on the I.T.T.C. headform.

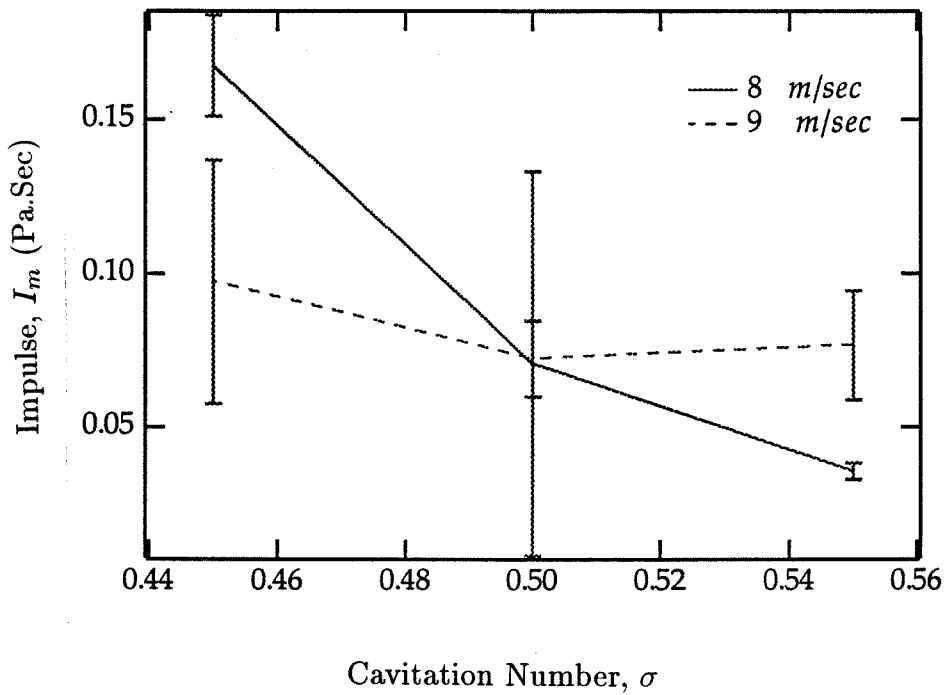


Figure 3.14: The figure illustrates the dependence of the acoustic impulse, I_m , on the flow velocity for mp -type events on the Schiebe headform.

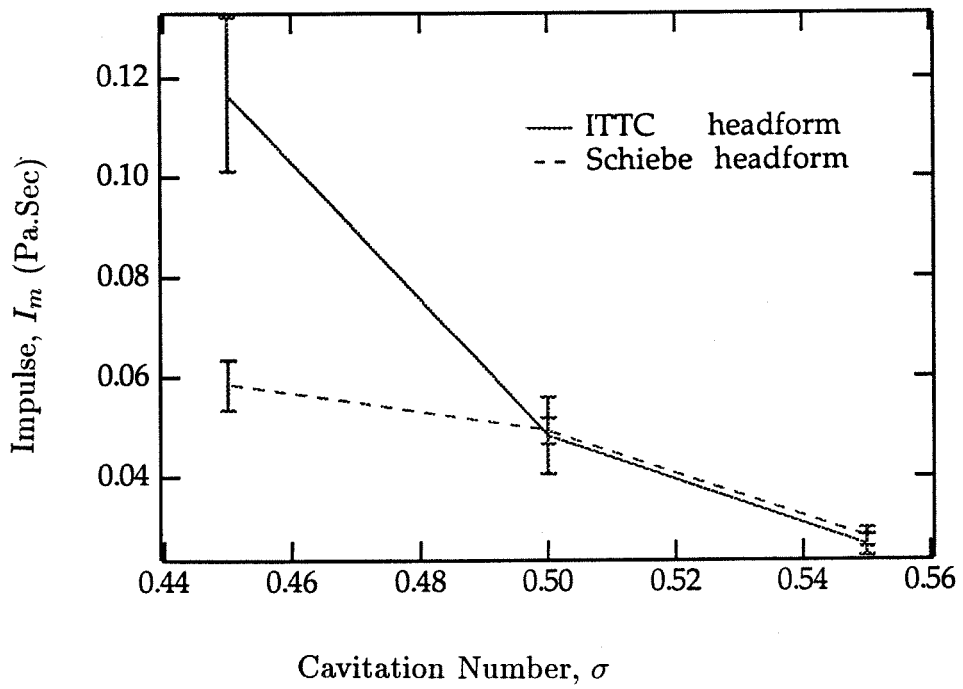


Figure 3.15: The figure illustrates the variation of the acoustic impulse, I_m , with the type of headform for sp -type of events. The flow velocity is 8 m/sec.

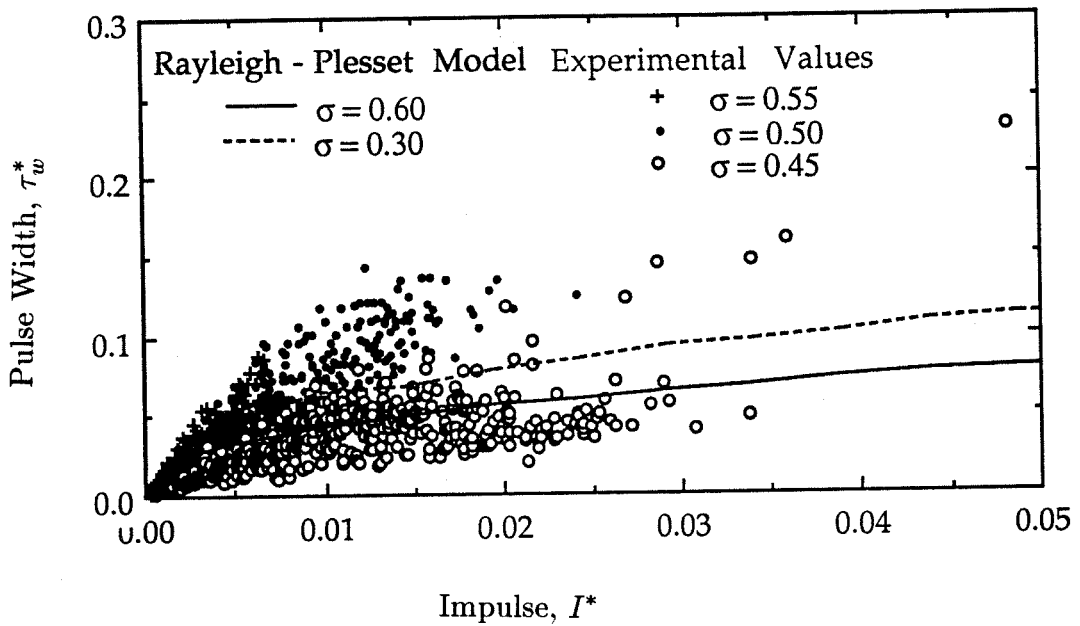


Figure 3.16: Experimentally obtained values of the nondimensional pulse width, τ_w^* , plotted against the nondimensional impulse, I^* , and compared with the values from the numerical integration of the Rayleigh-Plesset equation. The data for the I.T.T.C. headform and different cavitation numbers. The flow velocity is 8 *m/sec*.

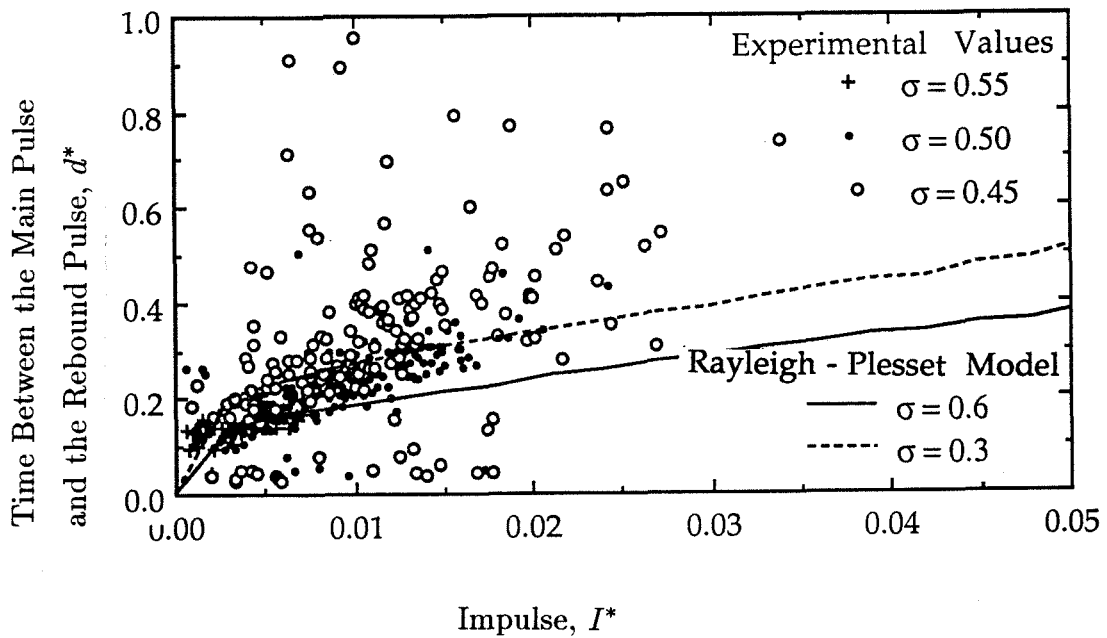


Figure 3.17: Experimentally obtained values of the nondimensional time between the main pulse and the rebound pulse, d^* , plotted against the nondimensional impulse, I^* , and compared with the values from the numerical integration of the Rayleigh-Plesset equation. The data for the I.T.T.C. headform and different cavitation numbers. The flow velocity is 8 *m/sec*.

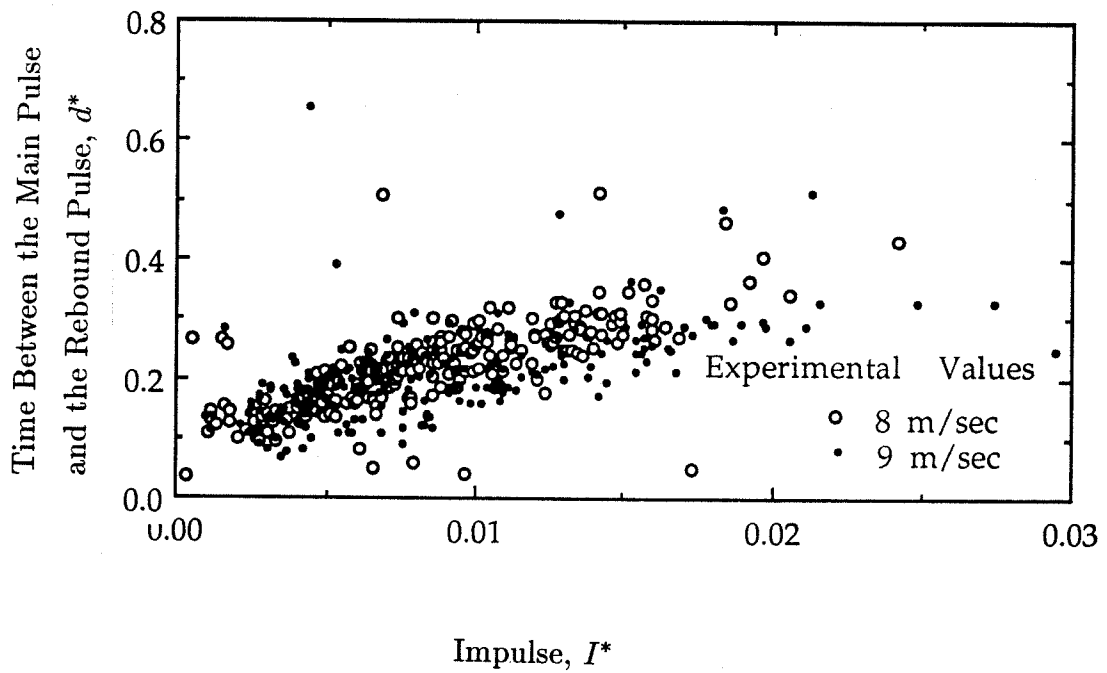


Figure 3.18: Experimentally obtained values of the nondimensional time between the main pulse and the rebound pulse, d^* , plotted against the nondimensional impulse, I^* . The data for the I.T.T.C. headform, different flow velocities and cavitation number of 0.50.

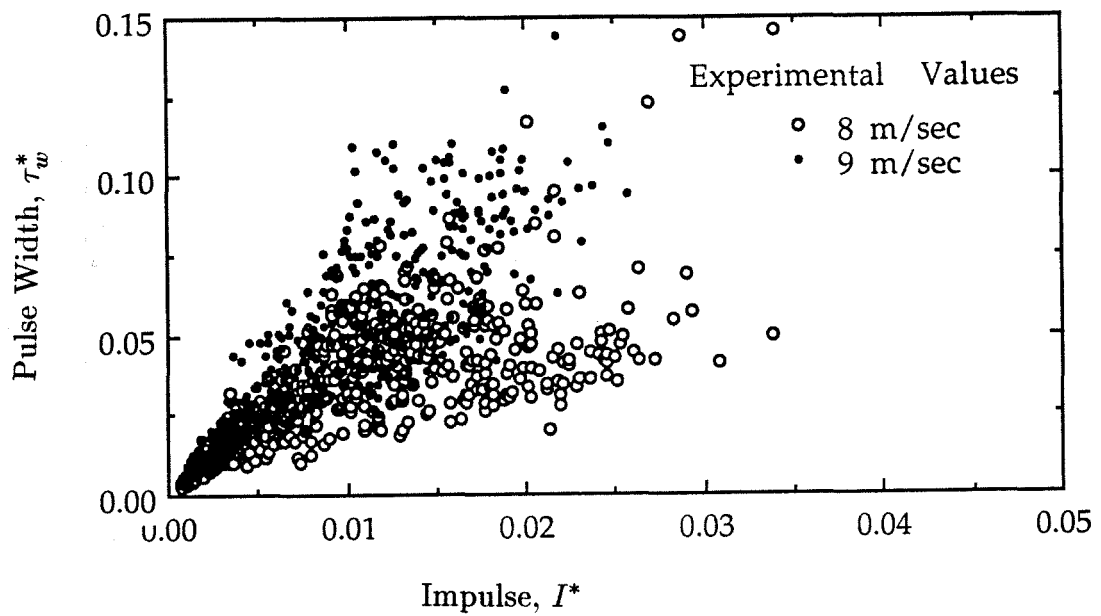


Figure 3.19: Experimentally obtained values of the nondimensional pulse width, τ_w^* , plotted against the nondimensional impulse, I^* . The data for the I.T.T.C. headform, different flow velocities and cavitation number of 0.45.

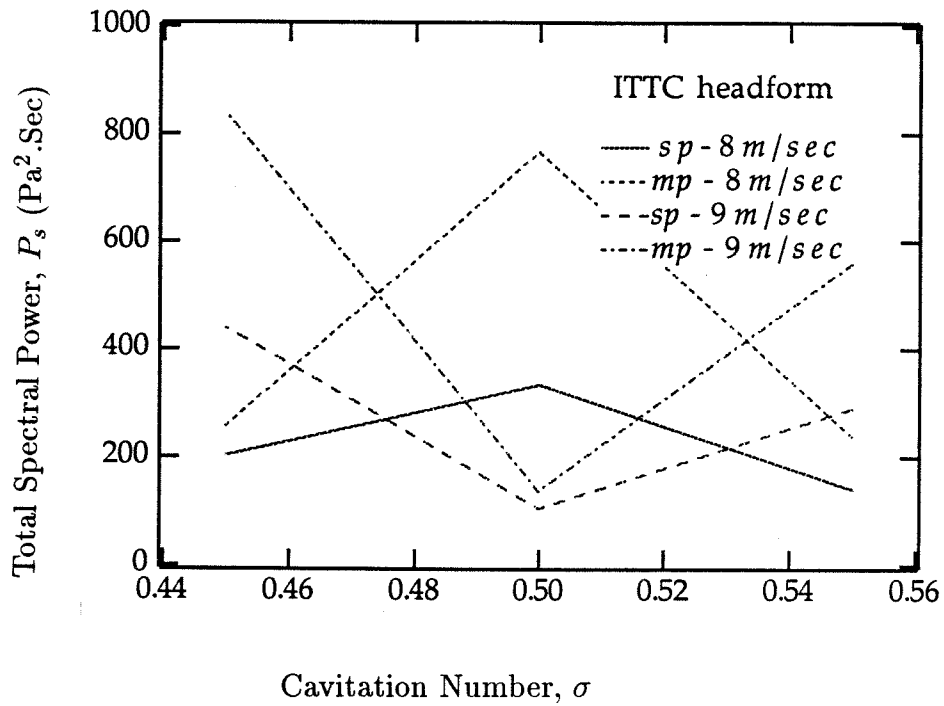


Figure 3.20: The total spectral power, P_s , plotted against the cavitation number for different types of events and the flow velocities. Data for the I.T.T.C. headform.

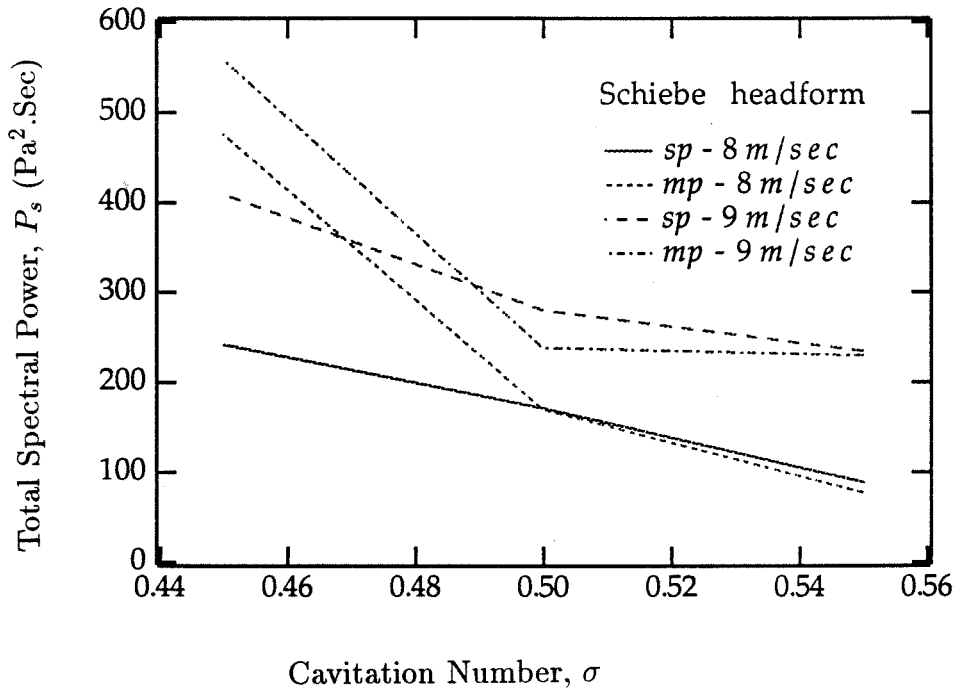


Figure 3.21: The total spectral power, P_s , plotted against the cavitation number for different types of events and the flow velocities. Data for the Schiebe headform.

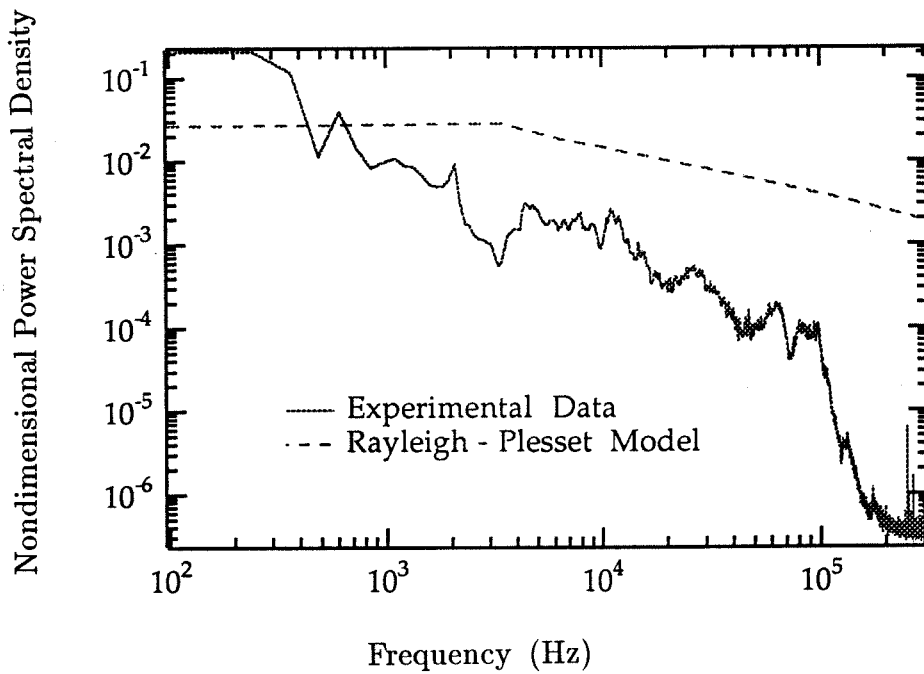


Figure 3.22: Typical nondimensional power spectral density obtained from the experimental data for the Schiebe headform at $\sigma = 0.45$ and flow velocity of 9 *m/sec*. The superimposed spectrum is from the numerical calculations using the Rayleigh-Plesset equation for a 100 μm nucleus at the water tunnel conditions.

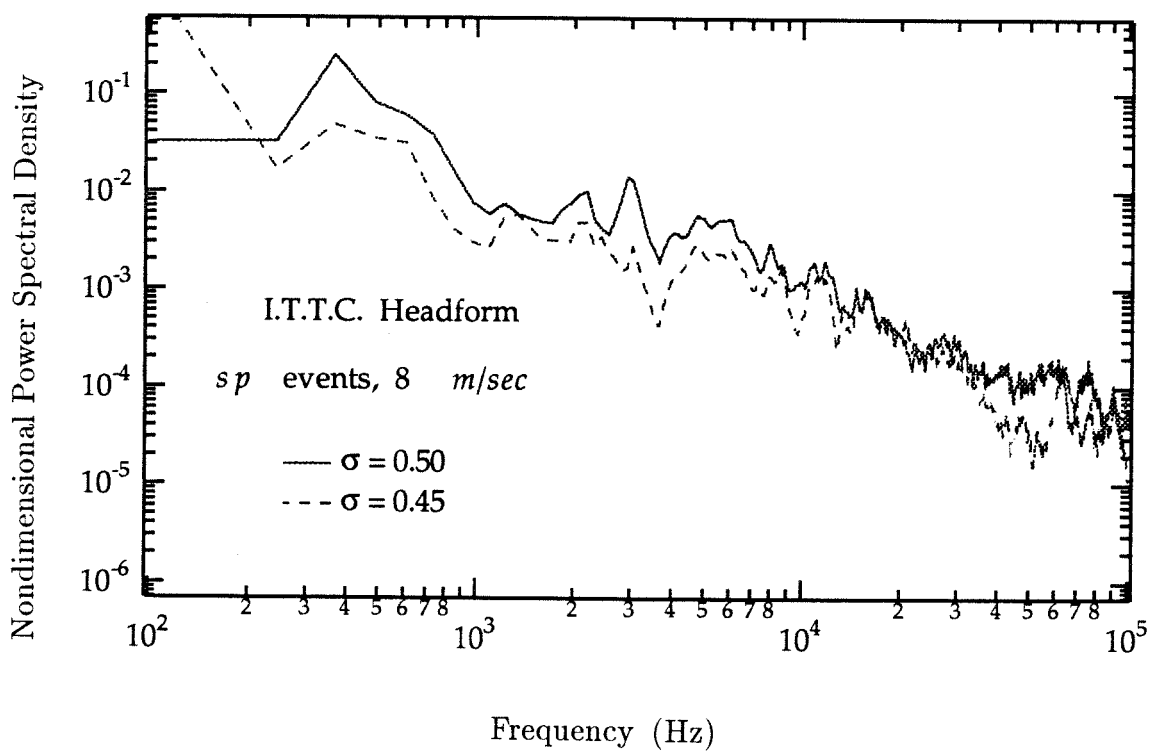


Figure 3.23: Effect of reduction in the cavitation number on the nondimensional power spectral density. Experimental data for *sp*-type events on the I.T.T.C. headform and flow velocity of 8 *m/sec*.

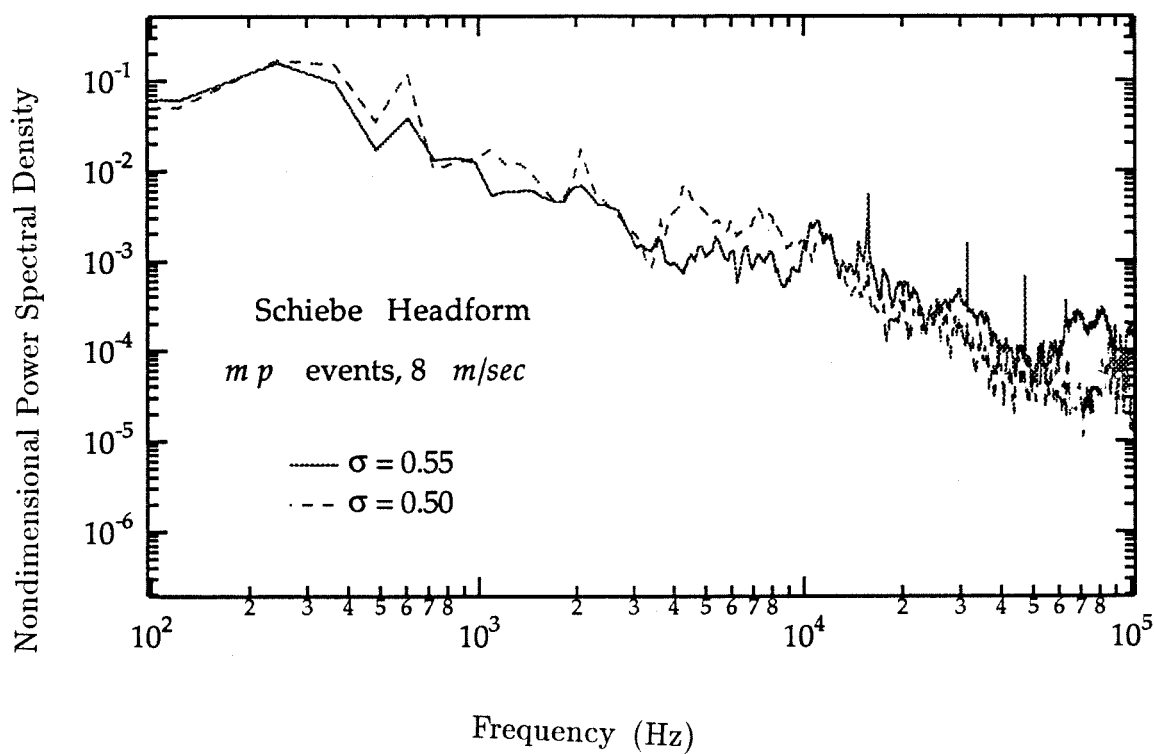


Figure 3.24: Effect of reduction in the cavitation number on the nondimensional power spectral density. Experimental data for *mp*-type events on the Schiebe headform and flow velocity of 8 *m/sec*.

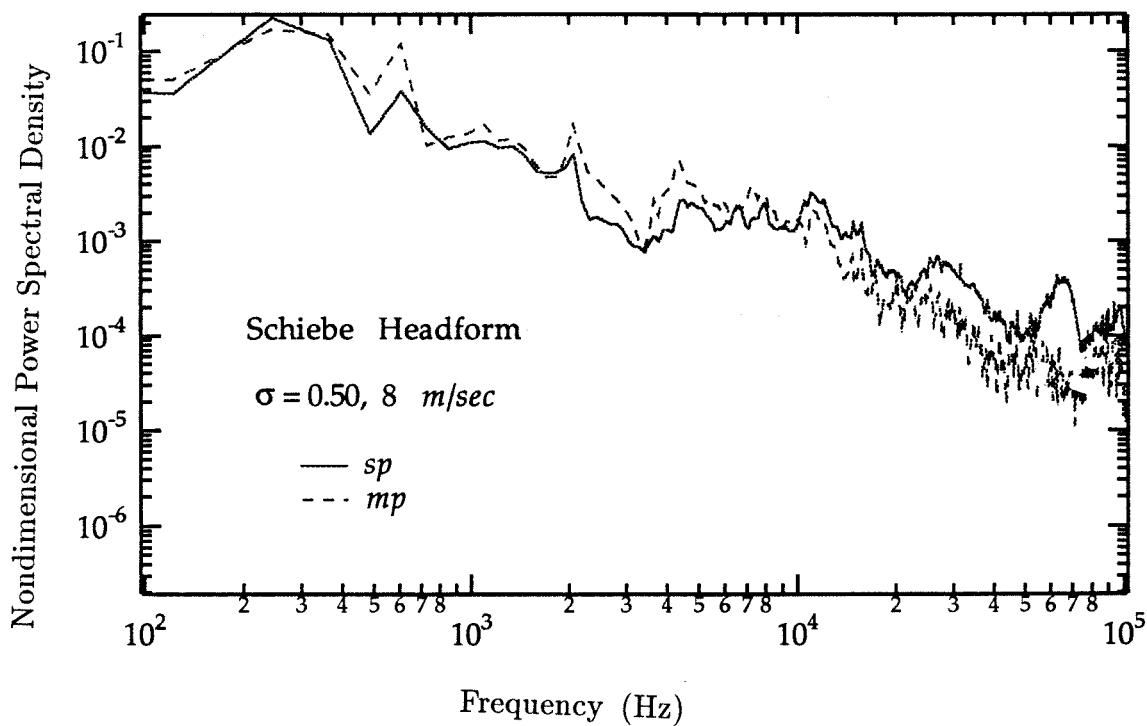


Figure 3.25: Effect of multipeaking on the nondimensional power spectral density. Experimental data for the Schiebe headform at $\sigma = 0.50$ and flow velocity of 8 m/sec .

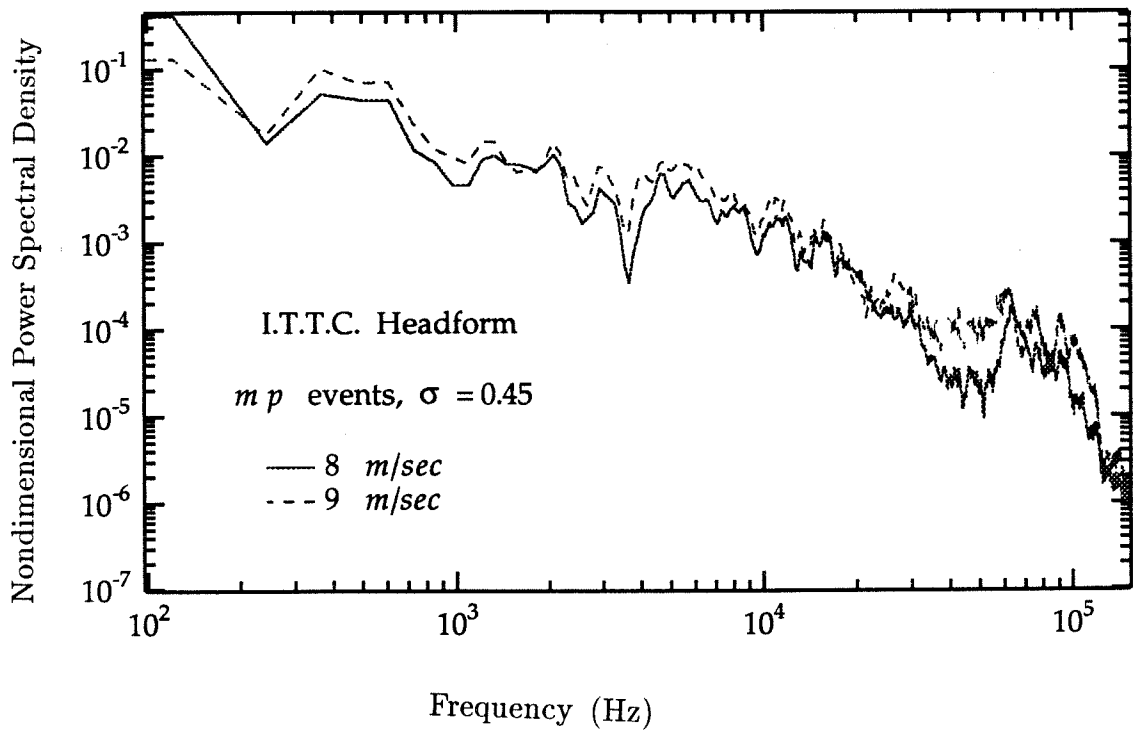


Figure 3.26: Effect of flow velocity on the nondimensional power spectral density. Experimental data for mp -type events on the I.T.T.C. headform at $\sigma = 0.45$.

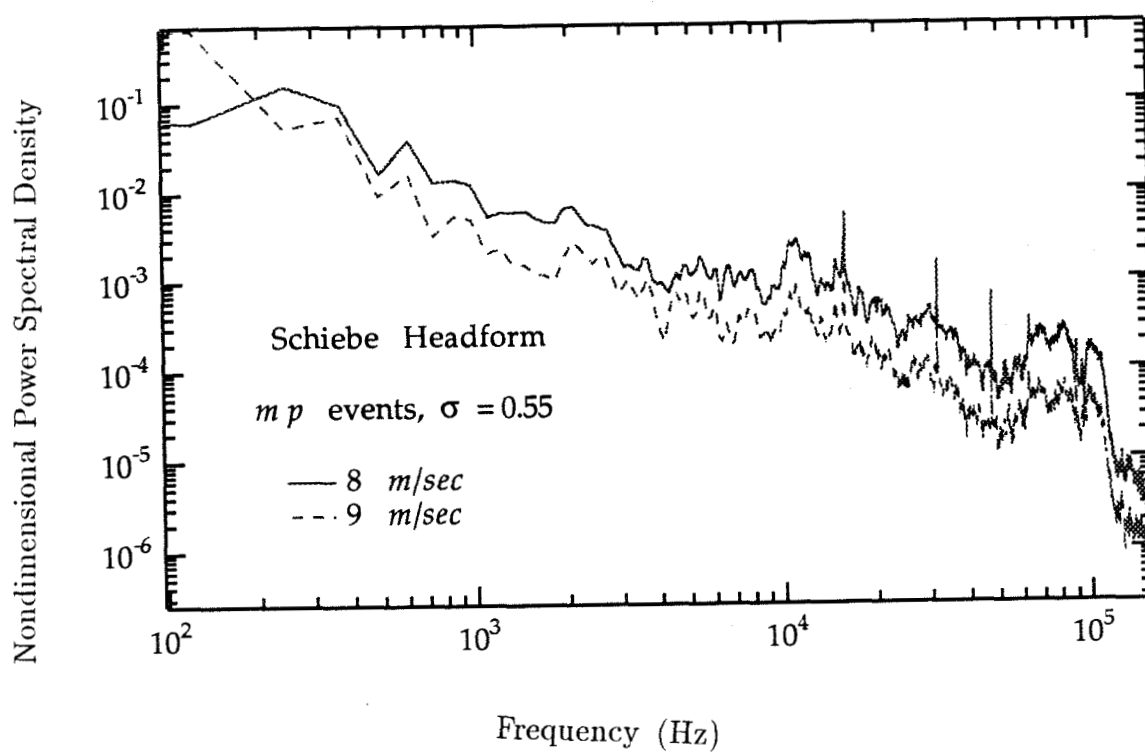


Figure 3.27: Effect of flow velocity on the nondimensional power spectral density. Experimental data for mp -type events on the Schiebe headform at $\sigma = 0.55$.

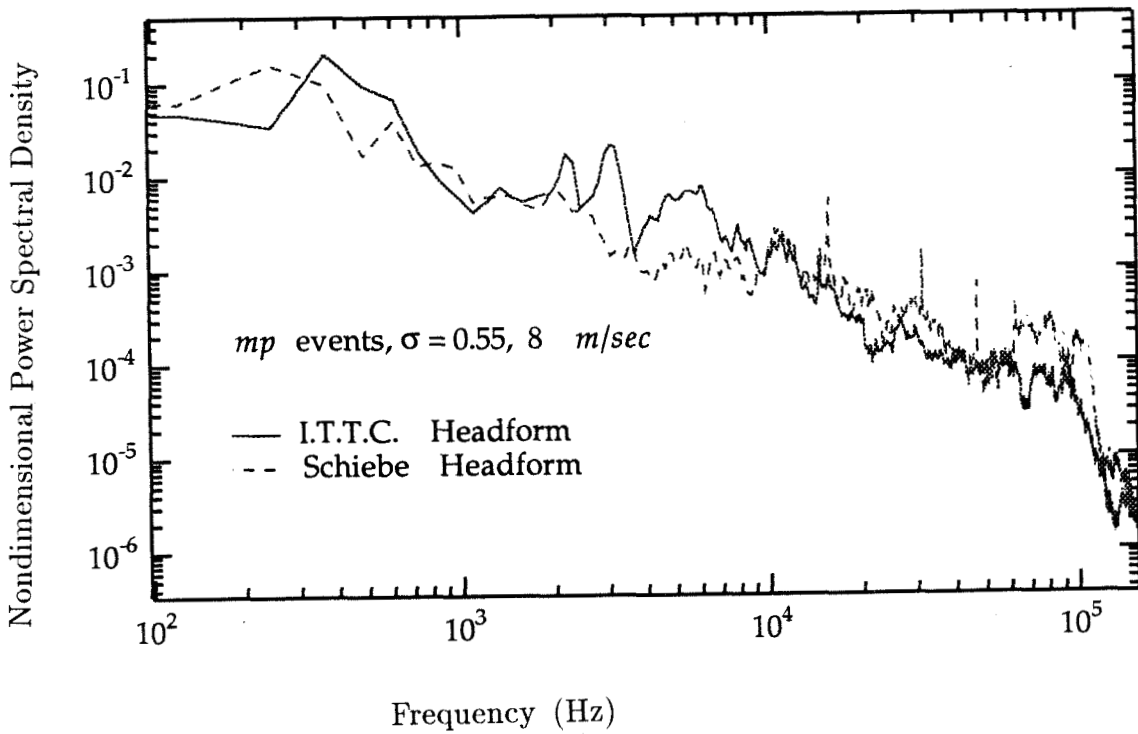


Figure 3.28: Comparison of the nondimensional power spectral density for the I.T.T.C. and the Schiebe headforms. Experimental data for *mp*-type events, flow velocity of 8 m/sec and cavitation number of 0.55.

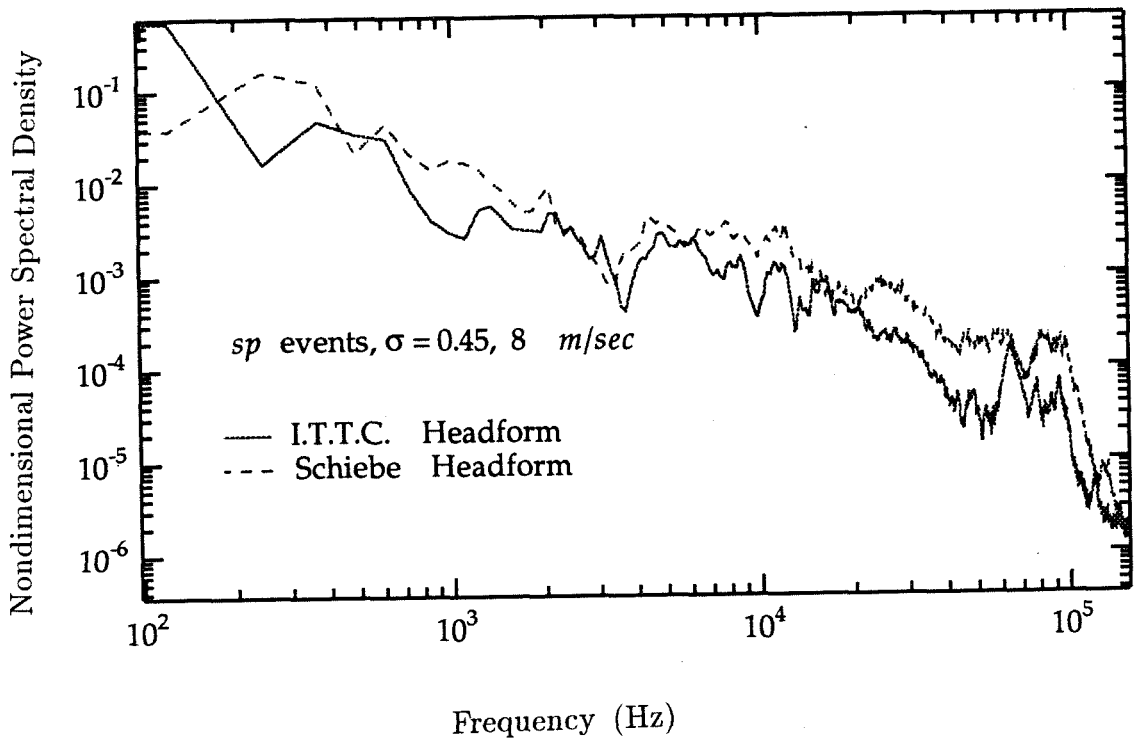


Figure 3.29: Comparison of the nondimensional power spectral density for the I.T.T.C. and the Schiebe headforms. Experimental data for *sp*-type events, flow velocity of 8 m/sec and cavitation number of 0.45.

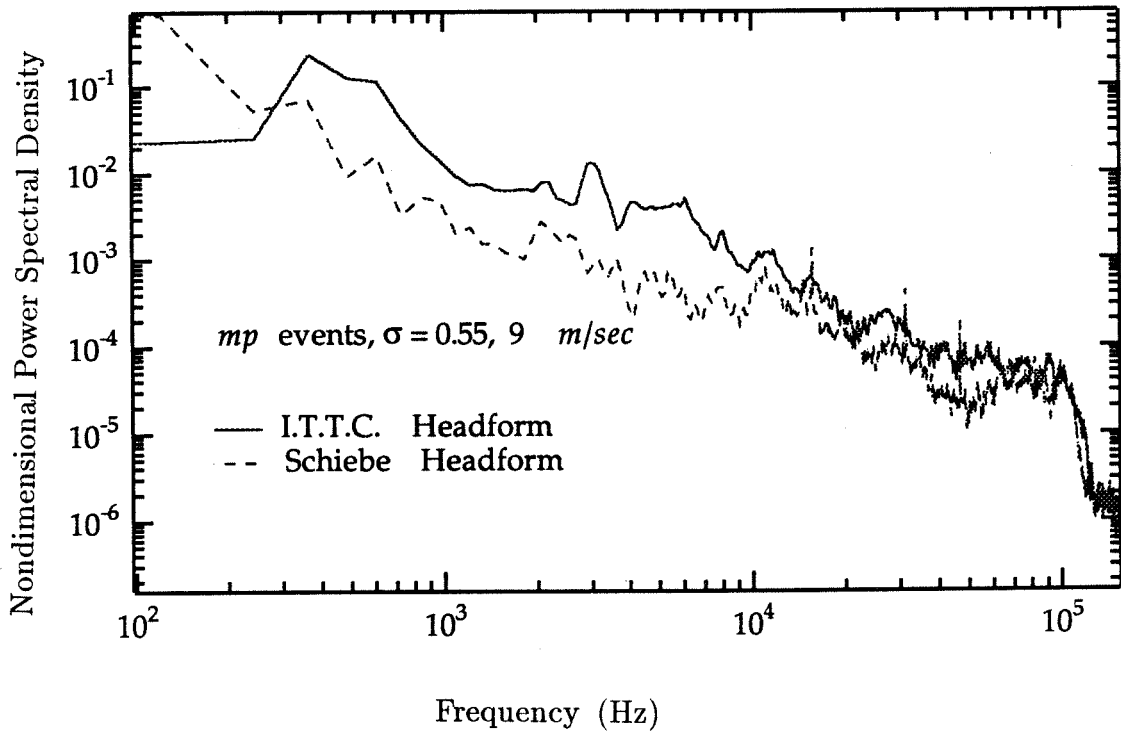


Figure 3.30: Comparison of the nondimensional power spectral density for the I.T.T.C. and the Schiebe headforms. Experimental data for *mp*-type events, flow velocity of 9 m/sec and cavitation number of 0.55.

Chapter 4

CONCLUSIONS

Two different aspects of cavitation noise have been investigated in the present work. The nonlinear interactive effects in bubbly mixtures have been theoretically modeled in the first part and the collapse process of a bubble in travelling bubble cavitation has been acoustically studied in the second part.

The nonlinear interactive effects in flows of bubbly mixtures have been studied by modeling the frequency response of a bubble layer next to a wall oscillating normal to itself. The response of the layer has been calculated in terms of the amplitude of pressure and radius oscillation in the bubbly mixture. The conclusions are summarized below:

- The presence of a finite length scale such as finite thickness of the bubble layer results in characteristic natural frequencies of the layer (called cloud natural frequencies), all of which are less than the linearized natural frequency of a single bubble, ω_b . The cloud natural frequencies are determined by the void fraction, the ratio of layer thickness to the bubble radius and the linearized natural frequency of a single bubble in the layer.
- The excitation at the lowest cloud natural frequency generates strongest response in the layer. The response of the layer is dominated by the fundamental and the second harmonic components. Since the amplitude of the second harmonic is significant, not all of the high frequency response is damped out.
- The amplitude of the response is increased by the proximity of lowest cloud natural frequency to $0.5\omega_b$.
- The amplitude of different harmonic components of the pressure and the radius oscillation form standing wave patterns in the layer

for excitation frequencies in *sub-resonant* and *trans-resonant* regimes ($\omega_f < \omega_b$). The amplitude of the standing wave decays slowly with distance from the wall.

- The response decays rapidly with distance from the source of excitation for excitation frequencies in the *super-resonant* regime.
- The phenomenon of *harmonic cascading* is seen to take place in a bubbly mixture containing bubbles of different sizes. In this case, the excitation at a frequency, ω_f , results in strong response at a frequency $2\omega_f$ because of presence of a large number of bubbles with a natural frequency of $2\omega_f$ in the layer. The phenomena of *harmonic cascading* can be modeled only by a nonlinear model.
- Smaller void fraction, reduced viscous and surface tension effects and larger amplitude of excitation promote stronger response in the layer.

Conclusions from the acoustical study of bubble collapse in travelling bubble cavitation around axisymmetric headforms are summarized below:

- The bubbles collapse and sometimes rebound and collapse again, resulting in up to two pulses in the acoustic signal generated from collapse of a single bubble. Each of the pulses may contain more than one peak - a phenomenon referred to as multi-peaking.
- Both multi-peaking and rebounding increase with reduction in the cavitation number for I.T.T.C. headform. However, multi-peaking decreases and rebounding increases with reduction in the cavitation number for the Schiebe headform
- A change in flow velocity does not influence the occurrence of multi-peaking and rebounding.

- The peak amplitude of the acoustic pulse from the first collapse is always twice as large the peak amplitude of the second collapse. This suggests a definite mechanism of bubble fission before the rebound.
- Smaller cavitation number, smaller flow velocity and multipeaking delay the rebound.
- The characteristic measures of the acoustic signal such as the peak amplitude and acoustic impulse increased with reduction in the cavitation number. The pulse width exhibited a maximum for the intermediate value of the cavitation number.
- The peak separation was found to be fairly constant at about $12 \mu s$ for the Schiebe headform but increased from $15 \mu s$ to $23\text{--}28 \mu s$ with reduction in the cavitation number for the I.T.T.C. headform.
- The characteristic measures of the acoustic signal have larger value at smaller flow velocity at the cavitation number of 0.45. This inequality is reversed at larger cavitation numbers.
- The characteristic measures of the acoustic signal have larger value for the I.T.T.C. headform than for the Schiebe headform at the cavitation number of 0.45. This inequality disappears at larger cavitation numbers.
- A theoretical model based on the Rayleigh–Plesset equation is seen to predict the right order of magnitude for the characteristic measures of the acoustic signal but does not properly predict the dependence of pulse width on cavitation number. The model does not predict the distribution of spectral energy in noise emitted very well.
- The fraction of spectral energy contained in high frequencies ($30 \text{ kHz}\text{--}80 \text{ kHz}$) is reduced significantly with decrease in the cavitation

number in some cases. In the case of the I.T.T.C. headform, this reduction appears correlated to the increase in *effective width* of the acoustic signal represented by the peak separation.

- Multipeaking does not appear to influence the distribution of spectral energy for the I.T.T.C. headform. In case of the Schiebe headform, the fraction of spectral energy contained between 50kHz and 75kHz is significantly reduced as a result of multipeaking. This may be caused by increase in *effective width* of the acoustic pulse that is due to multipeaking.
- In the case of the I.T.T.C. headform, the fraction of spectral energy in the high frequency range is significantly increased by an increase in flow velocity. However, in the case of the Schiebe headform, the fraction of spectral energy contained in the low frequency range increases with increase in flow velocity.

Clearly, many of the observations from the acoustical study of bubble collapse are not well understood in terms of physical mechanisms in bubble collapse. However, these observations may be used in a statistical model (Baiter(1986)) for description of the single bubble cavitation noise. The results from modeling of the nonlinear effects in bubbly mixtures when combined with a statistical description obtained from acoustical study of single bubble cavitation noise may be used to describe qualitatively the noise generated by bubbly mixtures.

An acoustical study to characterize the effect of various factors such as Reynolds number, length scales in the flow, nuclei number distribution and various flow structures is needed to obtain a complete picture of noise emission from bubble collapse. Additional data such as the cavitation event rate and bubble size information measured by Ceccio and Brennen (1991) need to be incorporated in such a study. A few high speed films taken along with the acoustic data can be

used to gain detailed understanding of the physical mechanisms in the collapse process of a single bubble, while a large number of acoustic traces can be gathered and analyzed to obtain a statistically meaningful picture of the noise emission by a collapsing bubble.

The nonlinear effects also need to be modeled differently to allow for large oscillations in bubble radius amplitude, which will give us a detailed and more realistic understanding of the interactive effects in bubble clouds.

REFERENCES

- Arakeri, V.H. and Shanmuganathan, V. 1985. *On the Evidence for the Effect of Bubble Interference on Cavitation Noise*. J. Fluid Mech., Vol. 159, pp. 130–150.
- Baiter, H. J. 1974. *Aspects of Cavitation Noise*. Symp. on High Powered Propulsion of Ships, Wageningen, The Netherlands, Publication No. 490, pp. 1–39.
- Baiter, H. J. 1986. *On Different Notions of Cavitation Noise and What They Imply*. Int. Symp. on Cavitation and Multiphase Flow Noise, ASME FED Vol. 45, pp. 107–118.
- Bendat, J.S. and Piersol, A.G. 1971. *Measurement and Analysis of Random Data*. John Wiley and Sons, New York, Chaps. 4, 5 and 6.
- Bendat, J.S. and Piersol, A. G. 1980. *Engineering Applications of Correlation and Spectral Analysis*. John Wiley and Sons, New York, Chap. 3.
- Biesheuvel A. and van Wijngaarden, L. 1984. *Two Phase Flow Equations for a Dilute Dispersions of Gas Bubbles in Liquid*. J. Fluid Mech., Vol. 148, pp. 301–318.
- Birnir, B. and Smereka, P. 1990. *Existence Theory and Invariant Manifolds of Bubble Clouds*. Comm. on Pure Appl. Math., John Wiley and Sons, New York, Vol XIII, pp. 363–413.
- Blake, J.R., Taib, B.B. and Doherty, G. 1986. *Transient Cavities Near Boundaries – Part 1. Rigid Boundary*. J. Fluid Mech., Vol. 170, pp. 479–497.
- Blake, W.K. 1986. *Propeller Cavitation Noise: The Problems of Scaling and Prediction*. Int. Symp. on Cav. and Multiphase Flow Noise, pp. 89–99.
- Blake, W. K., Wolpert, M. J. and Geib, F. E. 1977. *Cavitation Noise and Inception as Influenced by Boundary Layer Development on a Hydrofoil*. J. Fluid Mech., Vol.

80, pp. 617–640.

Brennen, C. E. and Ceccio, S. L. 1989. *Recent Observations on Cavitation and Cavitation Noise*. Proc. Third Int. Symp. on Cavitation Noise and Erosion in Fluid Systems, San Francisco, CA, Dec. 1989, pp. 67–78.

Brooke Benjamin, T. 1958. *Pressure Waves from Collapsing Cavities*. Second Symp. on Naval Hydrodynamics – Hydrodynamic Noise and Cavity Flow, ed. R.D. Cooper, pp. 207–233.

Ceccio, S.L. 1990. *Observations of the Dynamics and the Acoustic of Travelling Bubble Cavitation*. Ph. D. Thesis, Calif. Inst. of Tech., Pasadena, CA 91125.

Ceccio, S. L. and Brennen, C. E. 1991. *The Dynamics and Acoustics of Travelling Bubble Cavitation*. To appear in the J. Fluid Mech.

Chahine, G.L. 1982. *Pressure Field Generated by the Collective Collapse of Cavitation Bubbles*. IAHR symposium on Operating Problems of Pump Stations and Power Plants, Amsterdam, The Netherlands, Vol. 1 (2), pp. 1–12.

Chahine, G.L. 1983. *Cloud Cavitation : Theory*. 14th Symp. on Naval Hydrodynamics, National Academy Press, Washington, D.C., pp. 165–195.

d'Agostino, L. and Brennen, C.E. 1988a. *Linearized Dynamics of Spherical Bubble Clouds*. J. Fluid Mech., Vol. 199, pp. 155–176.

d'Agostino, L., Brennen, C.E. and Acosta, A.J. 1988b. *Linearized Dynamics of Two-Dimensional Bubbly and Cavitating Flows Over Slender Surfaces*. J. Fluid Mech., Vol. 192, pp 485–509.

Devin C. Jr. 1959. *Survey of Thermal, Radiation and Viscous Damping of Pulsating Air Bubbles in Water*. J. Acous. Soc. Am., Vol. 31 (12), pp 1654–1667.

Eller, A. and Flynn, H.G. 1969. *Generation of Subharmonics of Order One-Half*

- by *Bubbles in Sound Field*. J. Acous. Soc. Am., Vol. 46, No.3 (2), pp. 722–727.
- Ellis, A.T. 1952. *Observations on Cavitation Bubble Collapse*. Hydrodynamics Lab. Rep. No. 21–12, Calif. Inst. of Tech., Pasadena, CA 91125.
- Fitzpatrick, H. M. and Strasberg, M. 1956. *Hydrodynamic Sources of Sound*. First Symp. on Naval Hydrodynamics, Washington D. C., pp. 241–280.
- Flynn, H.G. 1964. *Physics of Acoustics Cavitation in Liquids*. Physical Acoustics – Principles and Methods, ed. W. P. Mason, Vol. 1, Part. B, Academic Press, New York, pp. 57–172.
- Gates, E. M. 1977. *The influence of Free Stream Turbulence, Free Stream Nuclei Populations and Drag Reducing Polymer on Cavitation Inception on Two Axisymmetric Bodies*. Rep. E182–2, Cal. Inst. of Tech., Div. of Engg. and Appl. Sci., Pasadena, CA 91125.
- Gates, E.M. and Acosta, A.J. 1978. *Some Effects of Several Free Stream Factors on Cavitation Inception on Axisymmetric Bodies*. 12th Symp. on Naval Hydrodynamics, Washington, D.C., pp. 86–108.
- Gates, E.M., Billet, M.L., Katz, J., Ooi, K.K., Holl, W. and Acosta A.J. 1979. *Cavitation Inception and Nuclei Distribution - Joint ARL-CIT Experiments*. Rep. E244-1, Calif. Inst. of Tech., Div. of Engg. and Appl. Sci., Pasadena, CA 91125.
- Gilmore, F.R. 1952. *The Growth and Collapse of a Spherical Bubble in a Viscous Compressible Liquid*. Hydrodynamics Laboratory Rep. No. 26 – 4, Calif. Inst. of Tech., Pasadena, CA 91125.
- Hamilton, M.F. 1981. *Travelling Bubble Cavitation and Resulting Noise*. Appl. Res. Lab., Penn. State, Tech. Mem. TM 81–76.
- Hamilton, M. F., Thompson, D. E. and Billet, M. L. 1982. *An Experimental Study of Travelling Bubble Cavitation and Noise*. ASME Int. Symp. on Cavitation Noise, pp. 25–33.

- Hansson, I., Kedrinskii, V. and Morch, K.A. 1982. *On the Dynamics of Cavity Clusters*. J. Phys., D: Appl. Phys., Vol. 15, pp. 1725–1734.
- Harrison, M. 1952. *An Experimental Study of Single Bubble Cavitation Noise*. J. Acous. Soc. Am., Vol.24 (6), pp. 776–782.
- Hoyt, J.W. 1966. *Wall Effect on the I.T.T.C. Standard Head Shape Pressure Distribution*. Contribution to 11th Int. Towing Tank Conf.
- Hsieh, D.Y. and Plesset, M.S. 1961. *Theory of Rectified Diffusion of Mass into Gas Bubbles*. J. Acous. Soc. Am., Vol. 33 (2), pp. 206–215.
- Illichev, V.I. and Lesunovskii, V.P. 1963. *On Noise Spectra Associated With Hydrodynamic Cavitation*. Sov. Phys. - Acous. Vol. 9 (1), pp. 25–28.
- Kimoto, H. 1987. *An Experimental Evaluation of the Effects of a Water Microjet and a Shock Wave by a Local Pressure Sensor*. Int. Symp. on Cavitation Research Facilities and Techniques, ASME FED Vol. 57, pp. 217–224.
- Knapp, R.T. and Hollander, A. 1948. *Laboratory Investigations of the Mechanisms of Cavitation*. Trans. ASME, July 1948, pp. 419–435.
- Lauterborn, W. 1976. *Numerical Investigation of Nonlinear Oscillations of Gas Bubbles in Liquids*. J. Acous. Soc. Am., Vol. 59 (2), pp. 283–293.
- Lauterborn, W. and Bolle, H. 1975. *Experimental Investigation of Cavitation Bubble Collapse in the Neighborhood of a Solid Boundary*. J. Fluid Mech., Vol. 72, pp. 391–399.
- Lindgren, H. and Johnsson, C.A. 1966. *Cavitation Inception on Headforms – I.T.T.C. Comparative Experiments*. 11th Int. Tank Towing. Conf., pp. 219–232.
- Maeda, M., Yamaguchi, H. and Kato, H. 1991. *Laser Holography Measurement of Bubble Population in Cavitation Cloud on a Foil Section*. presented in 1st ASME/JSME conference, Portland, Oregon, June 1991, FED Vol. 116, pp. 67–

75.

Marboe, M. L., Billet, M. L. and Thompson, D. E. 1986. *Some Aspects of Travelling Bubble Cavitation and Noise*. Int. Symp. on Cavitation and Multiphase Flow Noise, ASME, FED Vol. 45, pp. 119–126.

Mellen, R.H. 1954. *Ultrasonic Spectrum of Cavitation Noise in Water*. J. Acous. Soc. Am., Vol. 26 (3), pp. 356–360.

Mellen, R.H. 1956a. *An Experimental Study of the Collapse of Spherical Cavity in Water*. J. Acous. Soc. Am., Vol. 28, pp. 447–454.

Mellen, R.H. 1956b. *Spherical Pressure Waves of Finite Amplitude from Collapsing Cavities*. Underwater Sound Laboratory, Report No. 326.

Morch, K.A. 1980. *On the collapse of Cavity Clusters in Flow Cavitation*. In “Cavitation and Inhomogenieties in Underwater Acoustics”, Proceedings of the First International Conference, ed. W. Lauterborn, Springer-Verlag, New York, pp. 95–100.

Morch, K.A. 1982. *Energy considerations in the collapse of Cavity Clusters*. Appl. Sci. Res., Vol. 38, pp. 313–321.

Morozov, V. P. 1969. *Cavitation Noise as a Train of Pulses Generated at Random Times*. Sov. Phys. – Acous., Vol. 14 (3), pp. 361–365.

Neppiras, E.A. 1968. *Subharmonic and Other Low-Frequency Emission from Bubbles in Sound-Irradiated Liquids*. J. Acous. Soc. Am., Vol. 26, No.3 (2), pp. 587–601.

O’Hern, T.J., d’Agostino, L. and Acosta A.J. 1987. *Comparison of Holographic and Coulter Counter Measurements of Cavitation Nuclei in the Ocean*. Experimental and Theoretical Study on Cavitation Inception and Bubbly Flow Dynamics, Report No. Eng. 183.16, Div. of Engg. Appl. Sci., Calif. Inst. of Tech., Pasadena, CA 91125.

- Omta, R. 1987. *Oscillations of a Cloud of Bubbles of Small and Not So Small Amplitude*. J. Acoustical Soc. Am., Vol. 82, pp. 1018–1033.
- Parkin, B.R. 1952. *Scale Effects in Cavitating Flow*. Ph. D. Thesis, Calif. Inst. of Tech., Pasadena, CA 91125.
- Plesset, M.S. 1949. *The Dynamics of Cavitation Bubbles*. Trans. ASME, J. Appl. Mech., Sept. 1949, pp. 277–282.
- Plesset, M.S. and Hsieh, D.Y. 1960. *Theory of Gas Bubble Dynamics in Oscillating Pressure Fields*. Phys. of Fluids, Vol. 3 (6), pp. 882–892.
- Plesset, M.S. and Chapman, R.B. 1971. *Collapse of an Initially Spherical Cavity in Neighborhood of a Solid Boundary*. J. Fluid Mech., Vol.47 (2), pp. 283–290.
- Plesset, M.S. and Prosperetti, A. 1977. *Bubble Dynamics and Cavitation*. Ann. Rev. Fluid Mech., Vol. 9, pp. 145–185.
- Prosperetti, A. 1974. *Viscous and Nonlinear Effects in the Oscillations of Drops and Bubbles*. Ph. D. Thesis, Calif. Inst. of Tech., Pasadena, CA 91125.
- Prosperetti, A. 1977. *Application on Subharmonic Threshold to the Measurement of the Damping of Oscillating Gas Bubbles in Liquids*. J. Acous. Soc. Am., Vol. 61 (1), pp. 17–27.
- Rayleigh, Lord 1917. *On the Pressure Developed in a Liquid During the Collapse of Spherical Cavity*. Phil. Mag., Vol. 34, pp. 94–98.
- Schiebe, F.R. 1972. *Measurement of the Cavitation Susceptibility of Water Using Standard Bodies*. Rep. No. 118, St. Anthony Falls Hydraulic Laboratory, University of Minnesota.
- Tangren R.F., Dodge C.H. and Seifert H.S. 1949. *Compressibility Effects in Two-Phase Flows*. J. Appl. Phys., Vol. 20, pp. 637–645.
- Teslenko V.S. 1979. *Experimental Investigations of Bubble Collapse at Laser-*

Induced Breakdown in Liquids. In "Cavitation and Inhomogeneties in Underwater Acoustics", Proceedings of the First International Conference, ed. W. Lauterborn, Springer-Verlag, New York, pp. 30-34.

van der Meulen, J.H.J. and van Renesse, R.L. 1989. *The Collapse of Bubbles in a Flow Near a Boundary*. 17th Symp. on Naval Hydrodynamics, The Hague, The Netherlands, pp. 379-391.

van Wijngaarden, L. 1964. *On the Collective Collapse of Large Number of Gas Bubbles in Water*. Proc. of 11th Int. Cong. of Appl. Mech., Springer-Verlag, Berlin, pp. 854-861.

Vaughan, P.W. 1968. *Investigation of Acoustic Thresholds by Observation of the First Subharmonic*. Trans. ASME, J. Sound Vib., Vol. 7 (2), pp. 236-246.

Vogel, A., Lauterborn, W. and Timm, R. 1989. *Optical and Acoustic Investigations of Dynamics of the Laser-produced Cavitation Bubbles Near a Solid Boundary*. J. Fluid Mech., Vol. 206, pp. 299-338.